IMPLEMENTATION OF STRONG LIGHT-MATTER INTERACTION FOR FABRICATION AND LIGHT MANAGEMENT OF THIN CRYSTAL SILICON SOLAR CELLS

A THESIS SUBMITTED TO
THE GRADUATE SCHOOL OF NATURAL AND APPLIED SCIENCES
OF
MIDDLE EAST TECHNICAL UNIVERSITY

BY

MONA ZOLFAGHARI BORRA

IN PARTIAL FULFILLMENT OF THE REQUIREMENTS
FOR
THE DEGREE OF DOCTOR OF PHILOSOPHY
IN
MICRO AND NANOTECHNOLOGY

JULY 2021

Approval of the thesis:

IMPLEMENTATION OF STRONG LIGHT-MATTER INTERACTION FOR FABRICATION AND LIGHT MANAGEMENT OF THIN CRYSTAL SILICON SOLAR CELLS

submitted by **MONA ZOLFAGHARI BORRA** in partial fulfillment of the requirements for the degree of **Doctor of Philosophy** i**n Micro and Nanotechnology, Middle East Technical University** by,

Prof. Dr. Halil Kalıpçılar
Dean, Graduate School of **Natural and Applied Sciences**

Prof. Dr. Almıla Güvenç Yazıcıoğlu
Head of the Department, **Micro and Nanotechnology**

Assoc. Prof. Dr. Alpan Bek
Supervisor, **Physics, METU**

Prof. Dr. H. Emrah Ünalan
Co-Supervisor, **Metallurgical and Materials Eng., METU**

Examining Committee Members:

Prof. Dr. Halime Gül Yağlıoğlu
Physics Eng., Ankara Uni.

Assoc. Prof. Dr. Alpan Bek
Physics, METU

Prof. Dr. Burcu Akata
Micro and Nanotechnology, METU

Prof. Dr. Raşit Turan
Physics, METU

Prof. Dr. F. Ömer Ilday
Physics, Bilkent Uni.

Date: 29.07.2021

I hereby declare that all information in this document has been obtained and presented in accordance with academic rules and ethical conduct. I also declare that, as required by these rules and conduct, I have fully cited and referenced all material and results that are not original to this work.

Name, Last name: Mona Zolfaghari Borra

Signature:

ABSTRACT

IMPLEMENTATION OF STRONG LIGHT-MATTER INTERACTION FOR FABRICATION AND LIGHT MANAGEMENT OF THIN CRYSTAL SILICON SOLAR CELLS

Zolfaghari Borra, Mona
Doctor of Philosophy, Micro and Nanotechnology
Supervisor: Assoc. Prof. Dr. Alpan Bek
Co-Supervisor: Prof. Dr. H. Emrah Ünalan

July 2021, 106 pages

The integration of photonic components with electrical elements on the same silicon chip may lead to the development of new technologies. One limitation is the space available on the wafer surface, which is restricted. Currently, conventional fabrication techniques produce devices only on the top thin layer of the wafer surface. As a result, new architectural designs are required. Producing functional components deep inside Si without creating damage to the surfaces is a potential technique for overcoming the space constraint in electronic-photonic integration since the bulk of the wafer can be used with this method. In different transparent materials, such as glasses and polymers, laser-written devices have been shown. High-intensity laser pulses may cause a nonlinear breakdown when focused and can alter the morphology of the material's interaction area. This method is capable of fabricating a broad range of devices, including interconnects, optical waveguides, and quantum photonic devices. However, similar techniques have not been successful in Si. We developed a similar enabling technique inside Si by using nonlinear phenomena to create very controlled modifications deep inside Si.

Recently-demonstrated direct laser modification of high-quality three-dimensional (3D) subsurface inside of crystalline silicon (c-Si) wafers opens the doors to a wide range of novel applications in multidisciplinary research areas. A specially developed selective wet chemical etching step is usually required to follow subsurface processing of c-Si by laser in order to reveal the desired 3D structures. Proper development of such a selective etchant that leaves remaining unprocessed Si surfaces with smooth features is critical for subsequent applications at micro- and nanoscales. Achieving practically useful etch rate, etch selectivity, and final surface morphology of subsurface laser processed Si is essential and yet highly complicated due to intricate interdependence of these aspects through the etchant composition. Moreover, the well-accepted definitions of etch rate and selectivity in semiconductor micro-processing are univocally valid for surface etch in 2D in literature. As laser processing of crystalline semiconductors is an emerging technique, there appears to be a need for redefinition of both etch rate and selectivity since the etch takes place subsurface in 3D where etch thickness/time is not an applicable measure. Here, we report on development of a novel chromium-free (Cr-free) chemical etching recipe based on copper nitrate which yields substantially smooth surfaces at a high etch rate and selectivity of the both surface and subsurface laser processed Si without inducing significant etching of unmodified Si. The results show that etch rate and surface morphology are interrelated and highly affected by the composition of the adopted etching solution. After an extensive compositional study performed at room temperature, we achieved to develop such an etchant with a composition of $HF:HNO_3:CH_3COOH:H_2O$ – 56:65:72:207 (vol%), and 1 g of $Cu(NO_3)_2.3H_2O$ in 100 ml solution. This champion etchant exhibits more than 1600 selectivity for laser modified Si with respect to unmodified Si. Etch pit size distribution of surface defect analysis shows pit sizes to reside in the range of 1 – 10 µm indicating relatively smooth and low defective surface. In order to demonstrate the application potential of the etchant, c-Si solar cells based on thin absorber slices produced with a minimum loss of Si material. Additionally, we etched the laser processed parts of a c-Si to reveal high aspect ratio micro holes all the way through a wafer of 250 µm thickness, which has the potential to be utilized in the fabrication and development of microfluidic devices and photonic devices on Si, and also fabricated micro pillars with various sizes/depth to reach the minimum reflection which is crucial for solar cells. This work is the first to propose and use new definitions of etch rate and selectivity in etching of 3D structures.

Keywords: laser processing, subsurface modifications, selectivity, silicon, etch rate

ÖZ

İNCE KRİSTAL SİLİSYUM GÜNEŞ HÜCRELERİNDE ÜRETİM VE IŞIK YÖNETİMİ İÇİN YOĞUN IŞIK-MADDE ETKİLEŞİMİ UYGULAMASI

Zolfaghari Borra, Mona
Doktora, Mikro ve Nanoteknoloji
Tez Yöneticisi: Doç. Dr. Alpan Bek
Ortak Tez Yöneticisi: Prof. Dr. H. Emrah Ünalan

Temmuz 2021, 106 sayfa

Fotonik bileşenlerin elektriksel elemanlarla aynı silisyum çip üzerinde entegrasyonu, yeni teknolojilerin geliştirilmesine yol açabilir. Bir sınırlama, kısıtlı olan dilim yüzeyindeki mevcut alandır. Halihazırda, geleneksel üretim teknikleri, yalnızca dilimin en ince tabakası üzerinde cihazlar üretmektedir. Sonuç olarak, yeni mimari tasarımlara ihtiyaç duyulmaktadır. Yüzeylere zarar vermeden Si'nin derinliklerinde fonksiyonel bileşenler üretmek, elektronik fotonik entegrasyondaki alan kısıtlamasının üstesinden gelmek için potansiyel bir tekniktir, çünkü Si dilimin büyük kısmı bu yöntemle kullanılabilir. Camlar ve polimerler gibi farklı şeffaf malzemelerde lazerle yazılmış cihazlar gösterilmiştir. Yüksek yoğunluklu lazer darbeleri, odaklanıldığında doğrusal olmayan bir bozulmaya neden olabilir ve malzemenin etkileşim alanın morfolojisini değiştirebilir. Bu yöntem, optic ara bağlantılar, optik dalga kılavuzları ve kuantum fotonik aygıtlar dahil olmak üzere çok çeşitli cihazları üretebilir. Ancak benzer teknikler Si'de başarılı olamamıştır. Si'nin derinliklerinde çok kontrollü değişiklikler yaratmak için doğrusal olmayan etkileri kullanarak Si içinde benzer bir etkinleştirme tekniği geliştirdik. Son zamanlarda, kristal silisyum (c-Si) dilimlerin içindeki yüksek kaliteli üç boyutlu (3B) yüzeyaltının doğrudan lazer modifikasyonu, çok disiplinli araştırma alanlarında çeşitli yeni uygulamaların kapılarını açar. İstenen 3B yapıları ortaya çıkarmak için c-Si'nin lazerle yüzeyaltı işlemesini takip eden genellikle özel olarak geliştirilmiş bir seçici ıslak kimyasal aşındırma adımı gerekir. Geri kalan işlenmemiş Si yüzeylerini pürüzsüz özelliklere sahip bırakan böyle seçici bir aşındırıcının uygun şekilde geliştirilmesi, mikro ve nano ölçekli sonraki uygulamalar için kritik öneme sahiptir. Yüzey altı lazerle işlenmiş Si'nin pratik olarak faydalı aşındırma hızı, aşındırma seçiciliği ve nihai yüzey morfolojisinin elde edilmesi esastır ve yine de aşındırıcı kompozisyon yoluyla bu yönlerin karmaşık şekilde birbirlerine bağımlılığı nedeniyle oldukça karmaşıktır. Ayrıca, yarı iletken mikro işlemede iyi kabul edilen aşındırma hızı ve seçicilik tanımları, literatürde yalnız 2B'de yüzey aşındırma için geçerlidir. Kristalli yarı iletkenlerin lazerle işlenmesi yeni gelişen bir teknik olduğundan, aşındırma kalınlığı/zamanının uygulanabilir bir ölçü olmadığı yerlerde aşındırma, yüzeyin altında 3B gerçekleştiğinden hem aşındırma hızının hem de seçiciliğin yeniden tanımlanmasına ihtiyaç vardır. Burada, yüksek aşındırma hızında büyük ölçüde pürüzsüz yüzeyler ile hem yüzey hem de yüzey altı lazerle işlenmiş Si'nin seçici olarak aşındıran bakır nitrat bazlı yeni bir krom (Cr) içermeyen kimyasal aşındırma tarifinin geliştirilmesini rapor ediyoruz. Sonuçlar, aşındırma hızının ve yüzey morfolojisinin birbiriyle ilişkili olduğunu ve kabul edilen aşındırma çözeltisinin bileşiminden büyük ölçüde etkilendiğini göstermektedir. Oda sıcaklığında yapılan kapsamlı bir kompozisyon çalışmasından sonra, 100 ml solüsyonda $HF:HNO_3:CH3COOH:H_2O$ – 56:65:72:207 (% hacim) ve 1 g $Cu(NO_3)_2.3H_2O$ bileşimi ile aşındırıcı geliştirmeyi başardık. Bu şampiyon aşındırıcı, değiştirilmemiş Si'ye göre lazerle modifiye edilmiş Si için 1600'den fazla seçicilik sergiler. Yüzey kusur analizinin aşındırma çukuru boyutu dağılımı 1 – 10 µm aralığında olup, görece pürüzsüz ve düşük kusurlu yüzey elde edildiğini gösterir. Aşındırıcının uygulama potansiyelini göstermek için, ince soğurucu (absorber) dilimler üzerinde c-Si güneş pilleri, minimum Si malzemesi kaybıyla üretildi.

Ek olarak, bir c-Si'nin lazerle işlenmiş parçalarını, mikroakışkan kanalları ve fotonik cihazların imalatında ve geliştirilmesinde kullanılma potansiyeline sahip 250 µm kalınlığındaki bir dilim boyunca yüksek en-boy oranlı mikro delikleri ortaya çıkarmak için aşındırdık. Ayrıca lazerle işlenmiş olan bu parçaları güneş hücrelerinde çok önemli olan minimum yansımaya ulaştıracak çeşitli boyut/derinliğe sahip mikro sütunları ortaya çıkarmak için aşındırdık. Bu çalışma, 3B yapıların aşındırılmasında yeni aşındırma hızı ve seçicilik tanımları öneren ve kullanan ilk çalışmadır.

Anahtar Kelimeler: lazer işleme, yüzey altı modifikasyonları, seçicilik, silisyum, aşındırma oranı

To my family,

Who has faith in my potential

ACKNOWLEDGMENTS

First of all, I would like to express my sincere gratitude to my advisor, Assoc. Prof. Dr. Alpan Bek for the continuous support of my thesis study and research, for his patience, motivation, and immense knowledge. It has been a long and effective journey during my M.Sc. and Ph.D. studies with him.

My deepest thanks belong to Assist. Dr. Ihor Pavlov for his continuous guidance, valuable knowledge, creativeness, positive attitude, and time throughout my thesis study.

I am thankful to Prof. Dr. Raşit TURAN for giving us the opportunity of working in GÜNAM lab and for his ultimate support.

I would like to thank Prof. Dr. H. Emrah Ünalan for having given me the opportunity to have him as my co-advisor for this research.

I would like to thank Prof. Dr. F. Ömer Ilday and Prof. Dr. Burcu Akata for assisting me with their innovative ideas during my thesis.

Next, I would like to special thank Dr. Hisham Nasser for his support, continuous encouragement, friendship, and valuable guidance throughout my Ph.D. study.

I would like to thank Behrad Radfar for his friendship, illuminating discussions and contribution throughout my thesis work and Hande Çiftpınar for her friendship and her contribution to solar cell fabrication.

I would like to thank Assoc. Prof. Dr. Tahir Çolakoğlu and Assist. Dr. Onur Tokel for giving creative ideas for the thesis.

I would like to thank Dr. Ahmet Turnalı for his efforts in the laser processing of silicon.

Massive thanks to Dr. Mehmet Koç for drawing professional 3D figures for the thesis and discussion was amazing indeed.

I would like to thank Mustafa Ünal and Ozden Başar for the time they invested in formatting my thesis, which may be a burden for me without their help.

I would like to thank Gence Bektaş for his friendship and his assistance in translating my abstract to Turkish.

I wish to express my deepest gratitude to Nasim Seyedpour Esmaeilzad, Parisa Sharif, Salar H. Sedani, and Kerim Yusufi for their support, kindness, and pleasant moments that I spent with them.

I would like to express my warm thanks to Gamze Kökbudak and Ozan Akdemir, who are always patient, kind, and helpful to me.

I would like to next thank to all GÜNAM family; Ergi Donercark, Samet Özdemir, Ateş aliefendioğlu, Mehmet can Karaman, Milad Ghasemi, Buket Gökbakan, all technical and administrative staff and Nano-Optics group for their friendship and help.

I would like to thank my friends Fırat Es, Emel Semiz, and Efe Orhan for their friendship and discussions during my thesis.

I would like to thank my beloved parents and siblings who supported and believed in me and were always there for me in the most stressful moments.

This work is partially funded by the Scientific and Technological Research Council of Turkey under grants number TUBİTAK: 113M930-931-932 and 118M003.

TABLE OF CONTENTS

ABSTRACT v

ÖZ viii

ACKNOWLEDGMENTS xii

TABLE OF CONTENTS xiv

LIST OF TABLES xvii

LIST OF FIGURES xviii

LIST OF ABBREVIATIONS xxiii

CHAPTERS

1 INTRODUCTION 1

1.1 Background and research motivation 1

1.2 Research aims and objectives 4

1.3 Thesis outline 5

2 THEORITICAL BACKGROUND 7

2.1 Mechanism of subsurface laser modifications inside silicon 7

2.1.1 Mechanisms of carrier generation and recombination in silicon 7

2.1.2 Nonlinear mechanisms of heat generation and temperature profile in silicon 11

2.1.3 Light propagation in silicon 13

2.1.4 Light propagation under nonlinear feedback conditions in silicon 15

2.2 Explanation of the toy model 19

2.3 Silicon etching 26

2.3.1 Metal assisted chemical etching 27

2.3.2 Mechanism of metal assisted chemical etching on laser modified region 30

3 SELECTIVE CHEMICAL ETCHING 33

3.1 Fabrication steps 36

3.1.1 Laser-Induced silicon modifications 37

3.1.2 Comparison of different Chemical etchant composition 38

3.1.3 Silicon sample structures 41

3.2 Etch rate and selectivity redefined 41

Correction factors calculation & etch pit radius distribution analysis 44

3.3 Results and discussions 51

3.3.1 Comparison of MEMC and the Developed Champion Etchant 52

3.3.2 Effects of solution components on etchant chemistry 54

4 APPLICATIONS OF ENHANCED SELECTIVE CHEMICAL ETCHING .65

4.1 Thin crystalline silicon slicing 65

4.1.1 Overview of LASIS technique: 65

4.1.2 Si slices production based on selective etching of laser-modified region.66

4.1.3 Solar cell fabricated based on Si slice processed by LASIS method 68

4.2 High aspect ratio micro pillar arrays on Si 70

4.3 High aspect ratio micro-hole drilling on Si 74

5 CONCLUSION 79

REFERENCES 83

APPENDICES

A. Dicing of CALP Samples 97

B. Mass weights 98

C. Infrared images of laser modified region 100

D. Derivative of laser modified of etched mass 102

CURRICULUM VITAE 105

LIST OF TABLES

TABLES

Table 3.1 Chemical composition of the different etching solutions. The KOH-assisted etching was done at 80°C while other treatments were performed at room temperature. The duration of etching was varied based on the etch speed of the corresponding etching solution. 39

Table 3.2 Chemical composition of solutions by variation of $Cu(NO_3)_2$ concentration, HF concentration, and HNO_3 concentration. The amount of H_2O is adjusted to obtain 100 ml of solution (which corresponds to 100%). 44

Table 3.3 Effect of MEMC etching solution on the <111> and <100> plane and p-type and n-type wafers with duration of 12min. 53

Table 3.4 Effect of *the Champion Etchant* etching solution on the <111> and <100> plane and p-type and n-type wafers with duration of 18min. 53

Table 4.1 Various hole diameter values relative to laser pulse energy................... 77

LIST OF FIGURES

FIGURES

Figure 2.1 Experimental values show carrier density evolution. The black graph demonstrates laser intensity and the red graph demonstrate carrier density as a function of time [59]. 9

Figure 2.2. For individually temporal slice, the intensity distribution ($Ienv$) is calculated by considering the free carrier distribution, temperature, and refractive index from the previous iteration [59]. 16

Figure 2.3 Simulations of single laser pulse propagation in Si. Intensity distribution for the undressed beam case (a). Intensity distribution of the dressed beam case (b). Intensity evolution on a location where modification occurs. The blue graph shows the dressed beam case, and the red graph for the undressed case. The double peak is caused by the thermal lensing delay, which becomes effective in a few ns after FCI. This implies that the two effects are in competition. (c). Thermal evolution in the area of modification. Temperatures approach the melting temperature of Si in the dressed beam case (blue graph), but are restricted to 800 K in the undressed beam case (red curve) (d) [59]. 18

Figure 2.4 The pulse propagation for the cases with and without counter propagating beam (a), Image of IR transmission microscope that shows the subsurface modification only in double-side polished region (b) [59]. 24

Figure 2.5 Experimental data (red circles) and toy model expectation (blue graph) [59]. 25

Figure 2.6 Controlled structures formed by various number of laser pulses. Scanning Electron Microscope (SEM) images shows high aspect ratio of subsurface structures are created with (orange) for 20 and (blue) for 200 pulses (a). The scale bar is $40\mu m$. the comparison of structure length measurements from both SEM images with *in-situ* measurements and IR transmission microscopy (b) [59]. 25

Figure 3.1 Schematic of the experimental set-up (a), Photographs of the set-up (b,c). 36

Figure 3.2 (a, c) – Demonstration of laser beam scanning direction inside of the c-Si for CALP sample (a), and for SALP sample (c); (b, d) – Schematic representation of the laser processed zones for CALP sample (b), and for SALP sample (d) (see more explanations in text). 38

Figure 3.3 SEM images of different etching treatments on the subsurface laser-modified regions. Subfigures (a) to (e) corresponds to solution 1 to 5 in the Table 3.1 respectively. 40

Figure 3.4 Illustration of SALP sample in the chemical bath (a). Illustration of and CALP sample in the chemical bath. In both cases, an unprocessed Si was added (b). 42

Figure 3.5 Cross-sectional SEM image after 60 min etching showing the opening and etch pits resulted from the etching process for the champion etchant. 45

Figure 3.6 Area of the opening after etching treatment at the specific magnification (Set Opt: 500x). 46

Figure 3.7 The etch rates of laser modified region (red) and unprocessed sample over time, including the linear trend line of each etch rate for the champion etchant. 48

Figure 3.8 The selected area for the champion etchant from cross-sectional SEM image and the result etch pit size distribution analysis. 50

Figure 3.9 Etched masses of laser modified region and unprocessed sample corrected by exposed area for the champion etchant. 50

Figure 3.10 SEM images of laser modified openings after etching in the developed solution with different $Cu(NO_3)_2$ concentration: 0.75g to 2g in 100ml of etching solution. 55

Figure 3.11 SEM images of variation of HF concentration from 31ml to 46ml in 100ml of etching solution. 56

Figure 3.12 SEM images of variation of HNO_3 concentration from 15ml to 35ml in 100ml of etching solution. 57

Figure 3.13 Image of infrared camera of the etched laser modified region. 57

Figure 3.14 Etch rate of laser modified region over time by changing the $Cu(NO_3)_2$ concentrations from 0.75 to 2 g in 100 ml of solution for CALP (a); The selectivity of laser modified region comparing to unprocessed sample by fitting the etch rates over time for CALP (b); The area corrected etched mass of laser modified region for SALP (solid line) and CALP (dashed line) for different concentrations over 60 minutes (c); Normalized etched mass of laser modified region for SALP (d); The ratio of area normalized etched mass of laser modified region over the unprocessed region for SALP (e); Etch pit radius distribution obtained from SEM images by analyzing the surface morphology (f)..58

Figure 3.15 Etch rate of laser modified region over time by changing the HF concentrations from 7 ml to 18 ml in 100 ml of solution for CALP (a); The selectivity of laser modified region comparing to unprocessed sample by fitting the etch rates over time for CALP (b); The area corrected etched mass of laser modified region for SALP (solid line) and CALP (dashed line) for different concentrations over 60 minutes (c); Normalized etched mass of laser modified region for SALP (d); The ratio of area normalized etched mass of laser modified region over the unprocessed region for SALP (e); Etch pit radius distribution obtained from SEM images by analyzing the surface morphology (f)..60

Figure 3.16 Etch rate of laser modified region over time by changing the HNO_3 concentrations from 9.75 to 22.75 ml in 100 ml of solution for CALP (a); The selectivity of laser modified region comparing to unprocessed sample by fitting the etch rates over time for CALP (b); The area corrected etched mass of laser modified region for SALP (solid line) and CALP (dashed line) for different concentrations over 60 minutes (c); Normalized etched mass of laser modified region for SALP (d); The ratio of area normalized etched mass of laser modified region over the unprocessed region for SALP (e); Etch pit radius distribution obtained from SEM images by analyzing the surface morphology (f). 62

Figure 4.1 Steps of LASIS silicon micro slicing processes: Laser processing of subsurface (a), Modified part after laser processing (b), Selective chemical etching (c), Slicing into plates (d). 66

Figure 4.2 SEM images of 20 minutes etching (a), After 60 min etching (b), produced c- Si slice with 1mm × 0.5 mm area (c), After 20 min etching (d), After 3 hours etching (e), produced c-Si slice with 10 mm × 5 mm area (f). 67
Figure 4.3 SEM images of multi-layers after 30 min etching, the thicknesses of slicing are: ~80 µm (a), ~60 µm (b), ~ 45 µm (c), ~35 µm (d). 68
Figure 4.4 Schematic of c-Si solar cell structure (a), J-V curve of the first solar cell fabricated from LASIS Thin Sliced c-Si based on Al-BSF design (b). 69
Figure 4.5 Steps of micro pillar processes: Modified part after laser processing pattern of pillar (a), Selective chemical etching (b), Pillar arrays (c). 71
Figure 4.6 SEM images of micro-pillar arrays from top surface (a, c), 40° tilted (b), 60° tilted (d) with pillar area: 9 µm × 9 µm, Pillar depth of 118 µm and pulse energy 3 µj. 71
Figure 4.7 SEM images of micro-pillar arrays from top surface (a, c), 60° tilted (b), 40° tilted (d) with pillar area: 31 µm × 31 µm, Pillar depth of 158 µm and pulse energy 3 µj. 72
Figure 4.8 SEM images of micro-pillar arrays from top surface (a, c), 40° tilted (b,d), with pillar area: 57 µm × 57 µm, and pulse energy 3 µj. 72
Figure 4.9 Measured total reflection of the fabricated micro pillars with various areas and individual depth. 73
Figure 4.10 Steps of micro hole processes: Modified part after single circular motion of the laser processing (a), Selective chemical etching (b), Periodic hole drilling (c). 75
Figure 4.11 Top view SEM images of laser-processed drilled holes in c-Si wafer at different pulse energy: 2 µJ (a), 2.5 µJ (b), 3 µJ (c), 3.5 µJ (d), 4 µJ (e),4.5 µJ (f) and 5 µJ (g), after 90 minutes etching. 76
Figure 4.12 Average various holes diameter size as a function of the pulse energy. 77
Figure 4.13 Top-view SEM images of laser-processed drilled holes at 5 µJ pulse energy and chemically treated c-Si with selective etchant recipes: hole laser

processing before etching (a), enhanced composition after 90 minutes etching (b), optical microscope image of the produced drilled holes (c). 78

LIST OF ABBREVIATIONS

ABBREVIATIONS

3D	Three dimensions
Crystalline Silicon	c-Si
2D	Two dimensions
TPA	Two photon absorption
VB	Valence band
CB	Conduction band
FCA	Free carrier absorption
FCI	Free carrier index
α_{FCA}	free charge carrier absorption coefficient
n_{FCI}	density of free charge carrier index
FDTD	Finite difference time domain
FEM	Finite element method
NPE	Nonlinear paraxial equation
SiN_x	Silicon nitride
SEM	Scanning Electron Microscope
DRIE	deep reactive ion etching
MACE	metal-assisted wet chemical Si etching
b-Si	Black silicon
PSi	Porous silicon
LASIS	laser-induced silicon thin film slicing

CHAPTER 1

INTRODUCTION

The purpose of this study is to use nanosecond pulse laser to produce subsurface modifications and creation of embedded periodic structures in crystalline silicon. In this thesis work, a highly selective specialized etchant for removal of laser modified regions from Si wafers was developed. As laser direct processing of Si has arrived at its maturity, the need for such a selective etch agent has emerged. Utilization of direct laser processing and subsequent selective etching of Si, paves the way for fabricating a vast range of devices out of 3D sculpted microstructures embedded in silicon.

1.1 Background and research motivation

A new emerging silicon (Si) micro-processing technology is a crucial step that requires integrating photonic components with conventional integrated circuits [1,2]. To achieve this, optical components that can produce, manipulate, and detect light on the same chip as electronic circuits must be created [3]. However, until recently, there was no technique for inducing structural modifications or the formation of functional components deep inside Si. Integration of photonics and data-transfer components inside Si wafers is highly desirable since this may result in new generations of electronic devices. The silicon-on-insulator (SOI) technology is now the preferred method for manufacturing optical components for Si-photonics applications [3]. On this technology, active and passive optical components are fabricated on the Si substrate using conventional methods such as e-beam lithography and chemical etching. These methods utilize just the uppermost layer of the SOI device, thus which wastes much of the wafer bulk to place the functional components.

Various structures with varying functions have been demonstrated using direct-laser writing techniques on Si. Micropillar arrays [4] and surface ripples [5], were produced on Si substrates using laser diffraction. Furthermore, laser direct writing on Si surface can form the so-called black silicon (b-Si) which enhances light absorption for solar cell applications. These advancements are very advantageous in solar cell and thermal imaging applications [6,7]. Additionally, laser-writing is used to modify the surface characteristics of Si. Silicon can be achieved to superwicking by creating the surface pattern with a pulsed laser [8]. All these studies modified the optical and physical characteristics of Si, demonstrating the possibilities enabled by laser-Si interaction. These photo-induced effects, on the other hand, occur at the surface.

Laser micro-fabrication of transparent materials is a potential method for manufacturing three-dimensional (3D) embedded devices [9]. Alternative of these 3D methods have been used widely on glasses and polymers during the last decade [10]. Depending on the time scale, intensity, and energy of the laser pulse, photons can either nonlinearly transmit their energy to the medium, forming a seed electron population such as multi-photon ionization, or to phonons, causing a nonlinear breakdown [11,12]. Utilization of these processes enables the fabrication of a variety of optical devices, such as waveguides [13], quantum photonic circuits [14], resonators [15], and optical interconnects [16], buried within the bulk of materials like as glasses and lithium niobate crystals, with essential applications in integrated optics [17,18]. In a similar but distinct fashion, such an enabling technology is recently displayed for Si [19], in which nonlinear optical effects are used to produce controlled structures deep inside Si [20,21]. Then, these structures are engineered to form functional in-chip components without damaging the wafer surface. Prior efforts to modify the bulk of the Si, mainly ultrafast lasers, are utilized. Nejadmalayeri et al, pioneered in this field by developing optical waveguides [22]. Nevertheless, waveguides may be written in a very confined area at the wafer's surface rather than throughout the wafer. Attempts to create completely buried modifications failed without surface damage due to absorption or plasma shielding [23,24]. To reach the modification threshold, the pulse energies were raised to 90 µJ, however, this did not result in subsurface modifications. Numerous studies examined the nonlinear dynamics of these mechanisms in depth [25,26]. As a result, the range of the modifications were restricted to interfaces [22] or areas adjacent to the back surface [27]. The feasibility of producing subsurface modifications within Si was shown utilizing nanosecond pulses and initially described in Ref [20,28]. The formation of subsurface structures using a nanosecond or femtosecond pulsed laser beam [29–33] is a new approach for high-quality micro and nanofabrication applications. This method creates modification at localized regions with minor damage on the Si surface [20,34]. For revealing the 3D laser sculpted structures out of Si bulk, laser modified regions of the c-Si subsurface are removed by selective chemical etching. Accordingly, etching is an essential process step in micro and nanofabrication of c-Si based devices. Among different etching techniques, solution based chemical etching offers a low-cost and facile alternative compared to conventional plasma enhanced gas phase etching counterparts, while yielding a high surface and bulk material quality due to absence of plasma damage. Achieving a Si surface as defect-free as possible at the microscale is crucial to ensure high performance of Si devices, such as micro-electromechanical systems (MEMS) [35–38], micro-optics [39,40], photonic devices, integrated circuits, and photovoltaic solar cells [41–47].

The 3D Si structures can be utilized in a wide range of applications, including quantum photonics [48], lab-on-chip [49–52], optical communications [53], and microfluidics [54–56]. So far, neither the surface nor subsurface laser processing of Si has yet been investigated deep enough to unearth the full potential of 3D laser processing in micro-fabrication of Si devices. In this respect, a well-established route to selectively remove the laser modified regions from the Si wafer; without damaging unprocessed regions, simply does not exist. A natural outcome of surface laser processing is the intentional damage that it induces to the certain regions of the surface, therefore it is imperative that a specially tailored selective etchant needs to be developed for effective removal of only laser damaged regions. In Si technology, researchers have invested substantial efforts to control the defect densities associated with re-growth and Si wafer processing [57]. Selective chemical etching is a simple route to reveal the number of defects in the c-Si. Chemical treatments typically comprise a redox reaction to etch the defects selectively. In a more general view, it is of great essence that such a special etchant is developed to selectively remove laser modified Si out of c-Si wafer in order to sculpt functional 3D structures.

In this thesis, the creation of laser-induced rod-like structures with tunable lengths deep within Si will be reported. It will be shown, numerically and experimentally, that feedback mechanism is in effect when these high aspect ratio structures are formed. Due to the morphological difference produced by the laser exposure, selective etching is crucial, which has been used for the sculpting of Si. The development of a novel chemical etching recipe based on copper nitrate to produce substantially smooth surfaces at a high etch rate and selectivity of both surface and subsurface laser processed Si without inducing significant etching of unmodified Si is reported. An emerging application demonstrated by using this technique, is the laser assisted Si slicing (LASIS) [34] in which thin c-Si slices can be processed into thin/ultra-thin Si solar cells produced with a minimum loss of Si material. Low material loss in slicing is an important requirement in reduction of the solar cell cost. In addition, 3D structures such as high aspect ratio holes drilling and micropillars utilizing this technique will be shown.

1.2 Research aims and objectives

The purpose of this thesis is to use nanosecond pulse laser to produce subsurface modifications and creation of the embedded periodic structures. However, to reveal high-quality subsurface structures different chemical etching solutions should be investigated.

Besides, etch rate, etch selectivity, and final surface morphology of subsurface laser processed Si is final objective but also very complicated because of the interdependence of these factors through the etchant composition. The following procedures are used to accomplish the aforementioned study goals:

1. Study of the developing selective wet chemical etching to follow subsurface processing of c-Si by nanosecond fiber laser in order to reveal the desired 3D structures.

2. Redefinition of both chemical solutions etch rate and corresponding selectivity for subsurface processing in 3D structures where etch thickness/time is not an applicable measure. In addition, final morphology of surface and subsurface laser processed Si is analyzed.

3. Demonstration of the first solar cell fabricated from thin c-Si slice produced by laser-induced thin film slicing (LASIS) technique.

4. Fabrication of various 3D architectures of micro-deep structures in Si using laser induced subsurface technique.

1.3 Thesis outline

The thesis is organized into five chapters. Chapter 1 gives a brief research backgrounds including the introduction of laser-induced subsurface modifications by utilizing nanosecond pulses and developed etching for revealing the 3D structures by high selectivity of the laser-modified surface and subsurface Si at high etch rates.

Chapter 2 includes two sections. In the first section, the physical mechanism behind the effective creation of modifications is discussed. Specially, the development of carrier and temperature profiles caused by nanosecond laser pulses interacting with silicon are described. Additionally, a model that explains why and how counter-propagating beams form in-chip structures is proposed. In the second section, the chemical background and mechanism of metal assisted etching on both surface and subsurface modifications is discussed.

Chapter 3 focuses on developing a highly specialized chemical solution to selectively etch laser-modified surface and subsurface Si regions at high etch rates. The etch recipe is optimized to meet the requirement of reasonable etch rate while resulting in smooth Si facets. In addition, the quality of surfaces, sensitivity, reliability, and selectivity which are the key factors in the development of the developed etch solution are extensively investigated. The methods of the experiments are described in this chapter.

Chapter 4 comprises the end products of selective etching of laser-modified regions and microstructures. 3D applications such as Si slicing and corresponding solar cell prototype, high aspect ratio of micropillars and hole drilling by utilizing this technique are shown.

Chapter 5 concludes the study of laser-induced subsurface modifications by nanosecond laser pulses and development of a selective wet-chemical etchant for surface and subsurface for laser modified Si region. This chapter discusses the major results and potential future topics.

CHAPTER 2

THEORITICAL BACKGROUND

2.1 Mechanism of subsurface laser modifications inside silicon

In order to explain the formation of controlled structure in c-Si, specifically to fabricate high aspect ratio, rod-like and three dimensional (3D) modifications inside Si, we employ nonlinear interactions between silicon and the infrared laser pulses. The approach we use here is an extension of the nonlinear laser lithography (NLL), which exploits nonlinear feedback mechanisms in two dimension (2D) surface structuring [58]. This method enables to laser induced formation of modified region in the balk of Si with self-organized structures directly without damage on the c-Si surfaces. In this section, we describe the theoretical mechanism and give physical background information which are carrier generation, thermal nonlinearity, pulse propagation and nonlinear feedback mechanisms about the structure formation. The described mechanisms in this chapter have been developed in collaboration with Ultrafast Optics and Lasers Laboratory (UFOLAB) group of Bilkent University [59].

2.1.1 Mechanisms of carrier generation and recombination in silicon

The carrier generation is due to laser pulse propagation and thermal profile inside c-Si. Accordingly, to understand the formation of modification, first we examine free electron generation to get carrier profile and their recombination mechanism to get temperature profile as a result of carrier recombination in c-Si. We analyze later how the combination of these profiles contributes to the nonlinear effects in pulse propagation such as free carrier induced diffraction and thermal focusing, for the formation of subsurface modification mechanism in c-Si.

For the wavelength higher than band gap of Si (1.12 eV) absorption coefficient decreases to zero and Si behaves as a transparent material. Whereas, for high optical intensities, two photon absorption (TPA) can excite an electron from the valence band (VB) to the conduction band (CB) and leads to the generation of free carriers. Strong nonlinear absorption of TPA and free carrier effects in Si material result in an intensity profile behave deviation from the Beer-Lambert Law. Diffusion and recombination due to the carrier generation in Si leads to change the quasi-steady state carrier profile. Consequently, we will investigate all these mechanisms in Si material.

In our experiment, for the TPA process, two absorbed photons simultaneously cause free carrier (electron-hole pair) generation. Considering the impact of the TPA, free-carrier rate is expressed as $\xi = \beta_2 \, I(t)^2/2hf$ where β_2 is the TPA coefficient, $I(t)$ is the instantaneous intensity, h is the Planck constant and f is the photon frequency. The TPA process, the same two absorbed photons densities are denoted by N. Although high TPA leads to generate excess carrier optically, for Si which is a material with an indirect bandgap [60] , excess carriers recombine dominantly due to a phonon-assisted mechanism named the Auger recombination process. The carrier recombination densities is $\mathrm{N} > 10^{18} - 10^{19} cm^{-3}$. In this regime, other recombination processes like radiative and Shockley-Read-Hall (SRH) processes can be omitted [61]. For a single pulse, in the presence of final free carrier density without recombination is defined by Eq 2.1.

$$\mathrm{N}_{avg} = \int_{-\infty}^{\infty} \frac{\beta I(t)^2}{2hf} dt = \int_{-\infty}^{\infty} \frac{\beta \mathrm{I}_0^2 exp \ -2t^2/\tau_{pulse}^2}{2hf} dt = \frac{\sqrt{\pi}\beta \mathrm{I}_0^2}{2\sqrt{\pi}hf} \tau_{pulse} \qquad \text{Eq 2.1}$$

Where I_0 is the peak intensity intensity, β is the TPA coefficient and τ_{pulse} is the pulse duration. For the experimental parameters (τ_{pulse}= 3 ns, P_{avg}= 2 W, ω_0= 3 µm and I_0= 250 $W/\text{µ}m^2$), we achieved carrier density in the amount of $10^{21} cm^{-3}$. Before achieving this amount, Auger recombination prevent the free carrier density to get upper limit. With the prior consideration, the free carrier density is changed as:

$$\frac{d\mathrm{N}}{dt} = \frac{\beta \mathrm{I}^2}{2hf}\left(1 - \frac{\mathrm{N}}{\mathrm{N}_{at}}\right) - \Upsilon_3 \mathrm{N}^3 \qquad \text{Eq 2.2}$$

Where hf is the photon energy, I is the laser density, Υ_3 is the Auger recombination constant [62] and N_{at} is the atomic density in the crystal. The second term of the equation define the nonlinear effect of the TPA lead to generate free carrier and the first term of the equation shows Auger recombination due to excess carrier recombines through the temperature increment of the phonon effect. Carrier recombination time is $\tau_{rec} = 1/\gamma^3\, N^2$ which is comparable to the pulse duration for $N \approx 10^{19} cm^{-3}$. Therefore, average carrier density (since the recombination time is a function of carrier density) and pulse length (several nanosecond pulse generation) defined by time scale of the accumulative carrier density evolution. We verify carrier dynamics in the assets of recombination by solving Eq 2.2 numerically. The optical carrier density is in the range of $10^{19} - 10^{20} cm^{-3}$as we consider previously. Figure 2.1 shows the trend of the carrier density profile and pulse profile corresponding to the time. As it can be seen, both density and pulse profiles closely follow together.

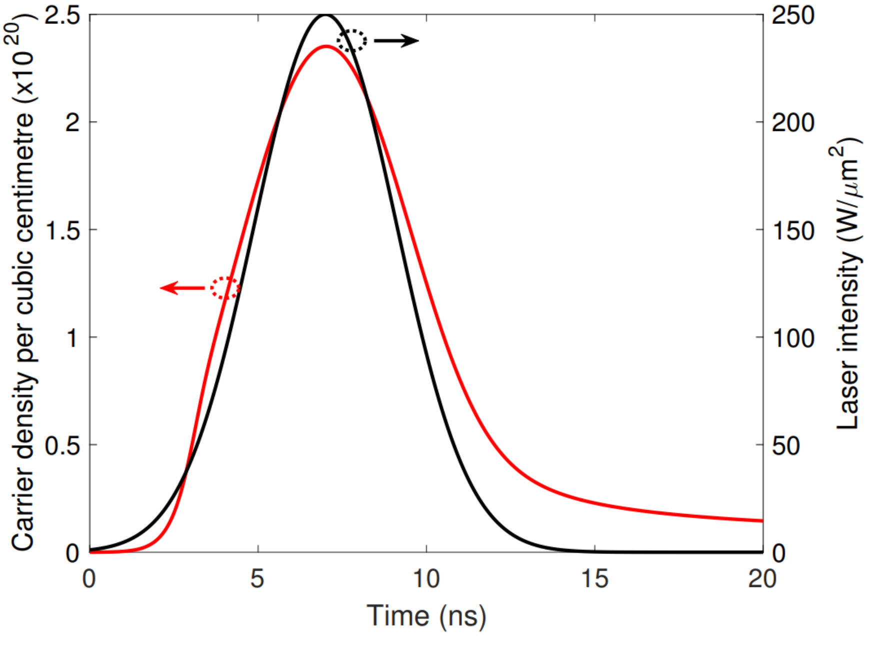

Figure 2.1 Experimental values show carrier density evolution. The black graph demonstrates laser intensity and the red graph demonstrate carrier density as a function of time [59].

Now, we regard as the effect of carrier diffusion on the carrier density. Excited carriers are important to figure out the response of Si to laser pulses. Diffusion of carriers should be accounted for the excited carriers before recombining or before pulse ends. So, carrier diffusion can be ignored if the diffusion length in the time scale of carrier (or recombination time or pulse duration) is less than the diameter of beam at the focal plane. Diffusion length equation is $L_{diff} = \sqrt{6D\tau_{pulse}} \ll S$, where D is the diffusion constant, τ_{pulse} is pulse duration and S is the smallest beam diameter in Si. For Si the carrier diffusion constant define as, $D_{carrier} = 2K_B T_e \mu_e \mu_h / (e(\mu_e + \mu_h))$, where K_B is the Boltzman constant, T_e is electron temperature, and μ_e *and* μ_h are mobilities of the electron and hole respectively. The diffusion length is 1.8 µm at the temperature of 300K which is smaller than beam width at focus of 3 µm. Electron and hole mobilities of Si increases as the temperature decrease [62], additionally, reducing the diffusion length. Recombination time reduced by high energy excessing carrier density; a large number of carriers will recombine before they diffuse out of the beam. So, carrier diffusion can be removed in Eq 2.2.

The same simplification viable for the carrier generation due to the contribution of avalanche ionization. In avalanche ionization, free carriers lose some of their energy to the electrons in VB during electron-hole generation mechanism. This effect can be added by modifying Eq 2.2 as:

$$\frac{d\mathrm{N}}{dt} = (\frac{\beta \mathrm{I}^2}{2hf} + \delta N)(1 - \frac{\mathrm{N}}{\mathrm{N}_{at}}) - \Upsilon_3 \mathrm{N}^3 \qquad \text{Eq 2.3}$$

Where δ is avalanche ionization, which is function of temperature of electron T_e and can be defined as $\delta(T_e) = 3.6 \times 10^{10} \exp(-1.5E_g / K_B T_e)$, where E_g is the bandgap energy. Physically, Auger recombination mechanism is the reverse process of impact ionization and it should remove the heat effects of Auger recombination. The maximum generation rate of avalanche ionization rate is $2.3 \times 10^5 s^{-1}$ and melting temperature of Si is 1600K. The Auger recombination rate is $7.8 \times 10^{17} cm^{-3}$ which is already the same as this rate. We indicated prior, the carrier densities are two orders of magnitude higher than this equilibrium density, removing avalanche ionization as an important mechanism for carrier generation. So, Eq 2.2 is the final formula for the free carrier densities.

2.1.2 Nonlinear mechanisms of heat generation and temperature profile in silicon

In the same way, the carrier density profile analyzed in the previous section, we need to express heat generation mechanism and diffusion to find the thermal profile in silicon. Thermal issues is critical and important in Si photonics [63]. The temperature varies with respect to the heat equation,

$$\rho C_p(T)\frac{dT}{dt} - \nabla.(\kappa\nabla T) = Q \qquad \text{Eq 2.4}$$

Where, ρ density of Si (gr/cm^3), $C_p(T)$ is the specific heat [64], κ is the thermal conductivity ($1.6\, W/cmK$) [65]. T is lattice temperature and Q is the heat generation rate. Since heat diffusion length define as $L_{diff} = \sqrt{6D_{heat}\tau_{pulse}} \ll S$, where S is spot size of the laser and $D_{heat} = \kappa/\rho C_p$. Therefore, the left side of Eq 2.4 can be eliminated and the heat generation turn into ΔT. The laser beam transfers its energy to the electrons during the interaction between laser irradiation and Si material. These carriers lead to electron-electron collision events quickly thermalized. After thermalization, carriers transfer the external heat to the lattice. Thermal equilibration occurs on a time scale while temperature differences between carriers and lattice balanced. In Si, Carrier-phonon relaxation time is less than 500 fs [66]. In our experiment, the nanosecond pulses which are larger than the relation time are used. Therefore, in that case, we can regard as heat temperature between lattice and electron carrier are in equilibrium ($T_e = T$).

Accordingly, we can categorize the heat generation mechanism and their effects in Si as given below:

1. TPA based heating

   Two photon absorption process occurs when the total energy of incident two photons is larger than energy bandgap of Si ($2\, h_f - \mathrm{E}_{gap}$), lead to excite electron and the remaining energy induce heat the sample. The heating rate of TPA is:

$$Q_{TPA} = \beta I^2 (1 - \frac{\mathrm{N}}{\mathrm{N}_{at}})(1 - \frac{E_{gap}}{2E_{photon}}) \qquad \text{Eq 2.5}$$

Where, E_{photon} is total energy of absorped photon and E_{gap} is the energy bandgap.

2. Auger recombination based heating

Auger recombination generate heat mainly in the material. For the carrier densities which is ($\mathrm{N} > 10^{18} cm^{-3}$), Auger recombination is the main recombination process, because of three-body interaction in which two carriers recombine, and excess energy transfers with a third carrier taking up the recombination energy. The mechanism of heating rate is [67]:

$$Q_{rec} = E_{gap} \gamma^3 N^3 \qquad \text{Eq 2.6}$$

3. Free carrier absorption (FCA) based heating

Free carrier induced by TPA are unavoidable in Si by incident optical density, resulting in FCA, which are collected in Si. Further free carrier generation leads to the interband absorption in Si. Therefore, intraband absorption leads to nonlinear absorption profile and induces heat. Notice that because of Kramers-Kronig relations, the heat effect induced by FCA lead to decrease optical refractive index in the real part, namely the free carrier index (FCI) vary. These changes in the free charge carrier absorption coefficient ($\Delta\alpha_{FCA}$) and density of free charge carrier index (Δn_{FCI}) can be calculated by Drude model [68].

$$\Delta\alpha_{FCA} = \frac{e^3 \lambda^2 \Delta \mathrm{N}}{4\pi^2 c^2 \epsilon_0 n} (\frac{1}{m^*_{ce}\, 2_{\mu_e}} + \frac{1}{m^*_{ch}\, 2_{\mu_h}}) \qquad \text{Eq 2.7}$$

$$\Delta n_{FCI} = -\frac{e^2 \lambda^2 \Delta \mathrm{N}}{8\pi^2 c^2 \epsilon_0 n} (\frac{1}{m^*_{ce}} + \frac{1}{m^*_{ch}}) \qquad \text{Eq 2.8}$$

It is seen that both free charge carrier effects are supposed to be linear in density of charge carrier. Because of mobilities of electron/hole (μ_e, μ_h) and effective carrier masses (m^*_{ce}, m^*_{ch}) dependent on temperature effect lead to $\Delta\alpha_{FCA}$ and Δn_{FCI} effects to temperature dependence. For Si, carrier mobilities depend on temperature, however the effective masses depend on weakly temperature and established by the band structure. Therefore, we consider Δn_{FCI} not to change by temperature while $\Delta\alpha_{FCA}$ is temperature dependence. In Eq 2.8, Δn_{FCI} is considered to vary just by 15% between room temperature (RT) (300K) and melting temperature of Si (1600K). Therefore, FCI is negligible due to dependence on temperature.

In the literature, the empirical parameters of $\Delta\alpha_{FCA}$ and Δn_{FCI} written as [69]:

$$\Delta\alpha_{FCA} = \Delta\alpha_h + \Delta\alpha_e = 0.51 \times 10^{-20}\lambda^2 TN + 1.01 \times 10^{-20}\lambda^2 TN \quad \text{Eq 2.9}$$

$$\Delta n_{FCI} = -[8.8 \times 10^{-22}N + 8.510^{-18}N^{0.8}] \quad \text{Eq2.10}$$

Where, T is the equilibrium temperature and λ is the wavelength of incident photon, display independent temprature for Δn_{FCI}. heating induced by FCA is written as $Q_{FCA} = \Delta\alpha_{FCA}I$.

The total heat generation value is the collection of all the mechanisms explained here and it is indicated as $Q_{FCA} = Q_{TPA} + Q_{rec} + Q_{FCA}$. It should be noticed that carrier for creating subsurface modification in Si structures.

2.1.3 Light propagation in silicon

Light propagation and Interaction of counter-propagating beams in Si can be achieved with an approximation that determines Maxwell equations like as Finite Element Method (FEM) or Finite Difference Time Domain (FDTD). However, the nonlinear effect of coupled mechanism of heat and carrier generations in Si increments the complexity of these methods. Since, thickness of Si wafer is three orders of magnitude higher than the laser wavelength, FEM/FDTD methods be essential for computational power. So, the nonlinear paraxial equation (NPE) describes the crucial beam propagation and evolution in Si. The NPE equation is written as [70]:

$$\frac{\partial A}{\partial z} = \frac{i}{2k}\nabla_T^2 A + \frac{ikA}{n_0}(\Delta n_{total} + i\Delta k_{total}) \quad \text{Eq 2.11}$$

In Eq 2.11, k is the wave vector, n_0 is the ambient refractive index, A is the distribution of electeric field, Δn_{total} represent total change in real parts of refractive index and Δk_{total} is the total change in the imaginary parts of refractive index. Δn_{total} can be disintegrated into three different parts:

$$\Delta n_{total} = \Delta n_{Kerr} + \Delta n_{FCI} + \Delta n_{Thermal} \qquad \text{Eq 2.12}$$

Where, Δn_{Kerr} symbolizes the variation of refractive index caused by the Kerr response of Si and written as $\Delta n_{Kerr} = n_2 I$, where n_2 is the Kerr coefficient. For Si at the wavelength of 1.5 µm can be write as $n_2 = 5 \times 10^{-14}\ cm^2/W$ [71].

Δn_{FCI} define the variation of refractive index due to free carrier. Δn_{FCI} can be considered as $\Delta n_{FCI} = -[8.8 \times 10^{-22}\mathrm{N} + 8.5 \times 10^{-18}\mathrm{N}^{0.8}]$ from Eq2.10. $\Delta n_{Thermal}$ is the variation of refractive index based thermal effect. The correlation between the variation of reflactive index and the temperature change is written as [72,73]: $\Delta n_{thermal} = 1.86 \times 10^{-4}\Delta\mathrm{T}$.

The total variation of refractive index in the imaginary part can be disintegrated as follows:

$$\Delta k_{total} = \Delta k_{TPA} + \Delta k_{FCA} \qquad \text{Eq 2.13}$$

Where, TPA loss lead to Δk_{TPA}. The variation of refractive index in the imaginary part can be shown as $\Delta k_{TPA} = \frac{\alpha_{TPA}\lambda_0}{4\pi} = \frac{\beta I \lambda_0}{4\pi}$. For TPA in Si, the attenuation coefficient (cm^{-1}) is $\alpha_{TPA} = \beta I$.

Δk_{FCA} this term defines as the generated charge carriers increment absorption relative to free carrier absorption. The correlation between the free carrier densities and the absorption coefficient (cm^{-1}) is calculated as $\Delta\alpha_{FCA} = \Delta\alpha_h + \Delta\alpha_e = 0.51 \times 10^{-20}\lambda^2 TN + 1.01 \times 10^{-20}\lambda^2 TN$. Notice that for high carrier densities, the same densities is valid for free electron and hole pairs. The variation of refractive index in the imaginary part given as: $\Delta k_{FCA} = \alpha_{FCA}\lambda_0/4\pi$.

2.1.4 Light propagation under nonlinear feedback conditions in silicon

Two primary diffractive effects, which are $\Delta n_{thermal}$ leads to thermal lensing and Δn_{FCI} leads to FCI diffraction, responsible for subsurface modification in Si. the effect of thermal lensing is not prominent for single pulse laser at the case of low intensities or weak focusing, FCI diffraction hinders self-focusing, and therefore no subsurface modification is occurred. Despite that, the contest between these two contradicting diffractive effects can be gain by thermal lensing when two counter-propagating laser pulses nonlinearly couple including a self-focusing feedback condition. In the experiment, this process is originated when the incoming beam from inside the Si couples with reflected beam from the interfaces of Si-air. in that situation, even at low power, a single laser pulse self-focuses and subsurface modification is created. By every incoming laser pulse, the previously modified regions lead to partially shifted position and cause the process starts again on the next pulse propagation. Due to this, modifications elongate with every laser pulse, lead to create high aspect ratio features, like as moving-focus model in filamentation [74]. Here, we performed a model with a single laser pulse propagation to create subsurface modification under nonlinear feedback conditions.

2.1.4.1 Implementation of single laser pulse model

The method we implement to achieve free carrier distributions and temperature profile should be able to manage both nonlocal feedback and high optical nonlinearities. Hence, we prefer split step Fourier method, which is a conventional tool numerically clarify nonlinear differential equations [75]. Summarily, the method propagates linear and nonlinear parts independently, for each small step. For individual steps, the linear part is clarified precisely in the frequency domain, while nonlinear part is considered in the spatial domain [75]. The FCI leads to generate a nonuniform refractive index profile by excitation of free charge carrier due to the propagation of laser pulse in Si. In the same direction, intraband TPA and FCA absorptions lead to heating will change the refractive index of Si. These two contradicting diffractive effects will frequently modify the propagation of laser beam, make the numerical implementation difficult. In the simulations part, the round trip time calibrated $\approx 10\,ps$ by consideration of thickness of the Si 500 µm. At the same time, we can deliberate the refractive index, temperature, and free carrier distribution quasi-stationary. The diagram of the pulse propagation is given in Figure 2.2.

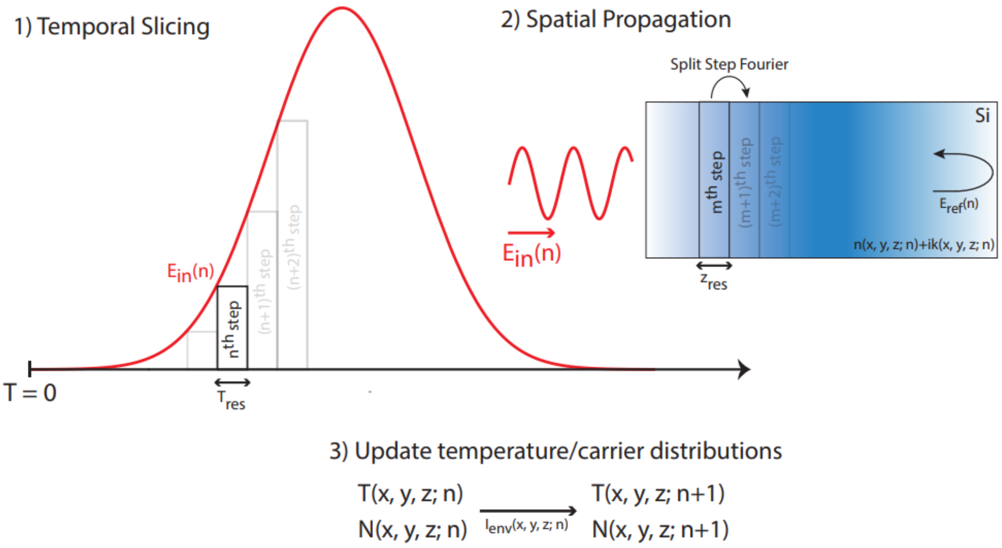

Figure 2.2. For individually temporal slice, the intensity distribution (I_{env}) is calculated by considering the free carrier distribution, temperature, and refractive index from the previous iteration [59].

As an input data from the previous iteration, for individual temporal slice, the I_{env} in Si is achieved by calculating the split step Fourier method, with consideration of free carrier density (N), temperature (T) with refractive index (n_{total}, k_{total}). In the first, the linear part of the field is propagated by half of the spatial resolution ($\Delta z/2$) and the nonlinear part is propagated for a length of Δz. For another ($\Delta z/2$) the calculation is finalized by propagating the linear part of the field. For individual temporal slice until the total time is equivalent to pulse duration this method is iterated. it must be noticed that by interaction of two counter propagating pulses, leads to form an interference pattern. At the same time, an interference pattern will form, with an oscillatory period of $\lambda_{si}/2 = 225\,nm$. The length scale of these oscillations is not much higher than both the spot size of incident beam and the diffusion lengths. For this reason, the intensity envelope (I_{env}) in the simulation part used as:

$$\mathrm{I}\alpha\left|E_{forward} + E_{backward}\right|^2 \leq \left(\left|E_{forward} + E_{backward}\right|\right)^2 = I_{env} \qquad \text{Eq 2.14}$$

2.1.4.2 Outcomes of single laser pulse simulation

In the experiment, we realized that subsurface modification did not occurs by sending weakly focused, low power beam. this effect observed with a second, counter-propagating beam, specifically a dressing beam. In an attempt to prove the creation of subsurface modification thank to the second beam (dressing beam), two alternatives were simulated. For the first alternative, for the first alternative, a single pulse is poorly focused inside Si, devoid of a dressing beam. In the second scenario, a counter-propagating dressing beam is combined to track the nonlinear coupling among the beams.

Experimentally, we accomplished the second scenario by focusing the laser beam on the existence side of the surface, in order that 30% of incoming laser beam is reflected back from the air-Si interface, creating the counter propagating beam. Even if, the energy of incoming beam (dressing beam) (14 µj) has greater than the reflected beam (4.2 µj), its peak density is lower considering the beam is focused outside the sample and the diameter of the beam have bigger at the interaction region.

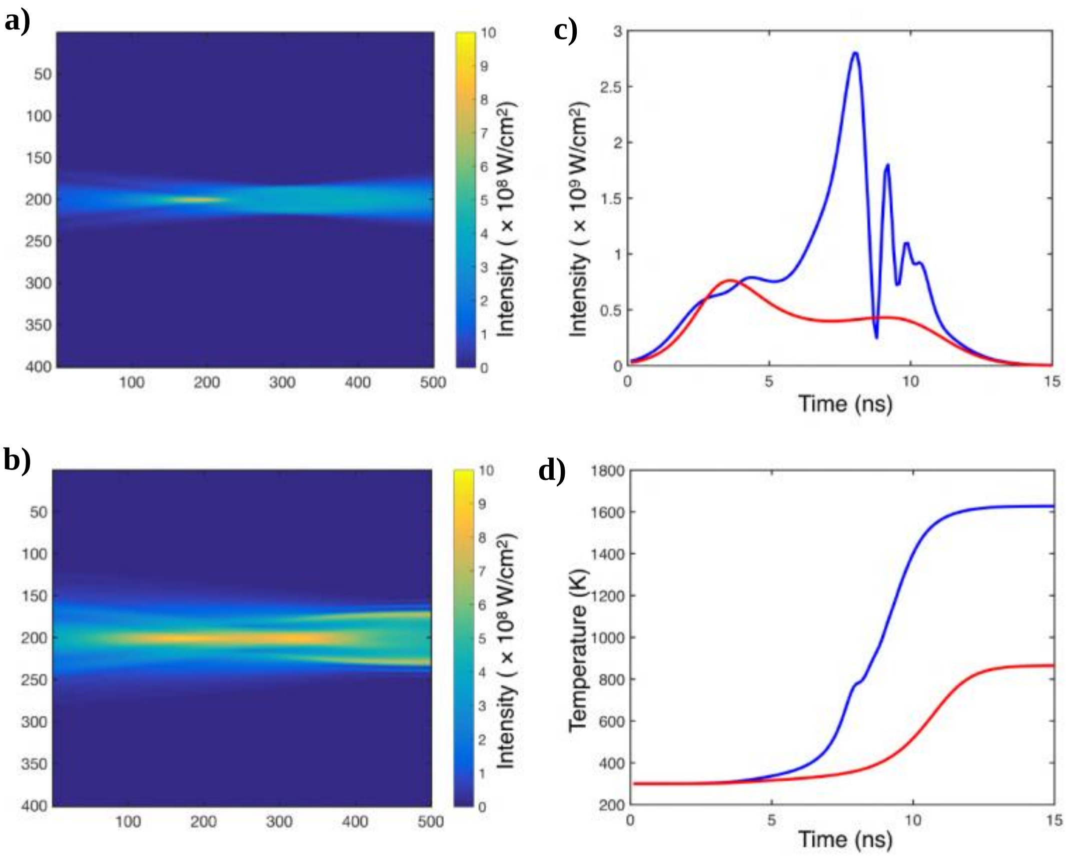

Figure 2.3 Simulations of single laser pulse propagation in Si. Intensity distribution for the undressed beam case (a). Intensity distribution of the dressed beam case (b). Intensity evolution on a location where modification occurs. The blue graph shows the dressed beam case, and the red graph for the undressed case. The double peak is caused by the thermal lensing delay, which becomes effective in a few ns after FCI. This implies that the two effects are in competition. (c). Thermal evolution in the area of modification. Temperatures approach the melting temperature of Si in the dressed beam case (blue graph), but are restricted to 800 K in the undressed beam case (red curve) (d) [59].

The simulation results show that increments of both temperature and beam intensity are restricted in the undressed beam scenario. FCI lead to diffracted beam in the first few nanoseconds Figure 2.3 (c). Thermal nonlinearity effect leads to start beam focusing after a few nanoseconds. The delay between mechanisms is predicted. The heating mechanism is because of intraband absorption which is resulted by two-photon absorption causing to the generation of free carriers requirement. The double peak as a result of the delay in the thermal lensing, that is valid a few nanoseconds after FCI (see Figure 2.3 (c)).

In the second scenario Figure 2.3 (b), only by adding a counter-propagating dressing beam, the simulation condition varied. in this condition, after a particular delay because of nonlinear coupling between the laser beams, intensity attains the experimentally realized threshold rate, and temperature raises to the melting temperature of Si (T=1600 K). The reason for morphology variation in Si leads to a dramatic increment in the beam intensity with self-focusing [76]. However, in the undressed beam case red graph in Figure 2.3 (d), maximum temperature is restricted to 800 K.

2.2 Explanation of the toy model

In point of fact, three dimensions (3D) buried or in-chip functionalities produced with no damaging wafer surfaces have not been recognized to date and opens novel feasibility to enable applications in various fields. A promising direction to accomplish present restrictions in producing controllable structures in Si is to investigate the rich nonlinear effects of the interacting optical beams with intimations in various fields. For example, thermally coupled wave packets have been presented to follow nonlinear gravitational effects [70]. In a similar way, we take advantage of the nonlinear effects of thermally coupled beams to authorize the production of subsurface functional structures in Si.

To analyze the creation of structure and elongation in Si, we developed a simple model named a toy model. The model captures the characteristics of the modification regions in Si, which are experimentally verified. the three primary claims of the toy model, including (i) feedback mechanism due to the counter-propagating beam leads to create structures (ii) nonlinear feedback leads to every laser pulse elongate into structures along the optical axis (iii) for high numbers of the laser pulse, before creating damage on the surface occurs, the elongation saturates.

We pursue an approach identical to the mathematical induction method. we first begin by the implementation of a single pulse condition, latter with two pulse condition, and lastly, broaden to any pulse numbers. Nonlinear paraxial equation

(NPE) and heat equation control the propagation of the laser pulse, as described in specific in section (2.1.3). In summary, Δn_{total} term in Eq 2.11 illustrates the feedback among two contradictory effects coming from thermal nonlinearity and variation of refractive index induces free carrier.

Extra incoming pulses mobilize the second feedback: every pulse creates modification as locally; this modification cause shifts the focal point for the following pulse like a moving focus model of self-focusing. We consider the self-induced lensing responses through pulse propagation which can be explained with two concatenated thin lenses, including f_{therm} and f_{FCI} that respectively define a positive focal length and a negative focal length. After focusing the first laser pulse in Si and which causes the creation of the local modification volume, caused by various optical properties in this volume, the focal position of the other pulse is changed the position concerning the prior pulse. The focal translation is calculated from lens equation, written as $\frac{1}{l_2} = \frac{1}{f_t} + \frac{1}{l_1}$, where l_2 represent the focal position of the second laser pulse, and $l_1$indicate the focal position of the first laser pulse and f_t is the shift in the total length per pulse, shown as $f_t = \frac{f_{therm}}{1+\eta}$. Here, we present $\eta = \frac{f_{therm}}{f_{FCI}}$, which is competition measurement among the self-induced lenses. For thermal nonlinearity to accomplish FCI effects and start to create subsurface modification, we consider $-1 < n < 0$, else $n < -1$. By extending of n^{th} modification, l_n can be achieved as $\frac{1}{l_n} = \frac{n-1}{f_t} + \frac{1}{l_1}$. In this condition, the total length of the subsurface modifications caused the total focal shift which is given as:

$$\delta l_n = \frac{l_1^2(n-1)}{f_t + l_1(n-1)} \qquad \text{Eq 2.15}$$

In Eq 2.15, f_t is the merely unknown term to determine the total structure length. f_t is a function of positive focal length f_{therm} and negative focal length f_{FCI}. Because of these beams, carrier density and temperature profiles are needed to determine the self-induced variations of the refractive index in Si. After the first laser pulse propagation, the total change in carrier density, δN_{tot}, which is given as:

$$\delta \mathrm{N}_{tot} = \delta \mathrm{N}_1 + \delta \mathrm{N}_2 + \delta \mathrm{N}_3 \qquad \text{Eq 2.16}$$

Where, $\delta \mathrm{N}_1$, $\delta \mathrm{N}_2$ and $\delta \mathrm{N}_3$ indicates forward beam propagation, backward beam propagation and their coupling due to generation of carrier densities, separately. In the condition of incoming beam is Gaussian, change in carrier densities are written as:

$$\delta N_i(z,r) \approx \frac{\beta \mathrm{I}_i^2(z)\delta t}{2\mathrm{E}} e^{\frac{-4r^2}{w_i^2(z)}} \qquad \text{Eq 2.17}$$

Where, E is the energy of photon, δt indicates pulse width, I defines the intesity, β shows two photon absorption coefficient, r is the radial distance. Hence, induced charge carriers cause the total refractive index profile is written as:

$$\delta n_{FCI}(z,r) \approx -\mathrm{A}\delta \mathrm{N}_{tot}(z,r) = -\sum_{i=1}^{3} \frac{\mathrm{A}\beta \mathrm{I}_i^2(z)\delta t}{2\mathrm{E}} e^{\frac{-4r^2}{w_i^2(z)}} \qquad \text{Eq 2.18}$$

Here, $\mathrm{A} = 8.8 \times 10^{-22} cm^3$ keeps constant [77]. However, the equal spatial profile for intensity and total temperature is considered, the temperature varies caused by the laser pulse is written as:

$$\delta T_i(z,r) \approx \frac{\beta \mathrm{I}_i^2(z)\delta t}{\rho \mathrm{c}} e^{\frac{-4r^2}{w_i^2(z)}} \qquad \text{Eq 2.19}$$

Where, c is specific heat capacity and ρ is density. Therefore, temperature variation leads to refractive index variation is:

$$\delta n_{therm}(z,r) \approx \sum_{i=1}^{3} \frac{\beta \mathrm{I}_i^2(z)\delta t}{\rho \mathrm{c}} \frac{d_n}{d_T} e^{\frac{-4r^2}{w_i^2(z)}} \qquad \text{Eq 2.20}$$

We refer to an approximation of paraxial ray, broaden the values throughout the optical axis and maintain the first two values for $\delta n_{FCI}(z,r)$ in Eq 2.19 and $\delta n_{therm}(z,r)$ in Eq 2.20, which supply

$$\delta n_{FCA}(z,r) \approx -\sum_{i=1}^{3} g_i(z)\left(1 - \frac{4r^2}{w_i(z)^2}\right) \qquad \text{Eq 2.21}$$

$$\delta n_{therm}(z,r) \approx \sum_{i=1}^{3} h_i(z)\left(1 - \frac{4r^2}{w_i(z)^2}\right) \qquad \text{Eq 2.22}$$

Where, $g_i(z) = \mathrm{A}\frac{\beta \mathrm{I}_i^2(z)\delta t}{2\mathrm{E}}$ and $h_i(z) = \frac{\beta \mathrm{I}_i^2(z)\delta t}{\rho \mathrm{c}}\frac{d_n}{d_T}$ are $\delta n_{FCI,i}(z,0)$ and $\delta n_{therm,i}(z,0)$, separately. To make easier our model, we average these values over the propagation direction z, and the form of refractive index profiles get to be,

$$\delta\bar{n}(r) = \delta\bar{n}_0(1 - \frac{4r^2}{\bar{w}^2}) \qquad \text{Eq 2.23}$$

With $\bar{n}$, $\bar{w}$ illustrate average values upon the z-axis.

We can present matrix optics formalism, which will perform to characterize the ray paths of the paraxial beam in a medium, where the refractive index depends on the r. The paraxial ray equation for this condition shown as:

$$\frac{\partial n}{\partial r} = n(r)\frac{d^2r}{dz^2} \qquad \text{Eq 2.24}$$

By implementing Eq 2.23 into Eq 2.24, we achieve the pulse propagation equation as follow:

$$\frac{d^2r}{dz^2} + z_0^2 r = 0 \qquad \text{Eq 2.25}$$

Where z_0^2 define as $z_0^2 = \frac{8}{\bar{w}^2}$. This equation supplies the transmission matrix of the medium [78]

$$T = \begin{bmatrix} \cos(zz_0) & \frac{1}{z_0}sin(zz_0) \\ -z_0 sin(zz_0) & cos(zz_0) \end{bmatrix} \qquad \text{Eq 2.26}$$

It could be demonstrated [78,79] that the T matrix is equal to a lens with a focal length of f:

$$f = \frac{1}{\delta\bar{n}_0 z_0} \qquad \text{Eq 2.27}$$

We consider the variation of the refractive index for forward and backward beams propagation is equivalent and demonstrate two coefficients, α and γ, which indicate the strength of coupling values in Eq 2.21 and Eq 2.22, as $\bar{g}_3 = \alpha\bar{g}_1 = \alpha\bar{g}_2$ and $\bar{h}_3 =$

$\gamma\bar{h}_1 = \gamma\bar{h}_2$, where α and γ are strength of coupling values. Hence, f_{therm} and f_{FCI} can be written as:

$$f_{FCI} \approx -\frac{1}{\delta\bar{n}_{0,FCI} z_0(2+\alpha)} = \frac{2\mathrm{E}}{\mathrm{A}\beta\mathrm{I}^2\delta t z_0(2+\alpha)} \qquad \text{Eq 2.28}$$

$$f_{therm} \approx \frac{1}{\delta\bar{n}_{0,therm} z_0(2+\gamma)} = \frac{2\mathrm{E}}{\beta\mathrm{I}^2\delta t \frac{dn}{dT}(2+\gamma)} \qquad \text{Eq 2.29}$$

The model proposes that the subsurface modification without feedback mechanism, which is impossible due to a counter-propagating beam (claim 1). To think of this, we get rid of the coupling beam value to zero, $\alpha = \gamma = 0$ and we implement in Eq 2.28 and Eq 2.29, for instance, $\lambda = 1.55\ \mu m, \varpi = 30\ \mu m, \delta t = 5\ ns$ and $\mathrm{E} = 10\ \mu j$. We determined variations of refractive index and the focal lengths like as $\delta\bar{n}_{0,FCI} = -8.3 \times 10^{-5}$ and $\delta\bar{n}_{0,therm} = 1.4 \times 10^{-6}$, $f_{therm} = 7.4 \times 10^{6}\mu m$ and $f_{FCI} = -2.5 \times 10^{5}\mu m$. From these outcomes, $\eta = \frac{f_{therm}}{f_{FCI}} \approx -30$ is identified, which cannot meet the structure creation case of $-1 < \eta < 0$.

This claim could be investigated experimentally by removing the back surface reflection, which is responsible for the counter-propagating beam. the back surface is deposited by an anti-reflection coating such that the focused beam does not back reflection into the Si sample (Figure 2.4 (a)). The laser is processed through the interface between double-side polished Si and the anti-reflected coated regions. As expected, the subsurface modifications did not create in the anti-reflected region because of the lack of feedback. Silicon nitride (SiN_x) is deposited with a thickness of 200 nm as an anti-reflection coating. Therefore, it causes the focused beam can pass through the back surface of Si with no reflection (Figure 2.4 (b)).

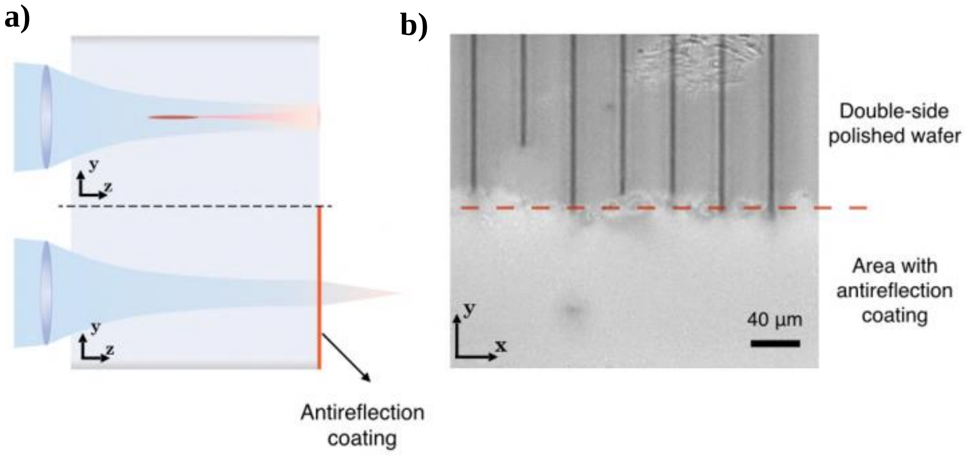

Figure 2.4 The pulse propagation for the cases with and without counter propagating beam (a), Image of IR transmission microscope that shows the subsurface modification only in double-side polished region (b) [59].

The model also expects that modifications create and elongate, pulse to pulse, throughout the optical axis (claim 2), In addition, self-regulate with increasing the number of laser pulses, their elongation leads to saturate and stop before creating damage on the surface (claim 3). In this model, we implement nonzero α and γ by considering $-1 < \eta < 0$. The laser beam incident with the various number of the pulses to generate subsurface modifications and measured the structure lengths. The comparison as a function of the structure length between the experimental data and expected by the model is analyzed (Figure 2.5). To fit the data, we utilized $f_t = 26\ mm$ and consider for simpleness the same size of the pulse and intensity for both forward and backward beams. We can predict α and γ from Eq 2.28 and Eq 2.29 given as:

$$\gamma = \frac{f_{therm}^0}{f_t} - \alpha \frac{f_{therm}^0}{f_{FCI}^0} \qquad \text{Eq 2.30}$$

Where, f_{therm}^0 and f_{FCI}^0 are the thermal and induced focal lengths respectively by considering on of the beam is turned off with no feedback condition.

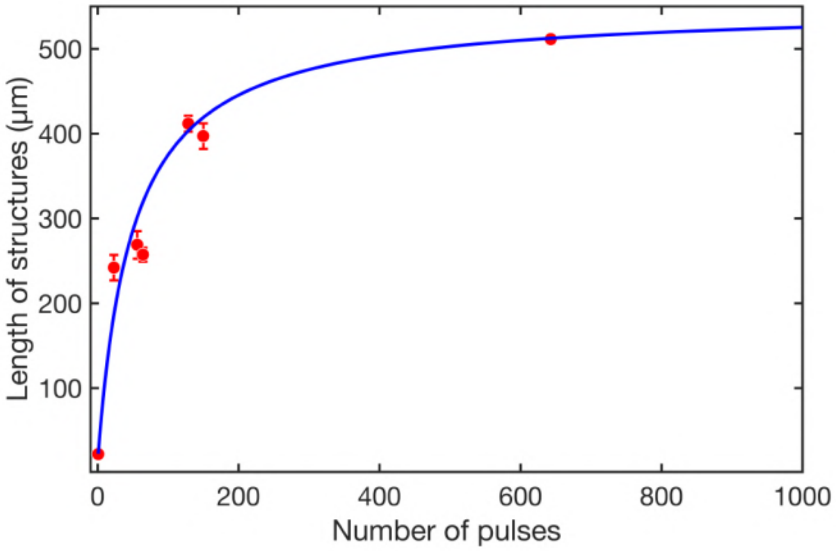

Figure 2.5 Experimental data (red circles) and toy model expectation (blue graph) [59].

By controlling of this level allows us leads to form subsurface structures with various aspect ratios, as seen in Figure 2.6. for example, we indicate different laser pulses such as 20 and 200, which make a formation of the long and short subsurface modification (Figure 2.6 (a)). The first pulse for each is self-focused in Si, and is signed with (orange) for 20 and (blue) for 200 pulses. As expected for the toy model, every pulse laser caused the structures to elongate throughout the optical axis. However, for the high number of laser pulses, the structures self-regulate and stop before approaching the surface of Si.

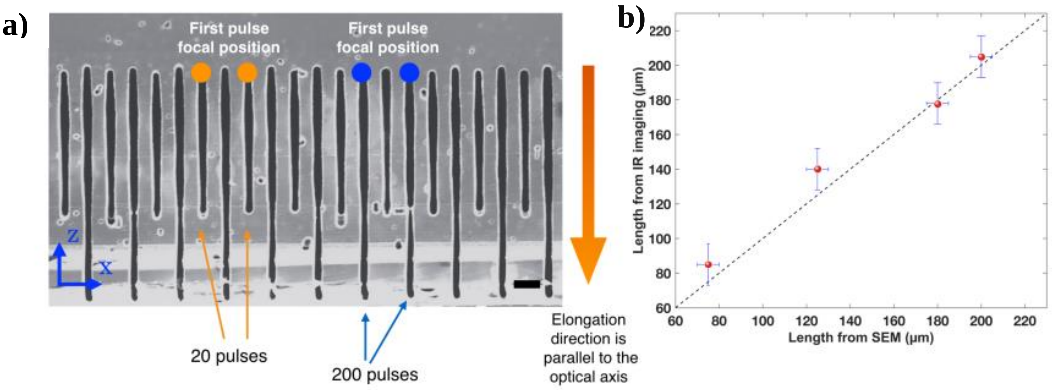

Figure 2.6 Controlled structures formed by various number of laser pulses. Scanning Electron Microscope (SEM) images shows high aspect ratio of subsurface structures

are created with (orange) for 20 and (blue) for 200 pulses (a). The scale bar is $40\mu m$. the comparison of structure length measurements from both SEM images with *in-situ* measurements and IR transmission microscopy (b) [59].

The embedded features in Si are also diagnosed in-situ. The positions of subsurface structures and their aspect ratios are specified by infrared (IR) transmission microscopy. In (Figure 2.6 (b)), the comparison measurements from both IR microscopy and SEM methods shows a great agreement and represent that the analysis of the length measurements are very credible.

2.3 Silicon etching

Recently, high-aspect-ratio Si micro and nanostructures are of great interest for their potential applications in various fields scoping from photonics, MEMS, and renewable energy to biomedical sensing. There are several methods to create micro and nanostructures on Si. Conventional fabrication methods include wet chemical etching (isotropic or orientation-dependent) using both acids and bases to remove the Si atoms, and dry chemical etching (anisotropic) such as reactive ion etching (RIE), plasma etching, and ion etching. There have been several attempts to create new 3D Si structures such as micro channels, hole drilling, and related nanodevices. Accordingly, as an alternative “top-down (etching)” approach, metal assisted wet chemical Si etching (MACE) [80–83], is examined as a promising solution to produce high aspect ratio [84] micro and nanostructures with well-defined controllable shapes, sizes, diameter, length, and various 3D complexity. There is an increasing interest in 3D structures with maskless and non-lithography which enable the fabrication of subsurface features with simple process, high throughput at room temperature and low cost. One of the primary goals of this study is to fabricate subsurface (buried) 3D structures using MACE. A dedicated and repeatable MACE process is required to remove the laser-modified subsurface regions selectively. The etching solution must perfectly have selective reactive behavior to defects, laser modified part, and perform at room temperature while keeping stable over long times. Additionally, in this approach it is possible to control the depth of the structures which is crucial for photonic application [85], metamaterials [86,87], micro-pillars [88], micro-holes [89,90], or microfluidics [91] applications, by tailoring the etching parameters such as chemicals concentration, etching time, etc. [92–94], which are hardly obtainable by any other fabrication processes. This section will explain the mechanism of MACE.

2.3.1 Metal assisted chemical etching

For Si-based micro and nanofabrication technology, the etching of Si during processing is essential in order to produce micro- and nano- structures productively. MACE is a disruptive technology that is, on the basis, a wet chemical method. However, it can create adjustable aspect ratios, etch rate, selectivity with minimum (defect-free) damage on Si surface. Besides, Si surface texturing is a necessary step to reach low surface reflectance from Si which is important to attain efficient c-Si solar cells. Commonly, the surface texturing structures on a Si solar cells are primarily upright pyramid arrays produced by the one-step alkaline etching (KOH) technique by anisotropic etching of the mono c-Si surface [95]. For texturing of multi-crystalline Si (mc-Si) wafers with different crystallographic orientations between the grains, anisotropic alkaline etching is not applicable. Instead, a MACE process has been generally used to fabricate both c-Si and mc-Si solar cells [96]. However, to improve absorption, ARC, and light trapping in photoelectric conversion efficiency, new structures such as b-Si, inverted pyramid, and porous Si (PSi) surface have become a very promising direction of the conventional c-Si solar cell applications. According to this, Si solar cell fabrication is shifting from microtextured to nanostructures which lead to modified surfaces with intensely high light absorption and low reflectivity [97]. The nano structuring is produced by various techniques using top-down or bottom-up approaches such as lithography [98], laser-chemical [99], electrochemical [100], reactive ion etching (RIE) [101],vapor–liquid–solid growth method (VLS), or vapor deposition [102]. By achieving these techniques, the complexity and corresponding additional costs inhibit the implementation of nanostructures in mass production or less competitive against wet chemical micro- or nano- structuring technology. Among these methods, the MACE [103,104] has been favored in the formation of different Si nanostructures because of simplicity, low energy consumption, potential in large-area fabrication, and controllable features such as shapes and sizes. Metal-assisted catalytic etching process does not require expensive and complicated lithographic process, since it is carried out in chemical solution by simply controlling etching time and concentration of etchant at room temperature. The MACE can be classified as a two-step [83] or one-step process [105]. In a conventional two-step MACE process, a noble metal catalyst like Au, Pt, Pd or Ag [82] is deposited on the Si substrate as either a thin layer or nanoparticles that locally increment dissolution of Si in the mixture of hydrofluoric acid (HF) and an oxidative agent in the aqueous etching solution. The Si beneath the metal is etched much faster than that without metal coverage. As a result, the metal immerses into the Si surface, leads to the creation of wires and pores. To reduce the fabrication process of nanostructures, one-step MACE process based on two-step MACE was enhanced. In the one-step MACE process, a chemical etching solution containing HF and metal salts. And consequently, the metal nanoparticles (NPs) formed on the Si surface accelerates the oxidation rate of Si beneath them. The oxidized Si is etched by HF into the solution of H_2SiF_6, which leads to creating pits on the Si surface.

Among metal-based etching processes, the Cu metal-assisted etch catalyst has several benefits over Au or Ag. Cu metal, in contrast to Au and Ag, is used extensively in commercial Si microfabrication equipment. Even though there is no proof that recombination because of the residual impurities leads to loss in solar cell efficiency, different experimental studies propose that Cu metal impurities in Si are usually less damaging to the efficiency of solar cells than that of Au [106] and Ag [107]. Putnam et al. represented that VLS grown Si nanowires implying Au catalysts have a shorter minority carrier diffusion length with four micrometers than those produced using a Cu catalyst with ten micrometers [106]. Besides, Kuzma-Filipek et al. indicated that epitaxial Si solar cells by Cu electroplating as front metal contacts profit from lower dark current density than cells with Ag screen-printed metal contacts [107]. Finally, to decrease the cost, copper was used instead of the expensive noble metals as the metal catalyst [108].

The facile one-step copper assisted chemical etching (Cu-ACE) process can be applied to produce a micron size random inverted pyramids [109] on c-Si because of its impressively anisotropic etching characteristic on large scale. The inverted pyramid structure achieved major light-absorbing and low surface area capability that produced by using maskless Cu-nanoparticle assisted etching [109]. Besides that, different nanostructures have also been developed through the Cu-ACE process, involving nanowire [82], nanopore [110–113], and crater [111,113] structures illustrating that the cheaper Cu can be used as a substitute for the expensive Au or Ag in the MACE process for the texturing of mc-Si wafers. Accordingly, the Cu-ACE process can be applied as a universal surface texturing technique for all types of Si to produce structures with micro or nano sizes. More particularly, the Cu-ACE method has demonstrated many prominent advantages in texturing, having perfect cell performances, lower costs and variant facilities for mass production of both c-Si and mc-Si solar cells.

In this thesis, Cu-ACE will be applied to a new developing Si micro-processing technology which depends on direct laser modification of Si subsurface to produce 3D microstructures with potential functionalities in numerous fields of applications. Even though surface laser processing is a well-established technique to produce desired features on Si surface like laser-induced periodic surface structuring (LIPSS) which is utilized to achieve light trapping interfaces for solar cells [45,114–116] or fabrication black-Si [101], subsurface laser processing within the bulk of Si wafer [34] is still at its early stages where there is much to be explored.

Additionally, the Si subsurface structures have created by nanosecond fiber laser [33,88,117] for laser-induced silicon thin film slicing (LASIS) solar cell and subsurface 3D structure applications. For the first time, copper(II) nitrate - $Cu(NO_3)_2$ based etchant solution was presented to catalyze the Si etching for the selective removal of the laser-modified regions. Cu is commonly used as a material for conductors in microelectronics devices because of its high electrical conductivity and its lower cost than Ag. A Cu-assisted chemical etching process is described as a more economical route to produce a surface and buried (subsurface) nanostructures.

2.3.2 Mechanism of metal assisted chemical etching on laser modified region

We describe a mechanism of the one-step copper(II) nitrate - $Cu(NO_3)_2$ based etchant method using HNO_3 as a reducing agent in the mixture of HF, HNO_3, CH_3COOH, and H_2O with $Cu(NO_3)_2.3H_2O$ in the solution. The MACE mechanism including two reactions: first oxidation reaction of the semiconductor and secondly dissolution of the oxidized semiconductor. MACE is an electrochemical reaction with the metal part representing a cathode and the metal/semiconductor interface representing the anode. The process steps: 1) the existence of oxidant in the etching solution becomes diminished locally on the surface of the catalyst, where the metal acting leads to a decrease in the activation energy resulting in the reduction of the oxidant (gain of electrons), 2) the oxidant reduction by metal catalytically generates a hole in the metal and leads to the injection of holes into Si., 3) Si is oxidized by holes injection and etched by HF into soluble compound (H_2SiF_6) at the metal/Si interface. This results in the Si beneath the metal catalyst, until desired depth to be etched over time. Therefore, MACE processing results in the formation of higher aspect ratios and various surface and subsurface structuring.

Subsurface laser modified Si regions are intended to be selectively etched by $Cu(NO_3)_2$-based wet-chemical etching solution. The solution is a mixture of $Cu(NO_3)_2$, HNO_3, HF, CH_3COOH, and DI water. Copper(II) nitrate is used as a catalytic metal salt for developing selective MACE-based processing. The etching mechanism and expected reactions are as follows [82,118]:

Cathode reaction:

$$Cu^{2+} + 2e_{VB}^{-} \rightarrow Cu^{0}(s) \qquad E^0 = +0.34 \text{ V/NHE} \qquad \text{Eq 2.31}$$

$$HNO_3 + 3H^{+} \rightarrow NO + 2H_2O + 3h^{+} \qquad E^0 = +0.96 \text{ V/NHE} \qquad \text{Eq 2.32}$$

Anode reaction:

$$Si + 4HF_2^- \rightarrow SiF_6^{2-} + 2HF + H_2 + 2e^- \qquad E^0 = -1.20 \text{ V/NHE} \qquad \text{Eq 2.33}$$

$$Si + 2H_2O \rightarrow SiO_2 + 4H^+ + 4e^- \qquad E^0 = -0.84 \text{ V/NHE} \qquad \text{Eq 2.34}$$

$$SiO_2 + 6HF \rightarrow H_2SiF_6 + 2H_2O \qquad E^0 = +0.33\text{V/NHE} \qquad \text{Eq 2.35}$$

The selective property can be described by regarding the anodic reaction at the boundaries among c-Si and the modified regions. These modified regions are supposed to have electronically active defects and various dopant concentrations compared to c-Si, fabrication variations in the Cu^{2+} ion concentration. The difference in the etch rate among the metal interface and c-Si can be referred to this unequal profile of Cu^{2+} ions, which have a high electronegativity in contrast to Si (for Cu and Si is 1.9 eV and 1.8 eV, respectively) [119,120] allowing Cu^{+2} ions to obtain electrons from Si atoms. This effect causes the selective chemical etching behavior at the laser-modified sites. Eq 2.31 is the reduction of Cu ions at the surface of the cathode. In the mechanism, Si injects electron to adsorbed Cu. Eq 2.32 is the reduction of HNO_3 at the surface of the cathode which is faster at the presence of Cu nanoparticles. When HNO_3 is added to the solution, hole generation rate drastically increases and becomes higher than the hole consumption during the etching process. The Cu ions are reduced to solid Cu by attracting minority negative charge carriers available from Si in Eq 2.31 and Eq 2.32 are used either in the direct dissolution reaction of Si at anode (Eq 2.33) or in oxidation (Eq 2.34) followed by etching (Eq 2.35) of the formed ultra-thin SiO_2 on Si surface by HF [94,121]. After the etching process, Cu residuals on the surface are removed by HNO_3 treatment followed by SC2 cleaning [122]. Both Cu^{2+} and HNO_3 act as oxidants while Si serves as the reductant in abovementioned redox system. Although Si etching rate in HNO_3/HF solution is low in the absence of metallic Cu ions, etching is accelerated by adding few moles of $Cu(NO_3)_2$ as source of Cu ions. In this way, Si is oxidized to SiO_2 and etched by HF. In addition, HNO_3 oxidizes the Si surface forming SiO_2 which is etched by the presence of HF. In the solution, CH_3COOH acts as a diluent and reduces the overall reactant concentration.

CHAPTER 3

SELECTIVE CHEMICAL ETCHING

A new emerging Si micro-processing technology relies on direct laser modification of Si subsurface allowing for fabrication of 3D microstructures with potential functionalities in a vast range of applications. Although surface laser processing is a well-established technique to create desired features on Si surface such as laser induced periodic surface structuring (LIPSS) which is used to create light trapping interfaces for solar cells [45,115,116,123,124] or fabrication black-Si [125,126], subsurface laser processing within the bulk of Si wafer [29] is still at its early stages where there is much to be explored. In subsurface laser processing of Si ultra-short near to mid-infrared laser pulses are focused into the bulk of the wafer. The interaction of the intense localized laser radiation with Si induces non-linear effects such as multi-photon absorption, self-focusing, and plasma generation inside the focal volume [127–129]. The subsurface laser processing provides precise local modifications at the targeted sites regardless of Si crystallinity or orientation [13,130]. In this technique, the optimization of the laser parameters (i.e., laser wavelength, pulse duration, and pulse energy) enables precise control over the laser-Si interaction. The formation of subsurface structures using a nanosecond or femtosecond pulsed laser beam is a new approach for high-quality micro and nanofabrication applications. This method creates modification at localized regions with minor damage on the c-Si surface [19,131]. It is of great essence that such a special etchant is developed to selectively remove laser modified Si out of c-Si wafer in order to sculpt functional 3D structures. Similar to surface laser processing, a subsequent chemical etch is essential to reveal the subsurface structures without altering non-laser processed Si regions to meet the requirements of the aforementioned wide applications. Hence, the development of a tailored etchant with the desired properties including the selectivity (ratio of the removal rate of laser processed and pristine regions) and etch rate, are highly favorable. Thus far, typical defect etchant recipes comprise chromium (Cr)-based chemical solutions or nitric acid (HNO_3) which both serve as the oxidizing agent of Si surface. The latter is called the HNA comprising Hydrofluoric acid (HF), Nitric acid (HNO_3), and Acetic acid (CH_3COOH). While HNA based etching recipes are Si-crystallographic orientation and dopant type independent, they require highly doped Si to initiate the etching. Another HNO_3-based etching solution is the Dash etch (1956) [132], which is also crystallographic orientation and dopant type independent. However, it requires high-temperature processing and a longer etch duration ranging between 4-16 hours to effectively reveal the defects on Si surface. Other etchants with Cr-based oxidizing agents are named after their inventors- as Sirtl, Seiter, Wright, and Secco. The Sirtl etch (1961) [133] makes use of chromium trioxide (CrO_3) to delineate defects and dislocations in Si. In this chemical combination, CrO_3 replaces HNO_3 as a strongly oxidizing agent of the Si surface. However, it works well only for <111> oriented surfaces, while the Seiter etch (1977) [134] works well on <100> surfaces. In comparison, the Wright etch (1977) [135] is applicable to both <100> and <111> crystallographic planes and is applicable to both n- and p-doped c-Si. Wright etching solution includes $HF + CrO_3 + H_2O + HNO_3 + Cu(NO)_3 + CH_3COOH$. In this chemical solution, the oxidizing agents (the CrO_3 and HNO_3) oxidize the Si surface and HF dissolves the formed SiO_2, while adding a small amount of $Cu(NO_3)_2$, in particular, assists in reducing the resultant point defects. Therefore, the amount of $Cu(NO_3)_2$ in the mixture of the solution greatly influences the localized differential oxidation at the defect sites. The usage of CH_3COOH in the solution affects the etched Si surface, resulting in a smoother surface morphology. It has been demonstrated that CH_3COOH addition prevents the formation of bubbles during the etching process due to the wetting action. Finally, the Secco etch (1972) [136,137] consists of potassium dichromate ($K_2Cr_2O_7$), and its typical defect etching time is ~2 minutes. If the etching time exceeds 3 minutes, large fraction of Si will be removed due to over-etching. It etches defects on all crystallographic orientations of surfaces resulting in superior surface quality at high etch rates. A highly selective etching solution of Si defects in professional electronics industry is the MEMC etching

(Monsanto Electronic Materials Company - 1987) [138] which is a copper nitrate – $Cu(NO_3)_2$-based etchant and is applicable to both p- and n-doped Si. MEMC etching solution has a long lifetime during room-temperature processes which generates clear pits on <111> and <100> oriented surfaces. This solution has a planar etch rate which is identical for all crystallographic directions while the etching uniformity is like that of Sirtl, yet it is Cr-free. It is essentially used in destructive characterization of Si wafer quality in industrial applications.

In MEMC etch, the HNO_3 oxidizing agent oxidizes the Si surface and HF dissolves the formed SiO_2, while adding a $Cu(NO_3)_2$, in particular, assists in reducing the resultant point defects. Therefore, the amount of $Cu(NO_3)_2$ in the mixture of the solution greatly influences the localized differential oxidation at the defect sites. The usage of CH_3COOH in the solution affects the etched Si surface, resulting in a smoother surface morphology.

Among the various etch solutions used for Si etching, we adopted the MEMC etch to develop a special etchant for selective removal of laser modified Si. Furthermore, this solution is highly defect-sensitive and thus, sensitively “selective” to laser modified Si regions. The solution is crystal orientation and dopant type dependent. It takes reasonably short etch durations and it has a long lifetime without requiring refreshment of chemical concentration (spiking) into solution bath or heating the solution. It is also important that this approach is non-toxic, eco-friendly, and Cr-free in contrast to other Cr-based counterparts (Sirtl and Seiter) which their reaction byproducts are toxic and have carcinogenic side effects as indicated by the U.S. National Institute for Occupational Safety and Health (NIOSH) [139], hence their utilization is heavily restricted by law.

This chapter discusses the development of a highly specialized chemical solution for high etch rate selective etching of laser-modified surface and subsurface Si regions. The etch recipe is optimized for reasonable etch rate and smooth Si facets. Along with surface quality, sensitivity, reliability, and selectivity were all critical parameters in the development of our etch solution.

3.1 Fabrication steps

In this study, the samples were prepared from double side polished and single-crystalline p-type Si wafers with the orientation of <100>. For the laser processing, two different sets of samples were prepared as follows: for subsurface modifications, the laser was targeted deep inside the Si with a thickness of 525 μm and the resistivity of 1-5 Ω.cm. For surface modifications, the laser beam was mounted to start the process from the deep inside towards the Si top surface. In the latter, the samples with a thickness of 1000 um and resistivity of 1-10 Ω.cm were used. These two sets were aimed to demonstrate an etching profile for both Cross-sectional Accessible Laser Processed (CALP) and Surface Accessible Laser Processed (SALP) with the desired depth.

At the first step, a 1550 nm nanosecond fiber laser was used to perform SALP and CALP modifications in Si. Then, the laser processed Si samples were treated with various etch recipes with varying components adopted from MEMC to extract the best performing composition combination. Figure 3.1 demonstrates our nanosecond laser setup.

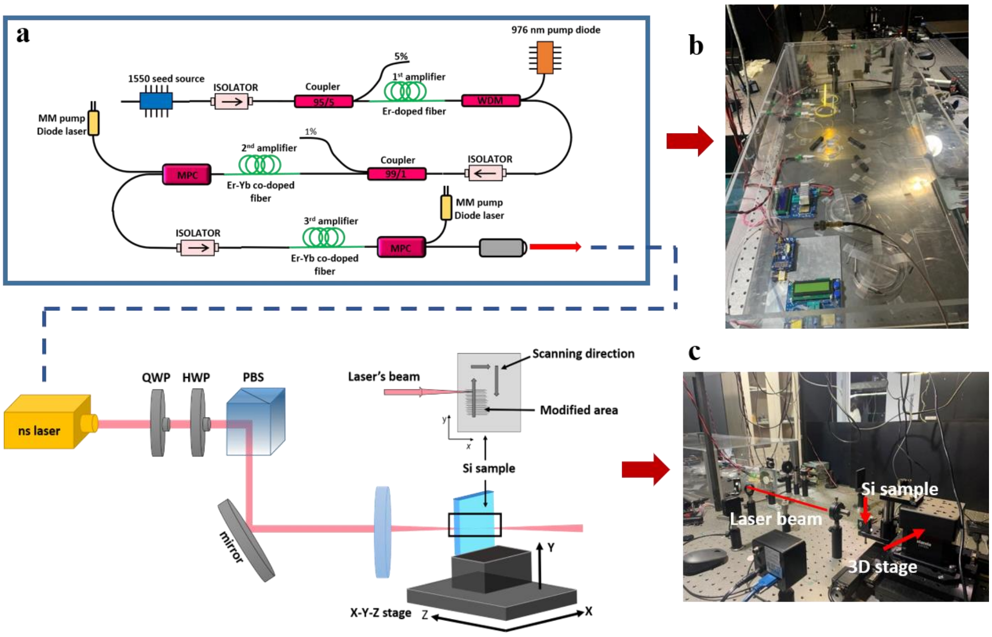

Figure 3.1 Schematic of the experimental set-up (a), Photographs of the set-up (b,c).

3.1.1 Laser-Induced silicon modifications

The laser system used for 3D subsurface processing was an in-house built nanosecond fiber laser, producing up to 5 W of average power at 1550 nm. The repetition rate of the laser was adjustable in the range between 100 kHz to 1 MHz, limited by the generation of amplified spontaneous emission (ASE) at low repetition rate. For subsurface modifications, the repetition rate of the laser was 100 kHz, corresponding to the maximum pulse energy of 50 μJ, and a pulse duration of ~5 ns, however, for surface modifications, much less pulse energy was enough to create the subsurface processed zones. At the given pulse duration and the repetition rate of the laser, we observed stable subsurface modification at pulse energies starting from ~2.5 μJ. The laser beam was focused inside of the samples by an aspheric lens (NA = 0.3, f = 8mm). Although we did not observe any effect of polarization direction on the properties of the processed region, the polarization was vertical. The samples with typical dimensions of 10 mm×10 mm were mounted on a 3D motorized translation stage allowing controllable scanning in all directions with sub-micron resolution. Two different types of the samples were prepared for chemical etching processes. For the first type, the laser was focused into the sample from the cross-sectional direction and the sample was raster scanned in x-y direction as shown in Figure 3.2 (a). Such scanning geometry forms one (or several) laser modified planes inside of the sample parallel to the top surface. The laser-modified thickness of each plane is ~ 4 μm as confirmed from the IR camera images (more details in ref. [34]). Several planes were created on top of each other forming laser processed zone with a thickness of ~ 30 μm as shown in Figure 3.2 (b). For this type of samples, the laser modified zone is accessible for the etchant solutions from cross-sectional surface at three sides with the opening of 30 μm height is presented in Appendix A. We will call this type of the samples as Cross-sectional Accessible Laser Processed (CALP) samples. For the second type of the samples, the laser beam was focused inside of the sample from the top surface and raster scanned in x-y direction as shown in Figure 3.2 (c). The cross-sectional thickness of one plane in z direction is ~ 80 μm. After creation of each plane, the sample was shifted 20 μm down in z-direction (corresponding to ~ 60 µm beam shift- up of the focal point inside of the sample due to refractive index of Si), and the next modified plane was formed with ~ 20 µm overlap with the previous layer. We repeated these steps until the last laser modified plane was created on the top surface of the sample to have total depth of ~ 450 µm, forming the laser modified zone as shown in Figure 3.2 (d). For this type of the samples, the laser modified zone is accessible for the etchant from top surface (10 mm × 10 mm area). We will call this type of samples as Surface Accessible Laser Processed (SALP) samples.

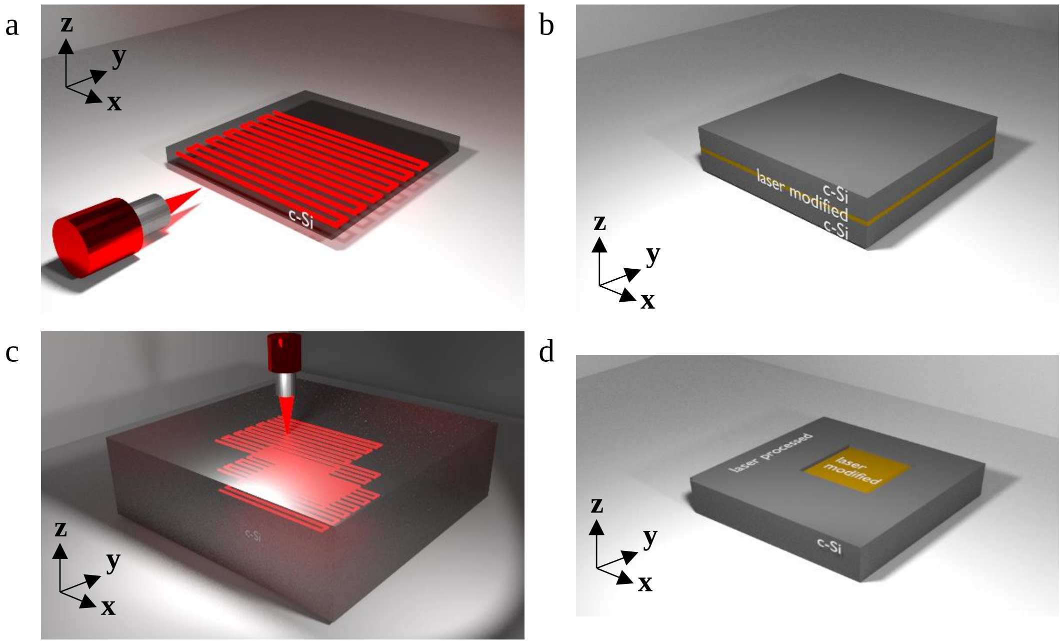

Figure 3.2 (a, c) – Demonstration of laser beam scanning direction inside of the c-Si for CALP sample (a), and for SALP sample (c); (b, d) – Schematic representation of the laser processed zones for CALP sample (b), and for SALP sample (d) (see more explanations in text).

3.1.2 Comparison of different Chemical etchant composition

In the first attempts, the effects of different etching solution compositions were investigated to find the most suitable solution for the subsurface laser modified region which can provide high selectivity at reasonable etch rate of modified regions. Table 3.1 shows the chemical composition of the considered etching solutions. The solution with potassium hydroxide (KOH); as one of the traditional chemicals to etch

Si, was heated to 80 °C prior the etching to activate the reaction. All other etching processes were performed at room temperature.

Table 3.1 Chemical composition of the different etching solutions. The KOH-assisted etching was done at 80°C while other treatments were performed at room temperature. The duration of etching was varied based on the etch speed of the corresponding etching solution.

Solution	HF (39%) ml	HNO_3 (65%) ml	CH_3COOH ml	$Cu(NO_3)_2$ g	$AgNO_3$ g	KOH w/vol %	Duration min
1	-	-	-	-	-	30	10
2	9	68.2	22.8	-	-	-	120
3	40	20	-	-	11	-	10
4	36	25	18	1	-	-	150
5	65	35	-	2	-	-	3

For these experiments, subsurface laser modifications with parallel lines were applied on the Si wafers to identify the effects each etchant on distinct modified regions. The SEM images of etched part of samples are given in Figure 3.3. As it can be seen, the KOH solution (Figure 3.3 (a)) was not effective enough to selectively open the laser modified regions. In addition, the high etch rate difference of KOH solution on the different Si planes leads to the formation of undesired pyramid textures on the surface. On the other hand, the $HF:HNO_3:CH_3COOH$ solution (Figure 3.3 (b)) was successful to reveal and open the laser modified region, however, the etch rate is found to be too low. Solution 3 with $HF:HNO_3:AgNO_3$ (Figure 3.3 (c)) is found to be moderately selective, the etch rate of laser modified regions is modest, and it left many residual particles on the surface. The initial composition of $HF:HNO_3:CH_3COOH:Cu(NO_3)_2$ solution (Figure 3.3 (d)) provided the required etch rate with better selectivity yet the obtained Si surface morphology features several holes which needs to be improved. The $HF:HNO_3:Cu(NO_3)_2$ solution (Figure 3.3 (e)) without acetic acid was too fast which etched large portion of sample in a very short time. In addition, it was not favorable since it could not provide the required selectivity and led to deteriorated surface morphology. SEM images of comparison of different Chemical etchant composition are shown in Figure 3.3.

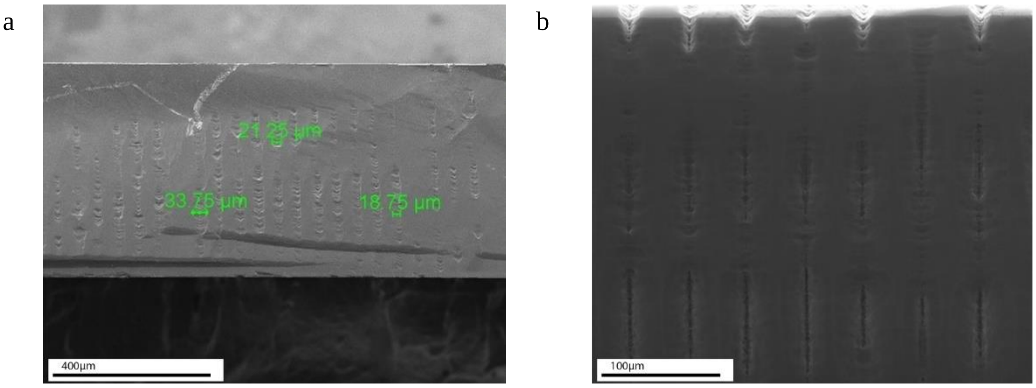

30% KOH

HF(9%):HNO_3(68.2%):CH_3COOH(22.8%)

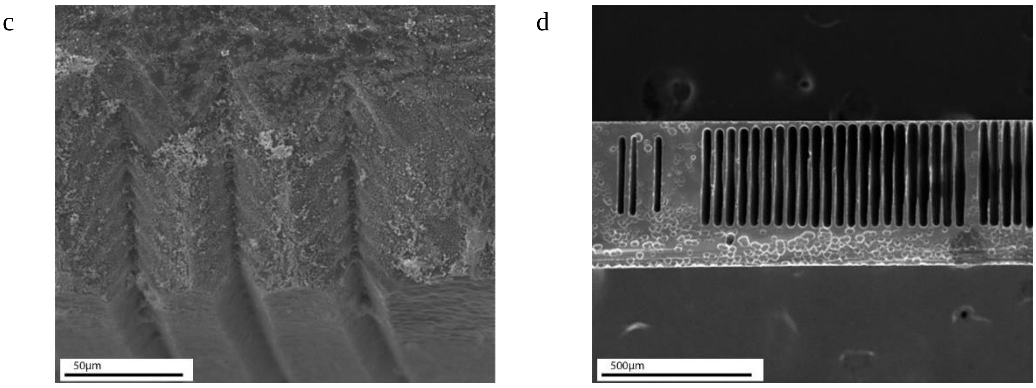

HF(40%):HNO_3(20%):$AgNO_3$(11g)

HF(36%):HNO_3(25%):CH_3COOH(18%):$Cu(NO_3)_2$(1g)

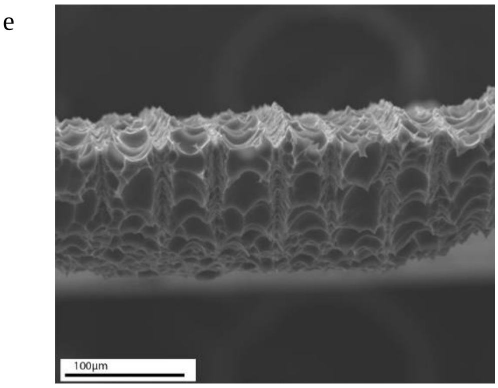

HF(65%):HNO_3(35%):$Cu(NO_3)_2$(2g)

Figure 3.3 SEM images of different etching treatments on the subsurface laser-modified regions. Subfigures (a) to (e) corresponds to solution 1 to 5 in the Table 3.1 respectively.

3.1.3 Silicon sample structures

The effects of different etch solution mixtures are investigated on both CALP and SALP samples. Our motivation is studying selective etching of Si in CALP configuration since it represents a universal scenario in 3D laser structuring of Si. This process does not necessarily create large laser processed surface areas in which the etchant can easily attack. It is especially important to check the feasibility of fabrication of 3D structures embedded inside the Si while heat transfer and diffusion constraints associated with narrow surface openings are present. As a complimentary configuration, we introduced SALP structuring in order to create features from the surface up to desire depth inside Si applications.

For the CALP structuring, the samples were diced into the smaller individual samples with area of 7.3 mm × 2.34 mm after laser modification. The dicing exposes three surfaces of the laser modified region (one 2.34 mm × 0.03 mm and two 6.55 mm × 0.03 mm) to the etchant solution (see Figure 3.2 (b) and Appendix B Fig. 2). For the SALP structuring, samples were diced with dimensions of 10 mm × 10 mm. The laser modified region (2 mm × 2 mm) is exposed to the etchant from one side; vertically from the top surface (see Figure 3.2 (d)). Also, a set of unprocessed Si wafers were diced with identical size (reference samples). Prior to chemical treatments, all samples were subjected to standard cleaning 1 and 2 (SC 1, SC 2) which are used to remove organic contaminants as well as metal and ionic contaminants from the surface of the samples respectively [122].

3.2 Etch rate and selectivity redefined

The well-accepted definitions of etch rate and selectivity in semiconductor micro-processing are univocally valid for surface etch in 2D in literature. As laser processing of crystalline semiconductors is an emerging technique, there appears to be a need for redefinition of both etch rate and selectivity since the etch takes place subsurface in 3D where etch thickness/time is not an applicable measure. So, we have redefined these parameters by using a 3D approach which necessitates using correction factors for the geometry.

In order to calculate the mass reduction due to the etching of the laser modified regions in each chemical mixture [which is referred to as a Set], a pair of laser processed and unprocessed c-Si samples were placed in the same solution as depicted in Figure 3.4. The mass reduction of the laser processed sample consists of two parts: the mass reduction of the laser-modified region and the mass reduction of the remaining (unprocessed) region of the same sample. We estimated the mass reduction of the unprocessed region of the laser modified sample by measuring the mass reduction of the unprocessed sample. Then, by incorporating proper correction factors, we modeled and calculated the mass reduction of the laser modified region (will be detailed in Result and Discussion section). In static etching procedure, there are various unmeasurable parameters involved in the abovementioned calculations. Those parameters include diffusion restriction for the mass and heat transports. Hence, proper estimation of the corresponding correction factors is essential (see Correction Factors Calculation & Etch Pit Radius Distribution Analysis). The SEM images taken from samples at the end of each etching process are used to track and determine the smoothness of the surface morphology by analyzing etch pit size distribution.

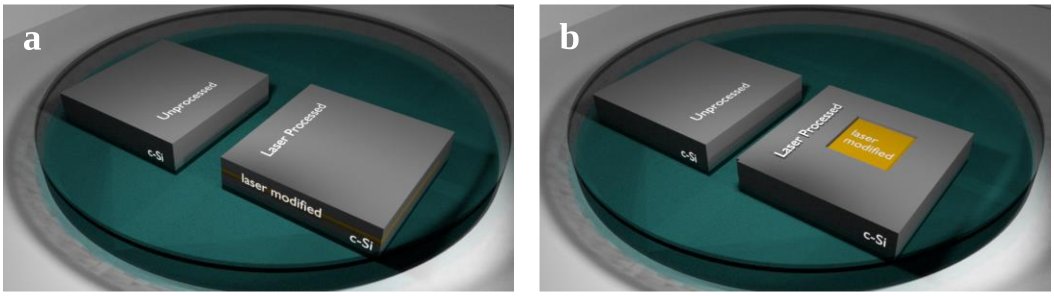

Figure 3.4 Illustration of SALP sample in the chemical bath (a). Illustration of and CALP sample in the chemical bath. In both cases, an unprocessed Si was added (b).

As mentioned in the *Introduction*, MEMC solution is already used in the electronics industry for defect density determination of Si wafers. However, the MEMC solution offers a high etch rate at the expense of high selectivity and smooth surface morphology. In order to lend MEMC the preferred qualities in selectivity and surface morphology, we made a systematic analysis of the function of redox mechanism [82,140] on etching chemistry. In order to investigate the effects of the nitric acid (HNO_3) as an oxidant, copper (II) nitrate hydrate salt ($Cu(NO_3)_2.3H_2O$) as a catalyst [120,138], and hydrofluoric acid (HF) as a oxide dissolvent on selectivity, etch rate, and surface morphology, the concentration of each component was varied in a systematic fashion. A total of 12 different sets of solutions were considered. The concentrations of the components are separated into three subgroups which are highlighted in Table 3.2. Within each subgroup, only one component of the mixture is varied. The amount of DI water is also varied to keep the solution volume fixed to 100 ml.

In order to calculate the etch rates, mass reductions of the laser processed sample and the unprocessed sample were measured by weighting the samples after etching in each solution for 60 minutes with 10-minute intervals for CALP and 5-minute intervals for SALP. We specifically probed the interval between 10 to 60 minutes of etch durations since industrial applications favor short etch durations while too short durations may not be sufficient to fully etch modified regions. Based on the obtained etch rates, we calculate the selectivity (the ratio of etch rates for the laser modified and unprocessed regions) of each solution set, and hence, assess the effects of each component to determine the corresponding properties of the solution.

Table 3.2 Chemical composition of solutions by variation of $Cu(NO_3)_2$ concentration, HF concentration, and HNO_3 concentration. The amount of H_2O is adjusted to obtain 100 ml of solution (which corresponds to 100%).

	$Cu(NO_3)_2$ (g)	HF (ml) or (vol%)	HNO_3 (ml) or (vol%)	CH_3COOH (ml) or (vol%)	H_2O (ml) or (vol%)
$Cu(NO_3)_2$ Comparison	**0.75**	14	16.25	18	51.75
	1.25				
	1				
	2				
HF Comparison	1	**7**	16.25	18	Remaining to 100 %
		10			
		12			
		14			
		16			
		18			
HNO_3 Comparison	1	14	**9.75**	18	Remaining to 100 %
			13		
			16.25		
			19.5		
			22.75		

Correction factors calculation & etch pit radius distribution analysis

To calculate the etch rate and selectivity in terms of reduced mass of the samples, the mass of laser processed silicon and the etched part of it must be determined. Thus, to find the mass change of the unmodified region, another unprocessed sample was used. The subtraction of the mass changes of the laser processed sample and the unprocessed sample is related to the laser modified region. After each chemical process, the mass change of the unprocessed and processed samples was measured.

The difference between the measured masses gives the etched mass of the laser modified region, which needs to be corrected due to the complicated behavior of the etching process, coming from diffusion peculiarities of the mass and heat transports. Therefore, the mismatch of the initial masses before the chemical etching of unprocessed and laser processed samples, the volume etched inside the laser modified region (see explanation below), and different in the opening areas of crystalline region and laser modified region of the processed sample being subjected to etchant needs to be modeled accordingly. To calculate laser modified mass properly in CALP structures, we hypothesis three correction factors, namely, Correction Factor of Initial Mass (CFIM), Correction Factor of Etch Opening (CFEO), and Correction Factor of Attacked Area (CFAA).

We tend to match the shape and size of laser processed and unprocessed samples. Thus, we used the following CFIM to compensate the small discrepancies in the masses of the processed and unprocessed samples, defined as:

$$CFIM = \frac{Initial\ Mass\ of\ Unprocessed\ Sample}{Initial\ Mass\ of\ Laser\ Processed\ Sample} \qquad \text{Eq 3.1}$$

Next, CFEO was determined by analyzing the opening of the etched part from the SEM images (a representative opening for *the champion etchant* with composition of $HF:HNO_3:CH_3COOH:H_2O$ – 56:65:72:207 with 0.01 g/ml $Cu(NO_3)_2.3H_2O$ is shown in Figure 3.5).

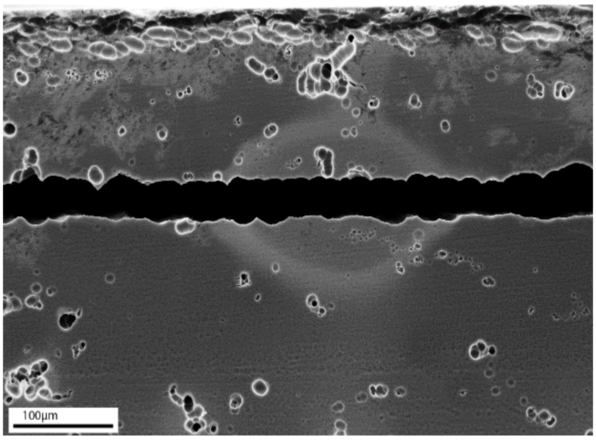

Figure 3.5 Cross-sectional SEM image after 60 min etching showing the opening and etch pits resulted from the etching process for the champion etchant.

This correction factor is essential for the samples where the openings after chemical etching are larger than the laser modified initial thickness (30 µm). In this case, all laser-modified regions are etched until a certain depth, exposing some parts of unprocessed regions above and below the laser modified region to the etchant. We assume that the etching of unprocessed regions is relatively proportional to the etching of unprocessed sample which experience exactly the same solution. On the other hand, for the samples with openings being less than the laser modified thickness, this correction factor is not used. To simplify the analysis, we assume that the geometrical factor is linear. The formulation of CFEO is given in Eq 3.2.

$$CFEO = \frac{Corresponding\ Opening\ Thickness\ -\ 30\ \mu m}{Thickness\ Reduction\ of\ Unprocessed\ Sample} \qquad \text{Eq 3.2}$$

In the following, the details of calculations of “Corresponding Opening Thickness” and “Thickness Reduction of Unprocessed Sample” are presented. The proportionality of etched part of unprocessed Si regions of laser processed sample to unprocessed sample is their relative difference in thickness. Since the openings are distinct straight lines, the “Area of Opening of Laser Processed Region of Laser Processed Sample” is calculated using Gwyddion [141] which is colored red in Figure 3.6. Then, this area is divided by the “Length of Opening at Given Magnification” which leads to “Corresponding Opening Thickness” as described in Eq 3.3. As an example, the opening of laser processed region for *the champion etchant* is shown in Figure 3.6. In this figure, magnification is 500x which indicates that “Length of Opening at Given Magnification” is 596 µm.

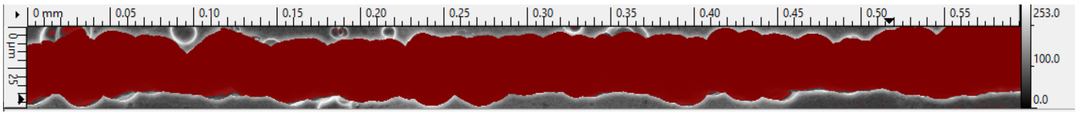

Figure 3.6 Area of the opening after etching treatment at the specific magnification (Set Opt: 500x).

$$Corresponding\ Opening\ Thickness = \frac{Area\ of\ Opening\ of\ Processed\ Region\ of\ Laser\ Processed\ Sample}{Length\ of\ Opening\ at\ Given\ Magnification} \qquad \text{Eq 3.3}$$

Based on the fact that the subsurface laser modified region thickness is 30 µm, the thickness of unprocessed region is “Corresponding Opening Thickness” minus 30µm.

The “Thickness Reduction of Unprocessed Sample” is calculated based on the “Exact Unprocessed Thickness” which can be obtained from initial mass converted to volume using density as stated in Eq 3.4.

$$\begin{aligned} &\mathit{Exact\ Unprocessed\ Thickness} \\ &\quad = \frac{\mathit{Initial\ Mass\ of\ Laser\ Processed\ Sample}}{\mathit{Silicon\ Density}} \\ &\quad \times \frac{1}{\mathit{Diced\ Area}\ (2.34mm\ \times 7.3mm)} \end{aligned} \qquad \text{Eq 3.4}$$

In order to calculate “Thickness Reduction of Unprocessed Sample”, “Final Volume” given Eq 3.5 is required. “Thickness Reduction of Unprocessed Sample” can be obtained by considering the thickness reduction from all 3 dimensions as presented in Eq 3.6.

$$\mathit{Final\ Volume} = \frac{\mathit{Final\ Mass\ of\ Laser\ Processed\ Sample}}{\mathit{Silicon\ Density}} \qquad \text{Eq 3.5}$$

$$\begin{aligned} &\mathit{Thickness\ Reduction\ of\ Unprocessed\ Sample} \\ &\quad = SOLVE\ \{(7.3 - x)(2.34 \\ &\quad - x)(\mathit{Exact\ Laser\ Processed\ Thickness} - x) - \mathit{Final\ Volume}\} \end{aligned} \qquad \text{Eq 3.6}$$

The mass reduction from unprocessed samples only occurs on the outer surfaces, being the c-Si lattice. However, in the case of laser-modified samples, etching occurs on both the outer surfaces as well as in the inner laser-modified region. It is worth mentioning that the volume neighboring the laser-modified region gets damaged during laser processing. The mass reduction of the outer layer of both laser processed and unprocessed samples are just identical. Thus, by applying CFIM and CFEO for each set, the laser modified mass can be calculated as:

$$\begin{aligned} &\mathit{Laser\ Modified\ Mass} \\ &\quad = \mathit{Mass\ Reduction\ of\ Laser\ Processed\ Sample} \\ &\quad - \frac{\mathit{Mass\ Reduction\ of\ Unprocessed\ Sample}}{\mathit{CFIM}} \\ &\quad - \mathit{Mass\ Reduction\ of\ Unprocessed\ Sample} \times \mathit{CFEO} \end{aligned} \qquad \text{Eq 3.7}$$

Later, for better comparison between the laser modified region of processed sample and the unprocessed sample, we consider the percentage of total mass by dividing each mass change by its own total mass:

$$\%\ \mathit{Mass\ Change} = \frac{\mathit{Mass\ Change}}{\mathit{Total\ Mass}} \qquad \text{Eq 3.8}$$

Where the “Total Mass” of the laser modified region is calculated based on the laser modified volume, being 6.55×2.34×0.03 mm^3 and the Si density being 2.329 $\mathrm{mg/mm}^3$.

After obtaining the %Mass Change of laser modified region over time, we calculate the etch rates. For the *champion etchant*, the etch mass is shown in Figure 3.7. for both unprocessed sample and laser-modified region of the processed samples.

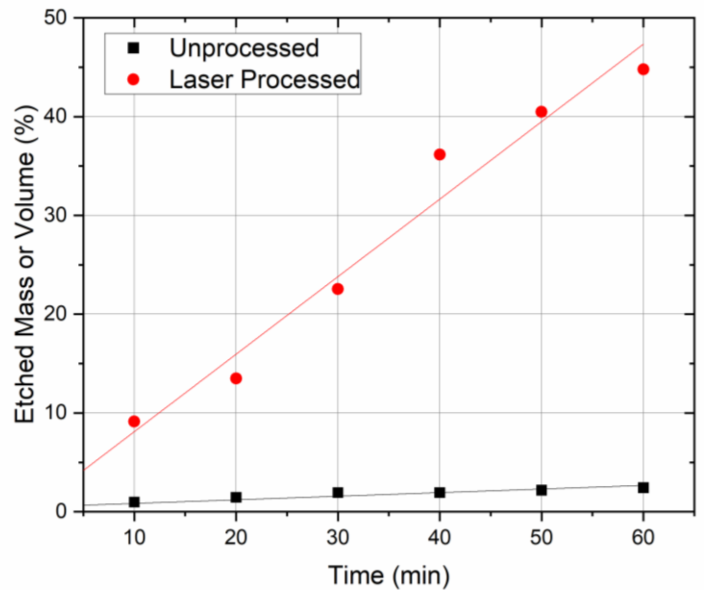

Figure 3.7 The etch rates of laser modified region (red) and unprocessed sample over time, including the linear trend line of each etch rate for the champion etchant.

The huge difference between the masses of the unprocessed sample and the laser modified regions; of the laser processed sample, is due to the exposed area of the sample and regions to the etchant. The unprocessed sample is exposed to the etchant from all surfaces (7.4×2.34×0.525 mm^3), whereas the laser-modified region is subjected to etchant from only 3 surfaces, as illustrated in yellow in Figure 3.2 (b).

Since the laser-modified region of the laser processed sample and unprocessed sample are attacked from different surfaces with different areas, the selectivity needs to be corrected by this area factor. The CFAA is defined as the "Attacked Area of Unprocessed Sample" over the "Attacked Area of Laser Modified Region" (a constant here; Eq 3.9).

$$CFAA = \frac{Attacked\ Area\ of\ Unpcessed\ Sample}{Attacked\ Area\ of\ Laser\ Modified\ Region} = \frac{2(a*b+a*c+b*c)}{2(a'*c')+b'*c'} = 95.609 \quad \text{Eq 3.9}$$

where,

a = 7.4, b = 2.34, c = 0.525 and a' = 6.55, b' = 2.34, c' = 0.03

To calculate the selectivity, first, we regress the mass reduction of the laser-modified region and unprocessed sample to obtain the corresponding average etch rates. Next, the selectivity was defined as the etch rate of laser modified region divided by etch rate of unprocessed sample, in each set using:

$$Selectivity = \frac{Etch\ Rate\ of\ Laser\ Modified\ Region}{Etch\ Rate\ of\ Unprocessed\ Sample} \times CFAA \quad \text{Eq 3.10}$$

The etch pit size distribution is determined using the built-in image processing toolbox of MATLAB [142] and the SEM images of subsurface processed Si. It is worth mentioning that the subsurface and surface processing have identical surface morphology. The histogram of etch pit size distribution for each material is presented in *Effects of Solution Components*. The SEM image of the *champion etchant* is shown in Figure 3.8.

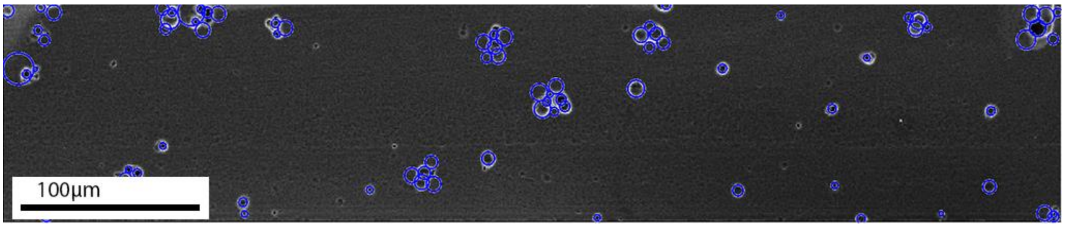

Figure 3.8 The selected area for the champion etchant from cross-sectional SEM image and the result etch pit size distribution analysis.

To compare the SALP and CALP etching behaviors, the calculated mass reduction of laser processed region are normalized to the opening areas that are exposed to the etching solution (0.46 mm^2 and 4 mm^2 for CALP and SALP respectively). The comparisons are presented in the Figure 3.14 (c), Figure 3.15 (c), and Figure 3.16 (c), for variations of $Cu(NO_3)_2$, HF, HNO_3 respectively.

For the SALP processing, after obtaining the %Mass Change of laser modified region over time, we calculate the etch rates. An example for the *champion etchant* is shown in Figure 3.9 for both unprocessed sample and laser modified region.

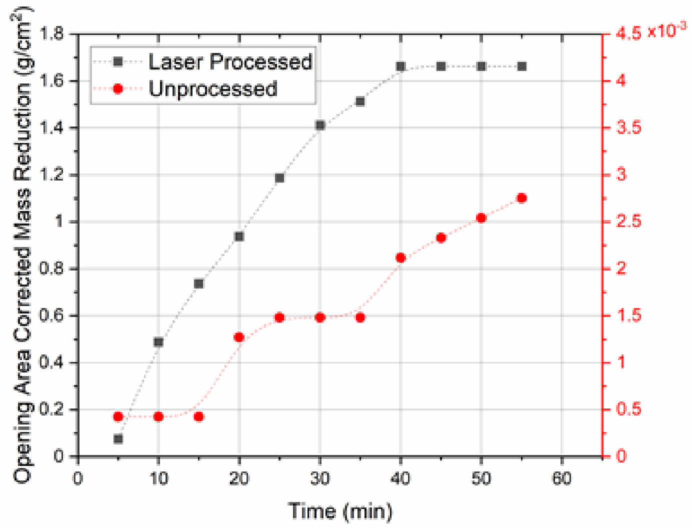

Figure 3.9 Etched masses of laser modified region and unprocessed sample corrected by exposed area for the champion etchant.

For the SALP structuring, the opening area of the laser modified region (2×2=4 mm^2) is 9 times larger than that of CALP (6.55×0.03+6.55×0.03+2.34×0.03=0.46 mm^2). The huge difference between the masses of the unprocessed sample and the laser modified regions is due to the exposed area of the sample and regions to the etchant. The unprocessed sample is exposed to the etchant from all surfaces (10×10×1 mm^3). In contrast, the laser modified region is subjected to etchant from the top on SALP, as illustrated in yellow in Figure 3.2 (d).

Since in the SALP structuring, we eliminated the limitation of diffusion in the etching region, the mass change of laser modified region can be directly calculated by subtracting the etched mass of the laser modified sample from unprocessed sample which is normalized by total mass reduction of laser processed sample (Eq 3.11); to include the total change of laser processed sample as shown in Figure 3.4 (b). The derivative of laser modified mass change is also calculated and presented for every chemical composition in Appendix D Fig 5 and Fig 6.

$$\begin{aligned} &Laser\ Modified\ Mass\ Change \\ &= \frac{Mass\ Reduction\ of\ Laser\ Processed\ Sample - Mass\ Reduction\ of\ Unprocessed\ Sample}{Total\ Mass\ reduction\ of\ laser\ Processed\ Sample} \end{aligned} \qquad \text{Eq 3.11}$$

The ratio of laser modified region to unprocessed sample is presented by Eq 3.12, indicating that what portion of reduction is related to which region at each time.

$$\begin{aligned} &Ratio\ of\ Laser\ Modified\ Mass\ to\ Unmodified \\ &= \frac{Mass\ Reduction\ of\ Laser\ modified\ Region}{Mass\ reduction\ of\ Unprocessed\ Sample} \end{aligned} \qquad \text{Eq 3.12}$$

3.3 Results and discussions

To determine the effectiveness of each etching set, we have calculated the etch rate, etch pit radius distribution analysis, and selectivity of laser-modified structures for both CALP and SALP as well as the derivative of normalized etched mass and ratio of area normalized etched mass of the surface are calculated for SALP. The etch rate is defined as the mass reduction of the laser modified region versus etching duration. The selectivity is defined as the etch rate of the laser modified region divided by the etch rate of the unmodified region, indicating the rate at which the laser modified region is etched away compared to the unmodified region. Note that it is also possible to use the sample volume instead of the mass since they only differ in a density factor which is the same for both the laser modified region and unprocessed samples. The etch pit radius distribution analysis which is an indication of the surface porosity and roughness, is performed for different concentrations of the solution components. The SEM images (Figure 3.10, Figure 3.11, and Figure 3.12) show that the etched surfaces of laser modified samples contain distinctive features such as etch pits in all considered sets. The observable etch pits on the surface are formed due to the interaction of the different solutions with the c-Si segments. Our etchant solution is formulated to selectively reveal the defects and thus the laser modified regions. The etchant attacks and magnifies the defect including dopant impurities on the surface of the Si rather than attacking the perfect (unprocessed) Si lattice. By utilizing chemical etching and etch pit analysis, it is possible to calculate the defect density (counting the etch pits and dividing them by the surface area) that is grown in the crystal lattice. However, it is a destructive characterization technique for the determination of crystal quality of crystalline samples.

3.3.1 Comparison of MEMC and the Developed Champion Etchant

We adopted the MEMC chemical compositions and its initial concentrations since $Cu(NO_3)_2$ is very defect sensitive which is effective not only on c-Si but also on laser modified Si regions. Even though it is orientation and dopant type dependent, it can be used for both dopant types since it has reasonable etching durations for different purposes and long lifetime without spiking in solution. It also does not require excessive heating and not forming dangerous gasses in solution. Additionally, unlike other etching solutions that contain Cr (VI) as an oxidizing agent such as Sirtl, Seiter, Wright, and Secco, MEMC etching is Cr-free. However, conventional MEMC solution was too fast and had relatively low selectivity. Thus, we modified and optimized the MEMC solution to obtain the optimum solution (*the Champion Etchant*). In *the Champion Etchant*, the etch rate is lower which provides required time for chemical treatments depending on the desired application. It is also more dopant type dependent and more anisotropic. After considering different concentrations of each component in the solution, the optimum concentration is achieved (14 (HF):16.25 (HNO_3):18 (CH_3COOH):51.75 DI water with 1g $Cu(NO_3)_2.3H_2O$).

The comparisons between MEMC and *the Champion Etchant* in terms of orientation and dopant type dependencies are presented in Table 3.3 and Table 3.4.

Table 3.3 Effect of MEMC etching solution on the <111> and <100> plane and p-type and n-type wafers with duration of 12min.

	Type	Plane	Thickness µm	Initial Mass mg	Final Mass mg	Mass Reduction mg	Normalized Mass Reduction %
1	p-type	<111>	525±25	274.55	139.95	134.60	49.03
2	p-type	<100>	279±15	150.85	044.65	106.20	70.40
3	n-type	<100>	279±15	144.05	092.65	051.40	35.68

Table 3.4 Effect of *the Champion Etchant* etching solution on the <111> and <100> plane and p-type and n-type wafers with duration of 18min.

	Type	Plane	Thickness µm	Initial Mass mg	Final Mass mg	Mass Reduction mg	Normalized Mass Reduction %
1	p-type	<111>	525±25	275.95	275.10	000.85	0.31
2	p-type	<100>	279±15	149.65	148.50	001.15	0.77
3	n-type	<100>	279±15	144.20	142.50	001.70	1.18

According to Table 3.3 and Table 3.4, it can be recognized *the Champion Etchant* etches p-type 1.48 times slower than n-type while MEMC etches p-type 2.07 times faster than n-type. In addition, <100> plane etch rate is higher than <111> for both MEMC and *the Champion Etchant*.

3.3.2 Effects of solution components on etchant chemistry

Etch rate (etched mass over time) and selectivity of the CALP structure, normalized etched mass and ratio of area normalized etched mass of the SALP structure, and etch pit radius distribution analysis for all chemical compositions were calculated based on the equations mentioned in section 3.2. This information is categorized into three subgroups for each solution component. The etch rate for CALP and normalized etched mass for SALP structure is not constant across time since there is some latency before the etching starts. Thus, some delay may be required for the activation of Si-etchant reactions. Afterward, chemicals start to attack all regions until either the reactions reach saturation, or the time frame is over. The etch rate and normalized etched mass over time and parameter concentration are given in Figure 3.14 (a, d). The selectivity of CALP and ratio of area normalized etched mass of the SALP samples are plotted in Figure 3.14 (b, e). Comparison of mass changes between CALP and SALP are shown in Figure 3.14 (c) indicating the effect of subsurface and surface etching. The etch pit radius size distribution presented in Figure 3.14 (f) shows the smoothness of surface morphology.

3.3.2.1 SEM / infrared (IR) camera images

The SEM images of all sets categorized into 3 subsets representing variation of each etching component are presented in Figure 3.10, Figure 3.11 and Figure 3.12 respectively showing variation of $Cu(NO_3)_2$, HF, and HNO_3.

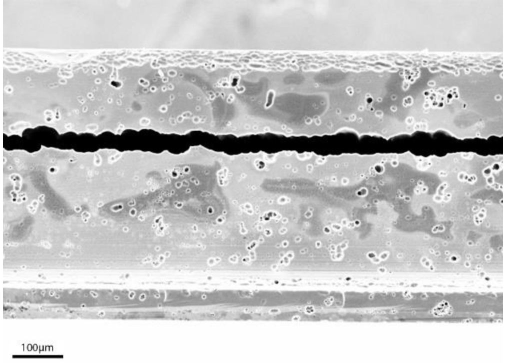

$Cu(NO_3)_2$ 0.75g

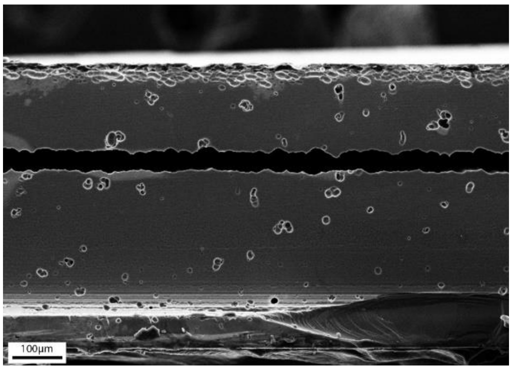

$Cu(NO_3)_2$ 1g

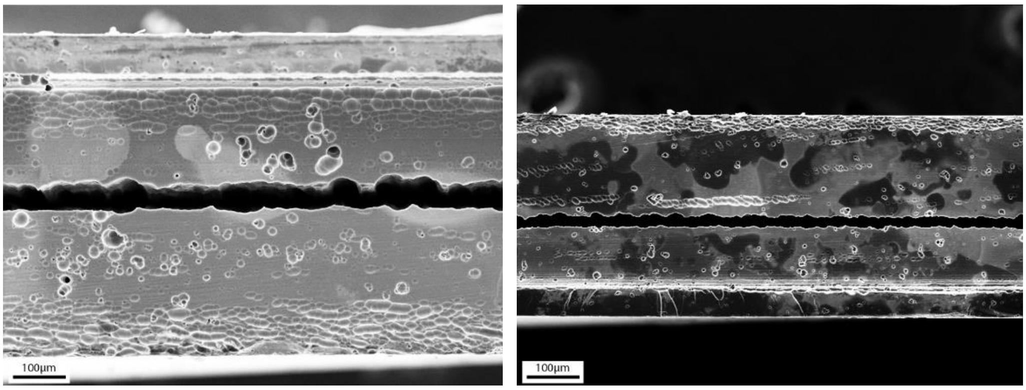

$Cu(NO_3)_2$ 1.25g $Cu(NO_3)_2$ 2g

Figure 3.10 SEM images of laser modified openings after etching in the developed solution with different $Cu(NO_3)_2$ concentration: 0.75g to 2g in 100ml of etching solution.

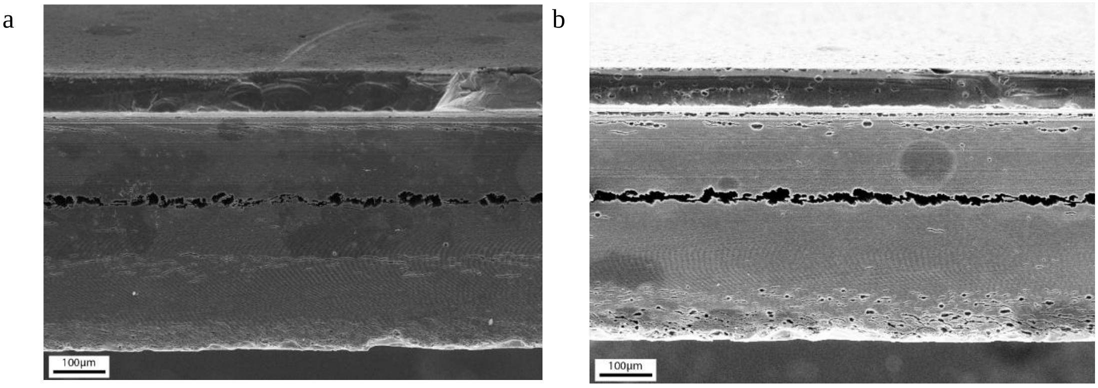

HF 7ml HF 10ml

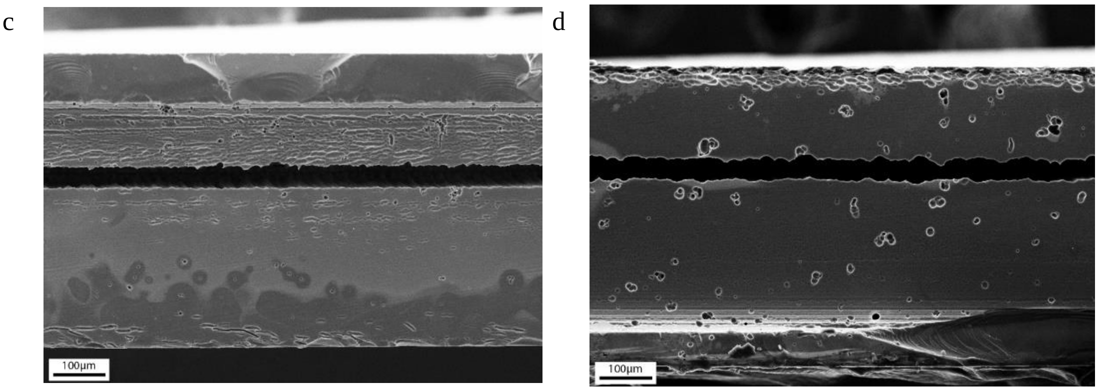

HF 12ml HF 14ml

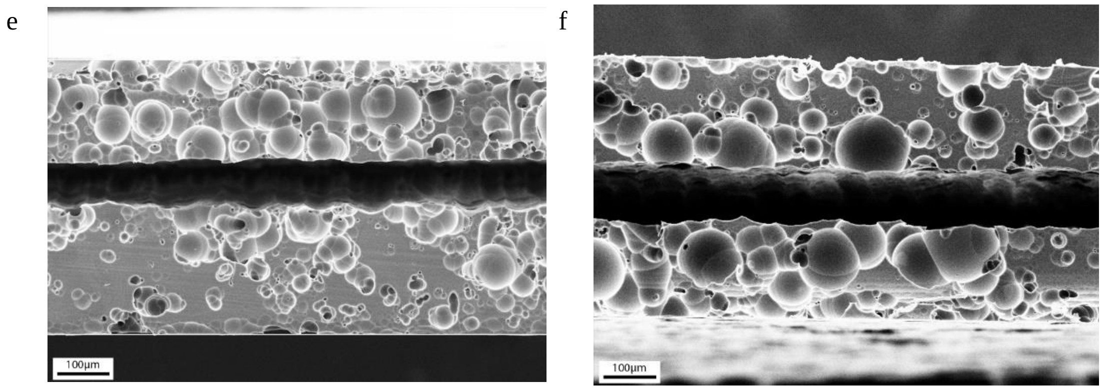

HF 16ml HF 18ml

Figure 3.11 SEM images of variation of HF concentration from 7ml to 18ml in 100ml of etching solution.

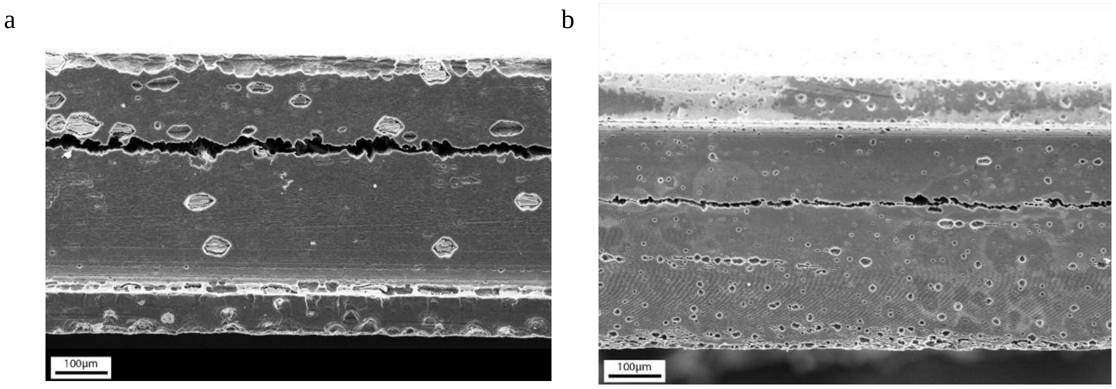

HNO_3 9.75ml HNO_3 13ml

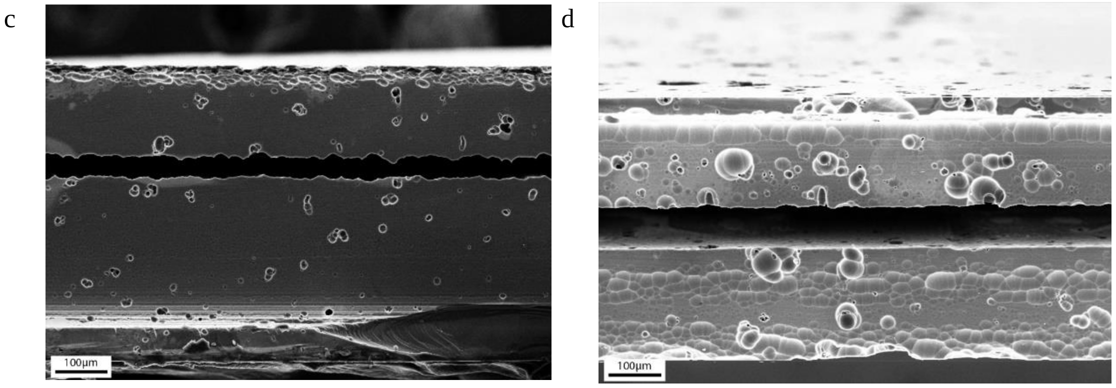

HNO_3 16.25ml HNO_3 19.5ml

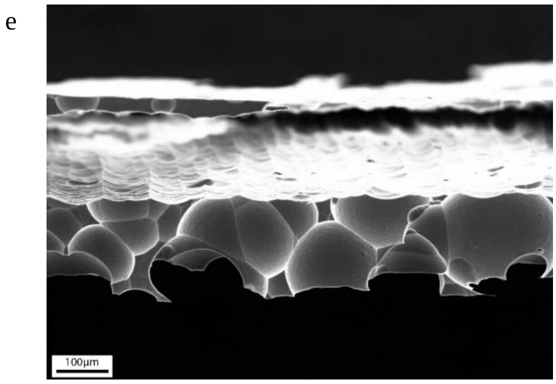

HNO$_3$ 22.75ml

Figure 3.12 SEM images of variation of HNO$_3$ concentration from 9.75ml to 22.75ml in 100ml of etching solution.

IR camera images

We measured the etched area of the laser modified region from the images obtained by the infrared (IR) camera. Figure 3.13 (a) clearly shows the laser modified and etched regions. The IR image of *the Champion Etchant* after 60 min etching is shown in Figure 3.13 (b). In this image, the black color is the etched modified region. In addition, the grey color at the center is laser modified region while the grey color at top of image is unmodified region. The two grey regions look similar since the modifications in crystallinity is not profound to be visible in IR camera region. The opening is obtained using SEM image in Figure 3.6. The other sets are presented in Appendix C Fig. 3.

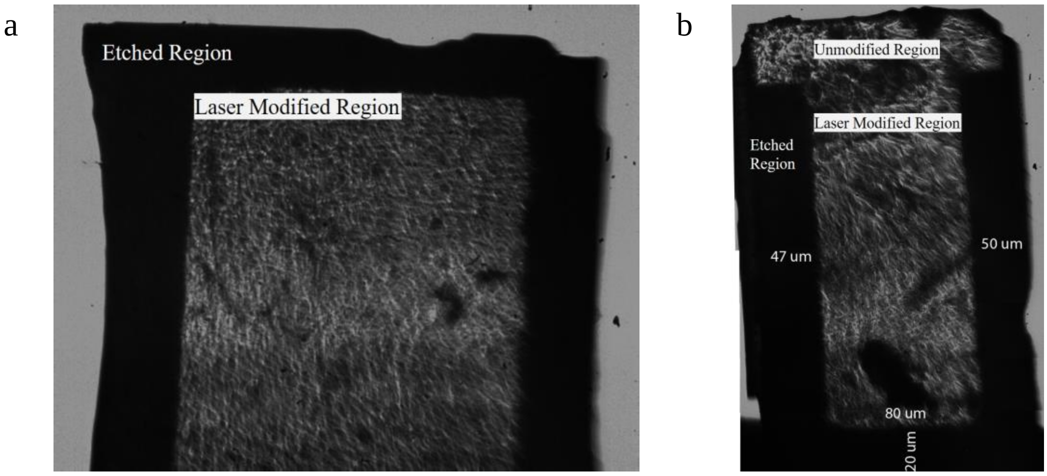

Figure 3.13 Image of infrared camera of the etched laser modified region.

3.3.2.2 Effects of Copper Nitrate – $Cu(NO_3)_2$ Variation

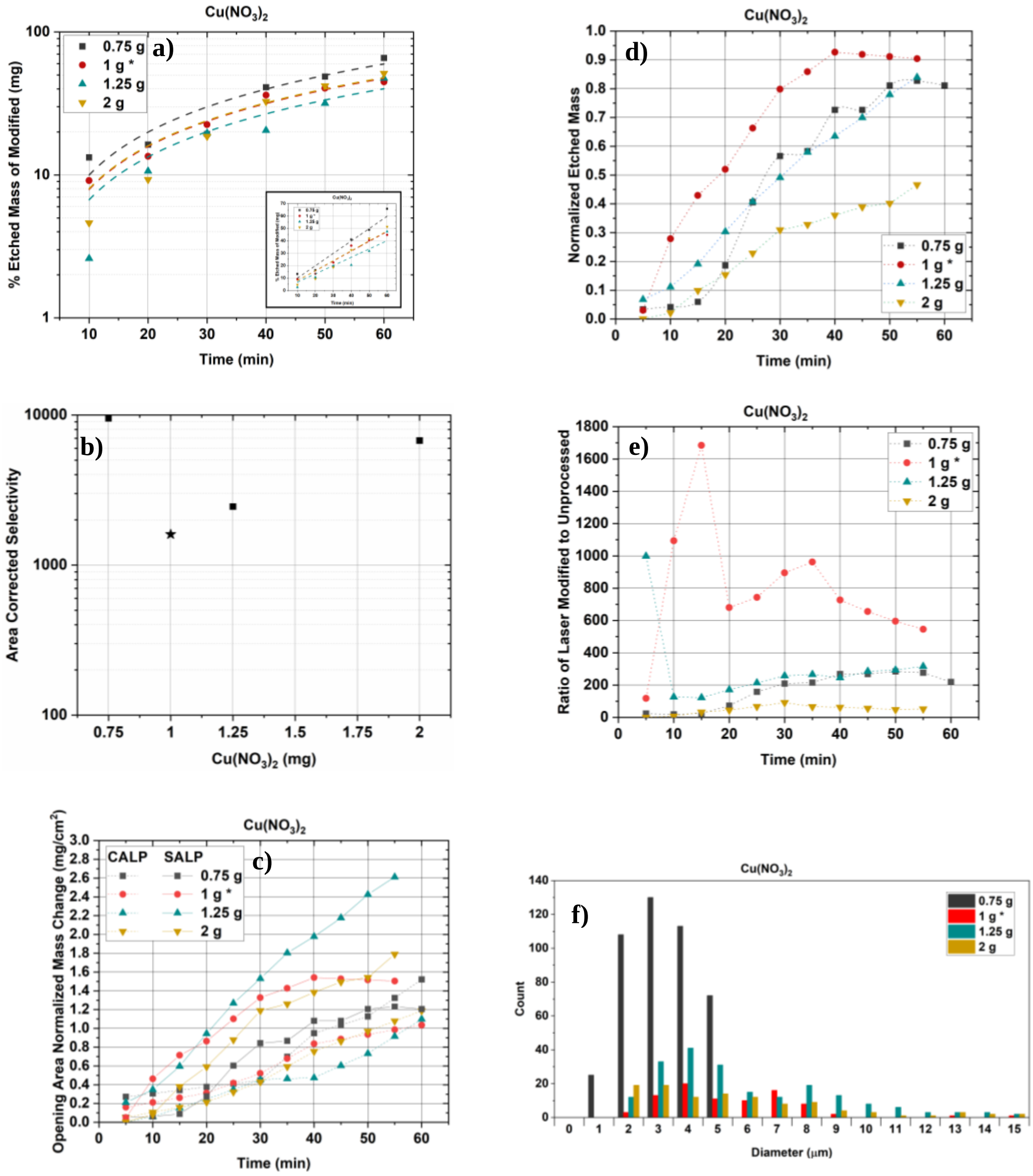

Figure 3.14 Etch rate of laser modified region over time by changing the $Cu(NO_3)_2$ concentrations from 0.75 to 2 g in 100 ml of solution for CALP (a); The selectivity of laser modified region comparing to unprocessed sample by fitting the etch rates over time for CALP (b); The area corrected etched mass of laser modified region for SALP (solid line) and CALP (dashed line) for different concentrations over 60 minutes (c); Normalized etched mass of laser modified region for SALP (d); The ratio of area normalized etched mass of laser modified region over the unprocessed region for SALP (e); Etch pit radius distribution obtained from SEM images by analyzing the surface morphology (f).

The energy level of the Cu^{2+}/Cu system is higher than the valence band (VB) of the Si. For a given combination of HF/HNO_3, adding various amounts of $Cu(NO_3)_2$ corresponds to the Si surface being covered by copper nanoparticles (CuNPs) of different sizes. These metal particles also catalyzed the etching of Si in HF/HNO_3 solution and were resulted in selectively attacks modified regions. The Cu^{2+} ions are reduced to solid Cu on the Si substrate and the oxidized surface is dissolved in HF. In addition, HNO_3 oxidizes the Si surface forming SiO_2 which is etched by the presence of HF.

In Figure 3.14 (a), it can be seen that the etch rate of the laser modified region decreases as the amount of $Cu(NO_3)_2$ increases from 0.75 to 1.25 g. However, the etch rate starts to increase for a lower amount of $Cu(NO_3)_2$.

In addition, as shown in Figure 3.14 (b), the selectivity for CALP shows a different trend where it is highest for 0.75 g of $Cu(NO_3)_2$ and drops drastically then increases by increasing the $Cu(NO_3)_2$ amount. In Figure 3.14 (c), the etched masses are normalized to their opening area due to the difference in an opening area exposed to etchant solution. The laser-modified etched mass in SALP exhibits higher trend compared to that of the subsurface laser processing. In Figure 3.14 (d), the etched mass of laser modified region divided by total etched mass is highest where the $Cu(NO_3)_2$ amount is 1 g. However, the etched mass decreases as the amount of $Cu(NO_3)_2$ increases from 0.75 to 2 g. In Figure 3.14 (e), the ratio of laser modified to unprocessed samples decreases as etching time increases. For longer durations, etchant starts etching unmodified parts when all the modified masses are etched away; thus, the ratio begins to increase again, and the selectivity will therefore decrease.

The etch pit radius distribution, ranging between 1 – 15 µm, is identical for both SALP and CALP surface as shown in Figure 3.14 (f) which infer that the etching solution results in similar surface morphology regardless the place of the laser modifications. The etch pit size distribution is in the order of 10^0. However, as the amount of $Cu(NO_3)_2$ increases, the resultant defects are found to have larger diameters this can be attributed to the increase in the oxidation rate of Si surface which increase the probability of revealing the defects embedded in the c-Si.

3.3.2.3 Effects of Hydrofluoric Acid – HF variation

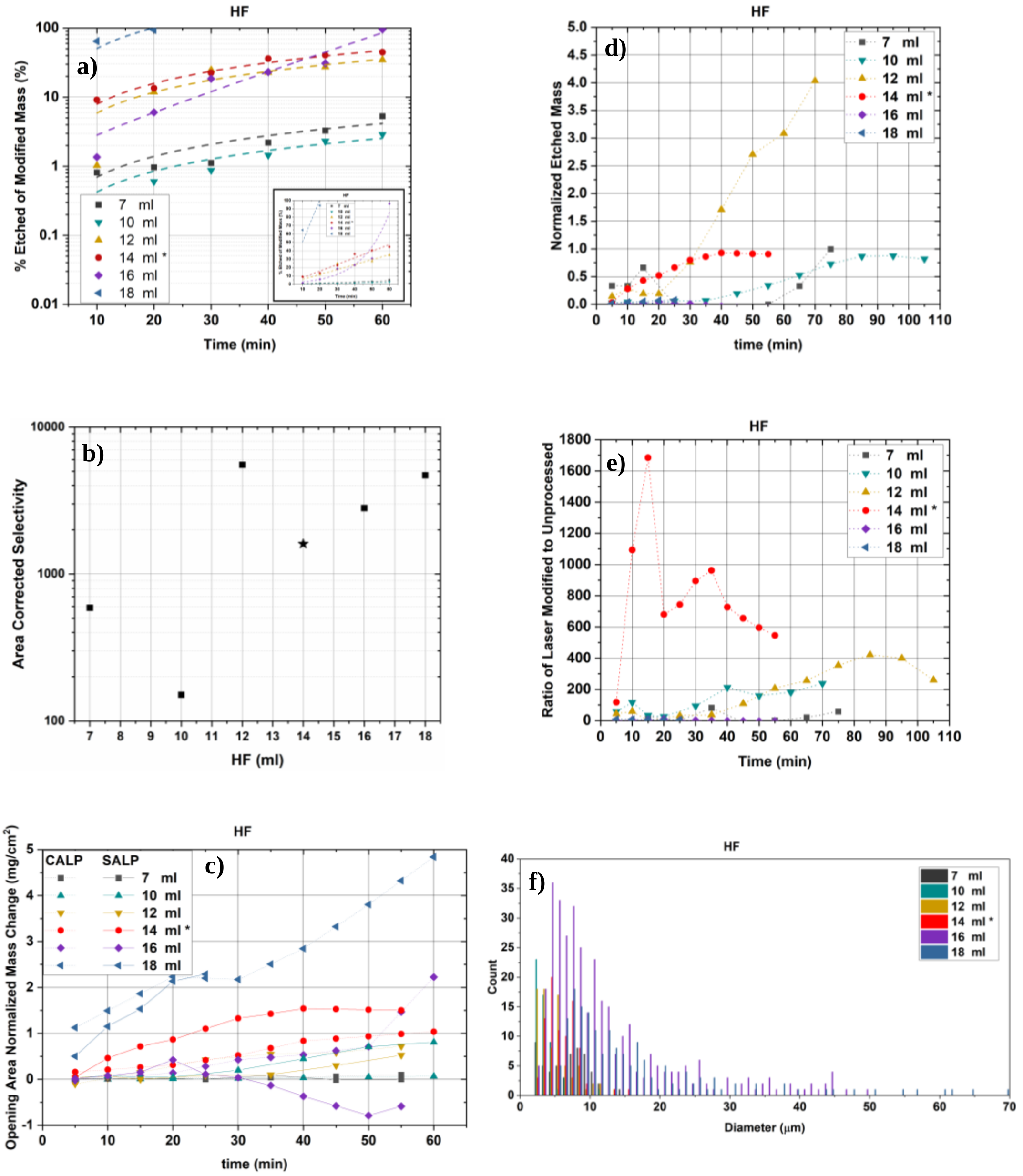

Figure 3.15 Etch rate of laser modified region over time by changing the HF concentrations from 7 ml to 18 ml in 100 ml of solution for CALP (a); The selectivity of laser modified region comparing to unprocessed sample by fitting the etch rates over time for CALP (b); The area corrected etched mass of laser modified region for

SALP (solid line) and CALP (dashed line) for different concentrations over 60 minutes (c); Normalized etched mass of laser modified region for SALP (d); The ratio of area normalized etched mass of laser modified region over the unprocessed region for SALP (e); Etch pit radius distribution obtained from SEM images by analyzing the surface morphology (f).

Increasing the amount of HF beyond a certain point for a given ratio of the copper and HNO_3 hinders the suspension of the NPs. Thus, NPs will be adsorbed on the surface at random locations and give rise to promotion of the etching process in their vicinity. This process is fast and creates more holes on the surface leading to a spongy Si surface morphology.

As can be seen in Figure 3.15 (a), a higher concentration of HF in the solution has very high etch rate, and it damages the sample leading to poor surface morphology (Figure 3.11(e, f)). The effect of higher HF is more pronounced in laser-modified regions than the unprocessed sample, resulting in higher selectivity (Figure 3.15 (b)). In Figure 3.15 (c), the laser modified etched mass in SALP goes higher than subsurface except for the solution with higher HF concentrations. In Figure 3.15 (d), the etched mass of laser modified divided by total etched mass region is well behaved for 14 ml of HF showing a reasonable etch rate. However, the modified region is harshly attacked in the etching solution with high HF concentration which can be due to the non-linear diffusion nature of the defects. In Figure 3.15 (e), the ratio of laser modified region to unprocessed sample decreases as time increases for the lower HF concentration. In Figure 3.15 (f), the etch pit size distribution is below15 µm when the HF concentrations is moderate (7 ml to 14 ml). With higher concentration of HF (above 16ml), the etch pits exhibits larger defect sizes on the Si surfaces as can be seen in SEM image (Figure 3.11(e, f)).

3.3.2.4 Effect of Nitric Acid – HNO_3 variation

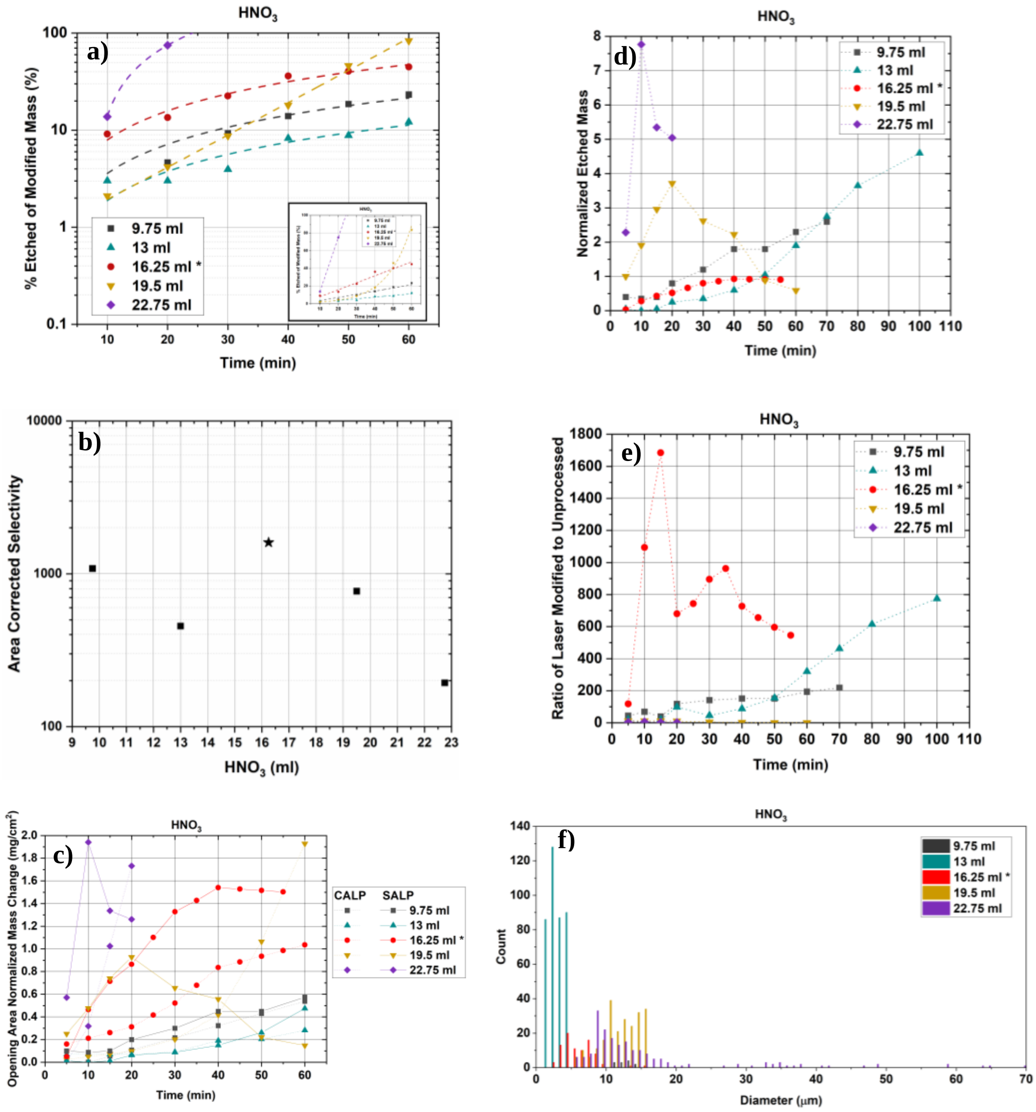

Figure 3.16 Etch rate of laser modified region over time by changing the HNO_3 concentrations from 9.75 to 22.75 ml in 100 ml of solution for CALP (a); The selectivity of laser modified region comparing to unprocessed sample by fitting the etch rates over time for CALP (b); The area corrected etched mass of laser modified region for SALP (solid line) and CALP (dashed line) for different concentrations over 60 minutes (c); Normalized etched mass of laser modified region for SALP (d); The ratio of area normalized etched mass of laser modified region over the unprocessed region for SALP (e); Etch pit radius distribution obtained from SEM images by analyzing the surface morphology (f).

Copper ions are adsorbed on the Si surface. These ions attract minority negative charge carriers available in the p-type Si substrate. Thus, CuNPs collect electrons through Cu/Si interface and transfer them to the solution. The conglomeration speed of CuNPs depends on the speed of metal ion removal. So, if the formation of the NPs is slower than the removal of it, there will be many holes on the surface which will continue growing larger and larger.

The amounts of oxidizing and reducing agents control how fast and aggressive the copper removes Si from the silicon surface for a certain copper amount. As a result, by fixing the amount of $Cu(NO_3)_2$ to 1 g, the combination of oxidation and reduction creates the intended structure. By tuning the oxidizing agent – HNO_3, it is possible to minimize the aggressiveness of the oxidation process in such a way that despite some distinct holes at surface, the etchant does not completely damage the Si surface and cause porosity. As discussed previously, increasing the HNO_3 controls the formation of the oxide on the NPs which are later etched by HF. On the one hand, presence of high amount of HNO_3 in a given concentration of HF i.e. 14 ml in 100 ml solution, causes NPs to rapidly become smaller. As a result, increasing HNO_3 makes the surface porous. On the other hand, the NPs must be maintained long enough, so that the desired structure can be achieved.

As can be seen in Figure 3.16 (a, b), both etch rates and selectivity increase by increasing the HNO_3 concentration in the CALP structure. This confirms that increasing the amount of oxidizing agent in the solution increases the etch rate of the laser modified region more than the unprocessed sample. This behavior is due to the generation of more excess hole carries at the surface which accelerates the anodic chemical reactions. In Figure 3.16 (c), the laser modified etched mass in SALP goes higher than subsurface except for a higher dose concentration of HNO_3. In Figure 3.16 (d), the etched mass of laser modified divided by total etched mass is increased and harshly attacked on both regions by the increasing amount of HNO_3 concentration as the etching time increases. The quality of etched surface is a function of HNO_3, i.e., increasing the amount of HNO_3 will result in the formation of engraved surface (Figure 3.16 (e)). In addition, Figure 3.16 (f) shows the etch pit radius size distribution is in the range of 1 – 70 µm except for the cases when HNO_3 concentration is high.

After surveying the abovementioned chemical compositions, we have achieved to determine the optimal concentrations of $HF:HNO_3:CH_3COOH:H_2O$ – 56:65:72:207 with 0.01 g/ml $Cu(NO_3)_2.3H_2O$ which we refer to as *the Champion Etchant*. The enhanced composition yields more chemical treatment time required for the specific applications. It is also dopant-type dependent and anisotropic (See section 3.3.1), which is beneficial for certain applications to etch laser-modified silicon regions. The comparisons between MEMC and the enhanced composition in terms of orientation dependency and dopant type dependency are discussed in section 3.3.1.

CHAPTER 4

APPLICATIONS OF ENHANCED SELECTIVE CHEMICAL ETCHING

4.1 Thin crystalline silicon slicing

Kerf-reduced slicing of bulk c-Si is of high commercial interest in photovoltaics industry. There are different techniques to produce thin c-Si slices; including chemical etching in highly concentrated potassium hydroxide (KOH) [143], stress induced lift-off method (SLIM)-cut [144], controlled spalling process [145,146], porous Si based lift-off [147] and the semiconductor on metal [148]. In these techniques, a large fraction of the initial c-Si wafer thickness is wasted. Moreover, industry continues to move towards thinner Si wafers. In this context, novel schemes alternative to wire-cutters for Si wafer are explored for achieving slicing with minimal material loss. We proposed laser-induced c-Si thin film slicing (LASIS) as a new technique in which the thin c-Si slices are produced with minimum loss of the material. A nanosecond-pulsed fiber laser focused deep in Si subsurface induces structural modifications near the focal point due to multiphoton absorption [149]. After laser processing, we demonstrated the development of a Cu $(NO_3)_2$ based etching solution on the application of subsurface laser modified region in Si result in obtaining c-Si slice [34]. The produced Si slice based on LASIS method is utilized in the fabrication of c-Si solar cells.

4.1.1 Overview of LASIS technique:

In this method firstly, a nanosecond-pulsed fiber laser operating at 1.55 µm wavelength is focused to the silicon cross-section process under the surface. The raster scan of the focal position inside of the sample produces a plain of 2D modified Si region. The Si wafers are scanned with different length in the x-y plane. Finally, the modified silicon regions are etched by $Cu(NO_3)_2$ based selective chemical etchant which targets the laser-modified regions and a silicon slice is formed [34]. Figure 4.1 outlines the conceptual and the fabrication procedure of LASIS method.

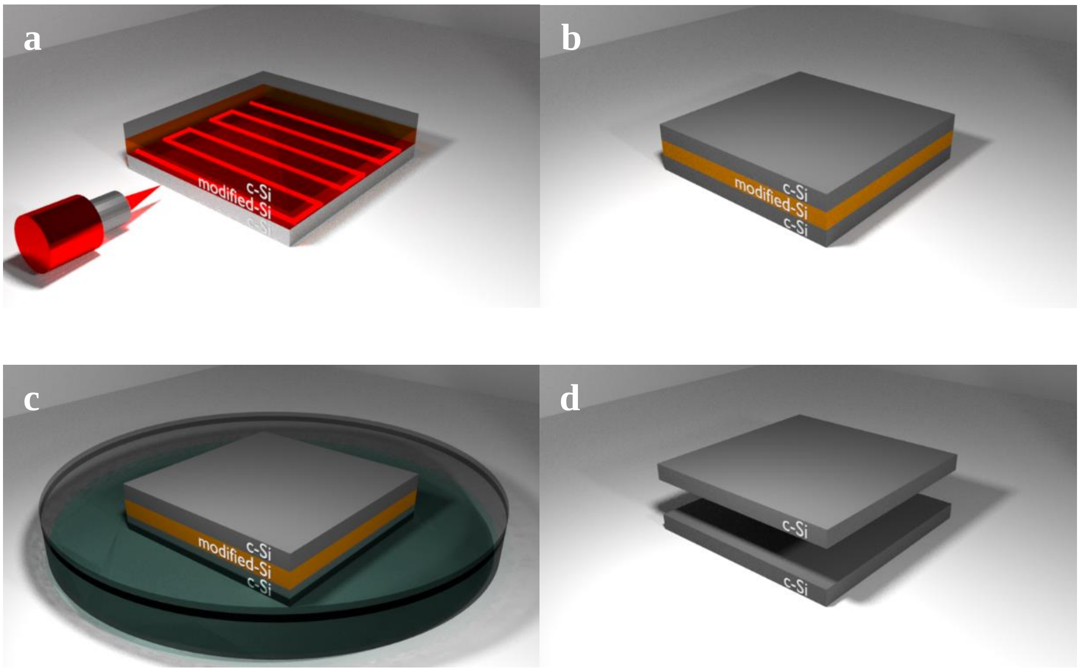

Figure 4.1 Steps of LASIS silicon micro slicing processes: Laser processing of subsurface (a), Modified part after laser processing (b), Selective chemical etching (c), Slicing into plates (d).

4.1.2 Si slices production based on selective etching of laser-modified region

In order to selectively remove the laser subsurface modified area, enhanced $Cu(NO_3)_2$ based chemical solution was utilized. Figure 4.2 shows the SEM cross-sectional images of different stages of laser-processed c-Si wafer, after 20 minutes etching (Figure 4.2 (a) and (d)) to slice formation etching (Figure 4.2 (c) and (f)).

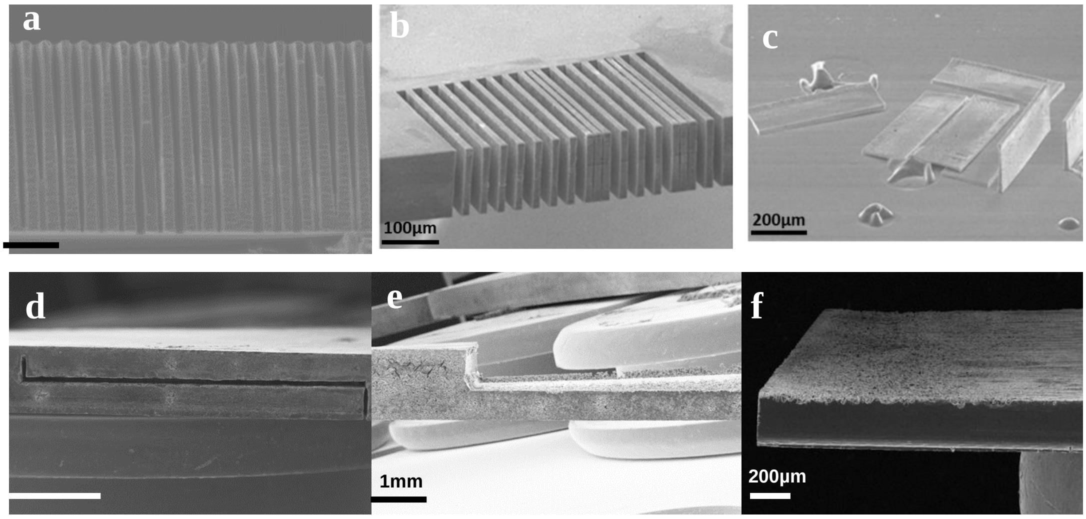

Figure 4.2 SEM images of 20 minutes etching (a), After 60 min etching (b), produced c- Si slice with 1mm × 0.5 mm area (c), After 20 min etching (d), After 3 hours etching (e), produced c-Si slice with 10 mm × 5 mm area (f).

LASIS method enables slicing Si wafers into multi-thin slices. The amount of Si material utilized in a photovoltaic (PV) cell will be decreased by an order of magnitude with this method. Since Si is one of the main cost-determining factors in PV cell production, therefore, it has the potential to decrease PV cell fabrication costs essentially. The SEM images of the first multi-slices shown in Figure 4.3.

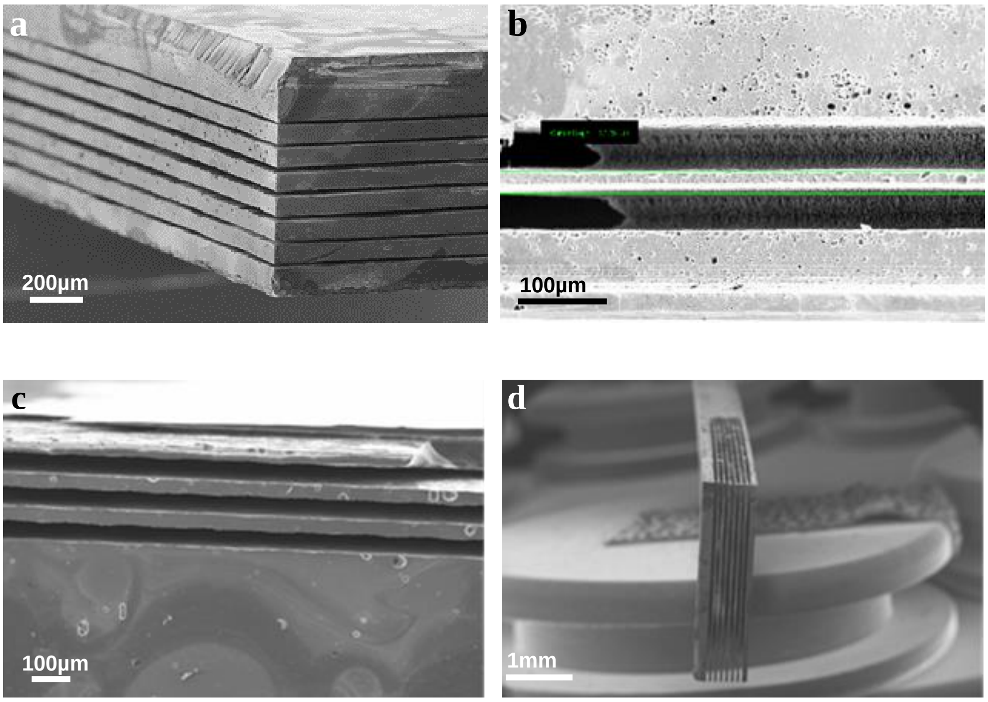

Figure 4.3 SEM images of multi-layers after 30 min etching, the thicknesses of slicing are: ~80 µm (a), ~60 µm (b), ~ 45 µm (c), ~35 µm (d).

As seen in Figure 4.3, the modified silicon regions are etched by $Cu(NO_3)_2$ based selective chemical etchant after 30 min etching and multi-layers are successfully produced by LASIS method. The distance between layers which are processed by laser are 100 µm.

4.1.3 Solar cell fabricated based on Si slice processed by LASIS method

The produced Si slice based on LASIS method in Figure 4.2 (f) is utilized in the fabrication of c-Si solar cell. The structure of the solar cell is depicted in Figure 4.4 (a). p-type c-Si slice performed by phosphorous diffusion ($POCL_3$) to create the junction and n^+ back surface field (BSF). The surface of the phosphorous diffusion (n^+) was passivated with SiO_2/ SiN_x stack layers. Silicon nitride (SiN_x) was deposited on the front side as antireflective coating (ARC). The front and back side metal contacts are screen-printed with Ag and Al-BSF. The highest attained efficiency is ~9% with a V_{oc} of 495 mV, J_{sc} of 29.31 mA/cm^2 and FF of 62.61% Figure 4.4 (b).

These values are low compared with the possible attained values from the same structure, yet they prove the applicability of c-Si slices produced by the LASIS method in the production of photovoltaic solar cell devices using industrialized fabrication techniques.

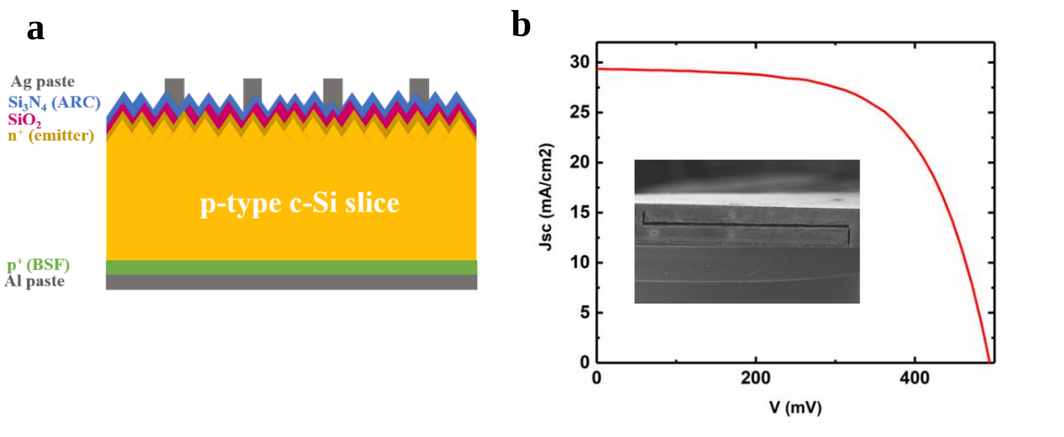

Figure 4.4 Schematic of c-Si solar cell structure (a), J-V curve of the first solar cell fabricated from LASIS Thin Sliced c-Si based on Al-BSF design (b).

4.2 High aspect ratio micro pillar arrays on Si

Micropillar or nanowire arrays have been of interest for solar applications due to the increased light trapping and high carrier collecting efficiency inherent in the pillar or wire structure. Light trapping of the solar incoming light can be achieved by texturing the surface of the solar cell. Numerous methods are available, including nanowires [150], inverted pyramids [109], plasmonic metal NPs [151], etc., on the cell surface. In this study, we demonstrate laser-induced Si pillar technology to produce micron-size pillars array on c-Si wafers. The aim of fabricating micro pillar arrays on the surface of Si wafers is to trap light in the region between the pillars via multiple reflections. This technology allows obtaining a controllable sizes/depth combination of the pillar in the various ranges in two-step fabrication in Si. The first step is laser processing, which focused on the surface of Si, induces structural modifications near the focal point due to multiphoton absorption. The raster scan of the focal position on the Si surface produces a pillar structure on Si wafer. The second step is etching of the modified regions with the developed selective chemical etching recipe. Figure 4.5 depicts the fabrication procedure of micro pillar. The modified regions are etched away by our developed chemical etchant to selectively attack the laser-modified regions at high rates. In order to achieve a high etch rate and smooth and defect-free surface, enhanced composition of $HF:HNO_3:CH_3COOH:H_2O$ – 14:16.25:18:51.75 with 1 g of $Cu(NO_3)_2.3H_2O$ has been used. The optical characteristics of a Si substrate are investigated when the depth/ sizes of micro pillar array are varied by using this method. With this technique, micro-pillar with an area of less than ~9 µm and 118 µm depth were successfully developed and fabricated. Additionally, periodic arrays of pillars with controlled sizes/depth were fabricated with this advanced technology. SEM images of various fabricated micro-pillars are shown in Figure 4.6. The 2mm×2mm total area covered with pillars can be revealed in 20 minutes etching duration.

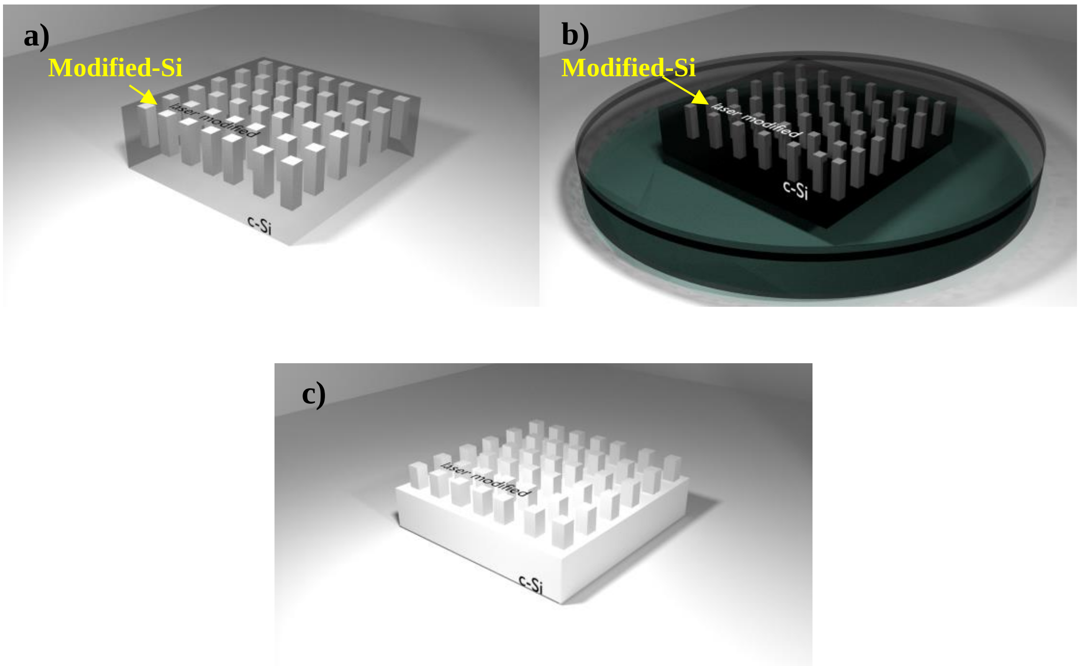

Figure 4.5 Steps of micro pillar processes: Modified part after laser processing pattern of pillar (a), Selective chemical etching (b), Pillar arrays (c).

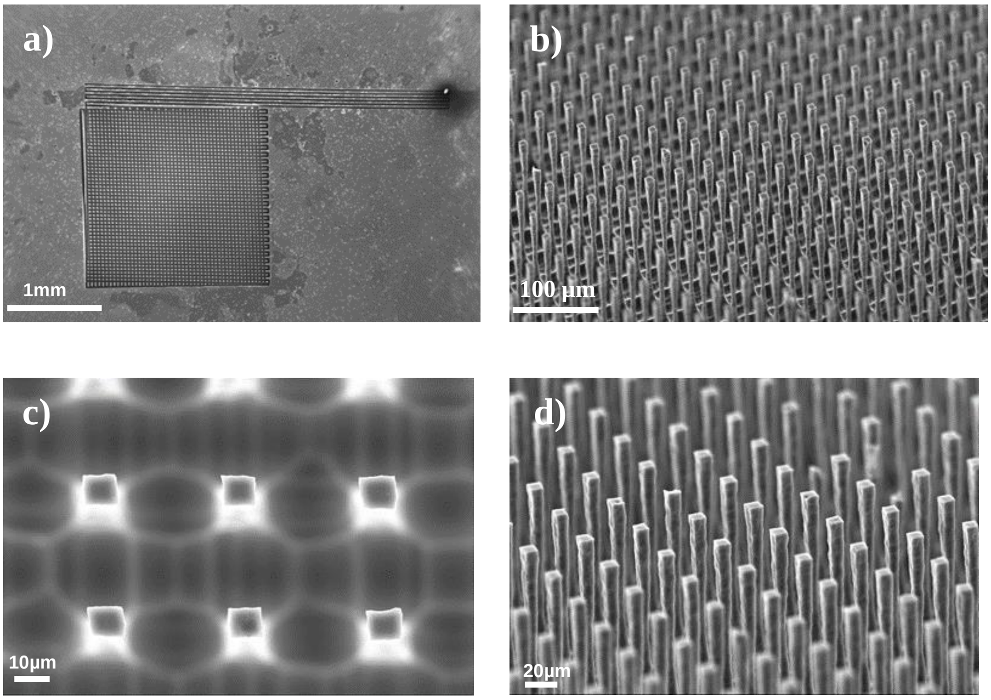

Figure 4.6 SEM images of micro-pillar arrays from top surface (a, c), 40° tilted (b), 60° tilted (d) with pillar area: 9 μm × 9 μm, Pillar depth of 118 μm and pulse energy 3 μj.

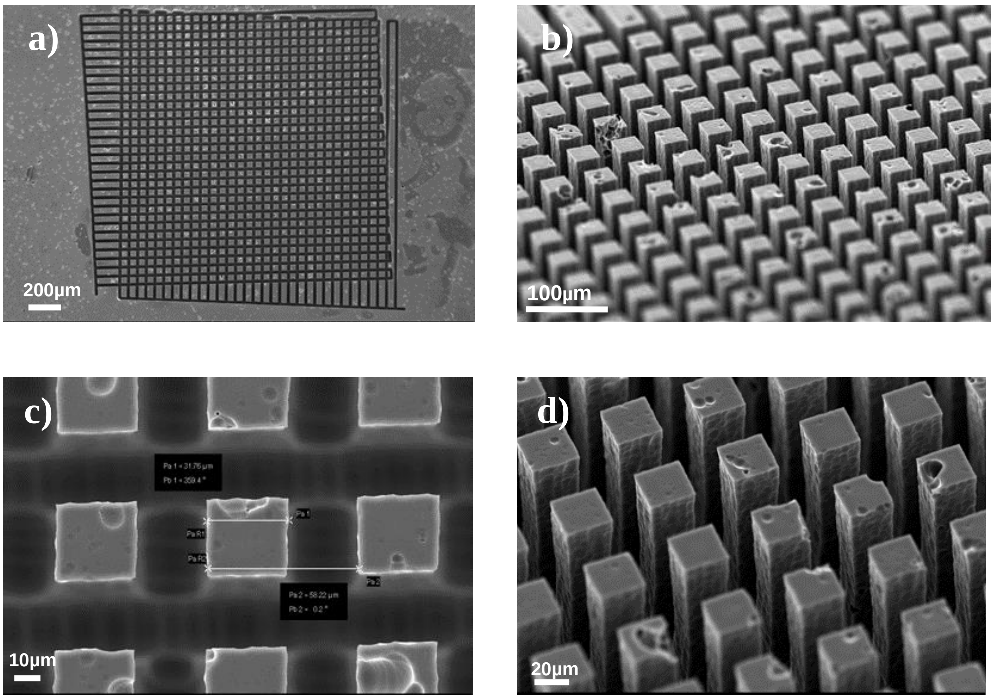

Figure 4.7 SEM images of micro-pillar arrays from top surface (a, c), 60° tilted (b), 40° tilted (d) with pillar area: 31 µm × 31 µm, Pillar depth of 158 µm and pulse energy 3 µj.

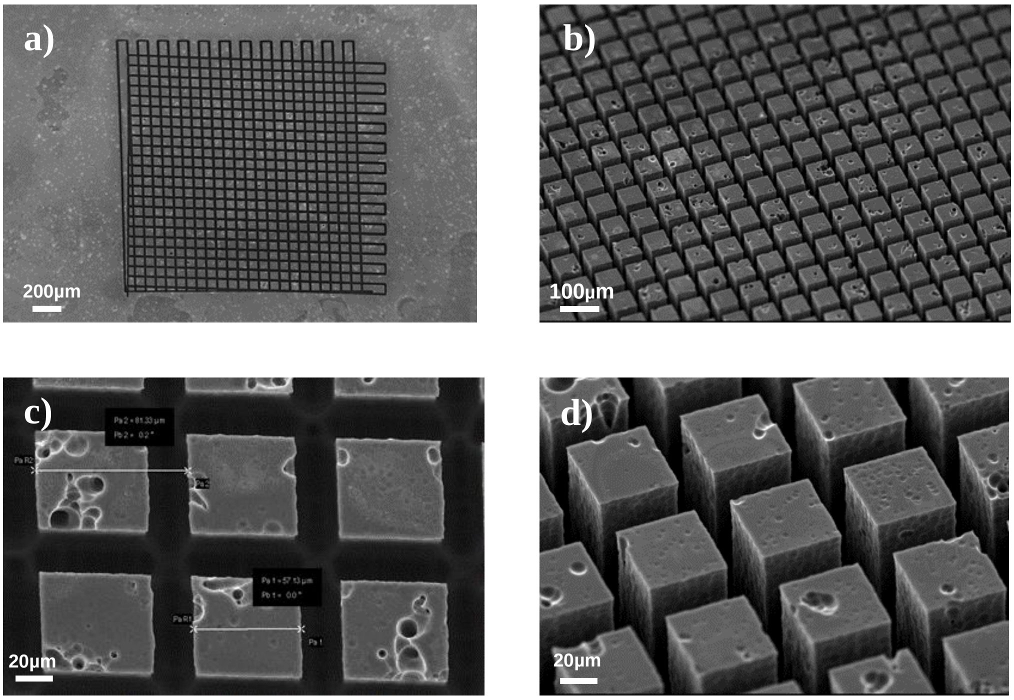

Figure 4.8 SEM images of micro-pillar arrays from top surface (a, c), 40° tilted (b,d), with pillar area: 57 µm × 57 µm, and pulse energy 3 µj.

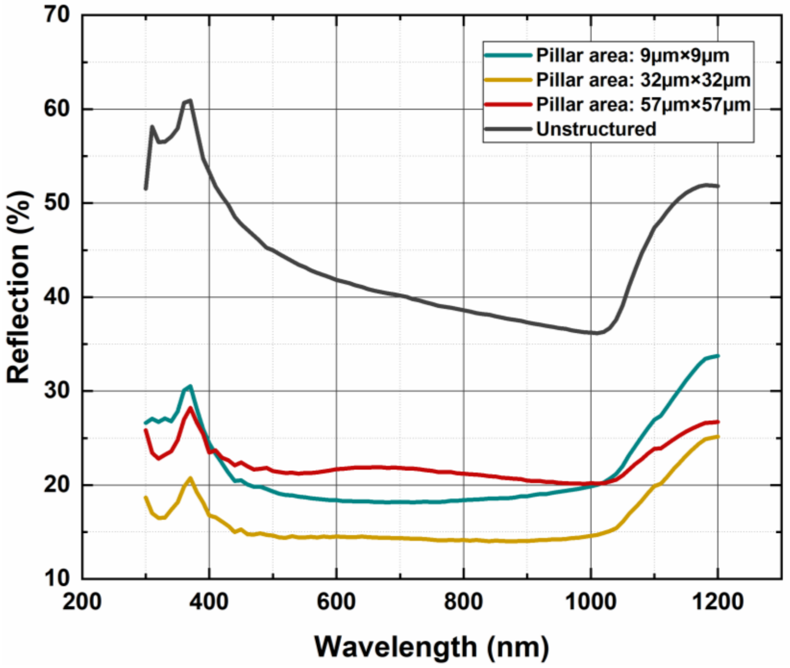

Figure 4.9 Measured total reflection of the fabricated micro pillars with various areas and individual depth.

Various surface coverage (Si/air) and various individual pillar properties (depth, area) resulted in different reflection response as displayed in Figure 4.9. As can be shown, the micro pillar array solar cells give better performance than the unstructured surface.

The surface coverage for 9 µm × 9 µm pillar (Figure 4.6) is as low as ~5%, therefore, the unstructured region between the pillars is large. This enables large fraction of the sunlight to leave the unstructured regions between the pillar with a minimum of multiple reflections. However, the surface coverage for 57 µm × 57 µm pillar (Figure 4.8) is large (~56.25%), and the unstructured regions between the pillars is very small. This enables large fraction of the sunlight to be reflected at the top surface of the micro pillars. For an optimum amount of surface coverage, in between these ranges, which is corresponding to 31 µm × 31 µm pillar (Figure 4.7), the light can be trapped by multiple reflections resulting in lowest relative total reflectance. As can be observed from Figure 4.9, surface coverage of ~25% is found to the optimum for square micro-pillars with minimum reflection response. As a result, more multiple reflections occur, giving a lower reflectance which leads to improved light trapping in photonic structure and solar cell applications.

4.3 High aspect ratio micro-hole drilling on Si

As an application of 3D sculpting, achieving high aspect ratio hole drilling in Si is interesting for microfluidics and Via formation in Si electronics [90,152]. We demonstrated laser-induced Si drilling technology to fabricate micron-size holes in c-Si wafers. The laser is focused deep in Si, induces structural modifications near the focal point due to multiphoton absorption. The holes scan of the focal position inside Si, positioned in the back surface plane with a single circular motion of the laser beam, produces quasi-2D modified Si regions. The modified regions are then etched by our developed chemical etchant to selectively attack the laser-modified regions at high rates. Figure 4.10 demonstrate the fabrication procedure of micro holes. In order to achieve a high etch rate and smooth and defect-free surface, enhanced composition of $HF:HNO_3:CH_3COOH:H_2O$ – 14:16.25:18:51.75 with 1 g of $Cu(NO_3)_2.3H_2O$ has been used. This technology allows obtaining a controllable hole diameter in the range of less than 10 µm in two-step fabrication in Si. The first step is laser processing, and the second step is the removal of modified regions with selective chemical etching. With this technique, micro-holes with a diameter of less than ~10 µm were successfully developed and fabricated for 90 minutes etching with a depth of 250 µm. Additionally, periodic arrays of holes with controlled depth and diameter were fabricated with this advanced technology. SEM images of hole diameter through-hole with a depth of 250 µm and average various holes diameter size as a function of the pulse energy are shown in Figure 4.11.

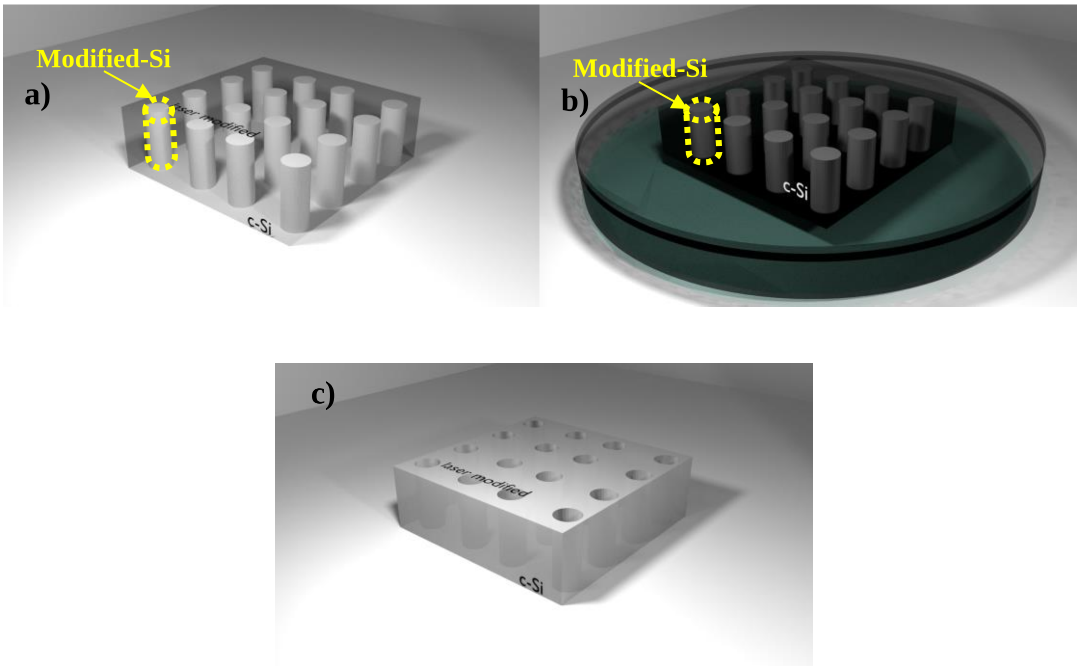

Figure 4.10 Steps of micro hole processes: Modified part after single circular motion of the laser processing (a), Selective chemical etching (b), Periodic hole drilling (c).

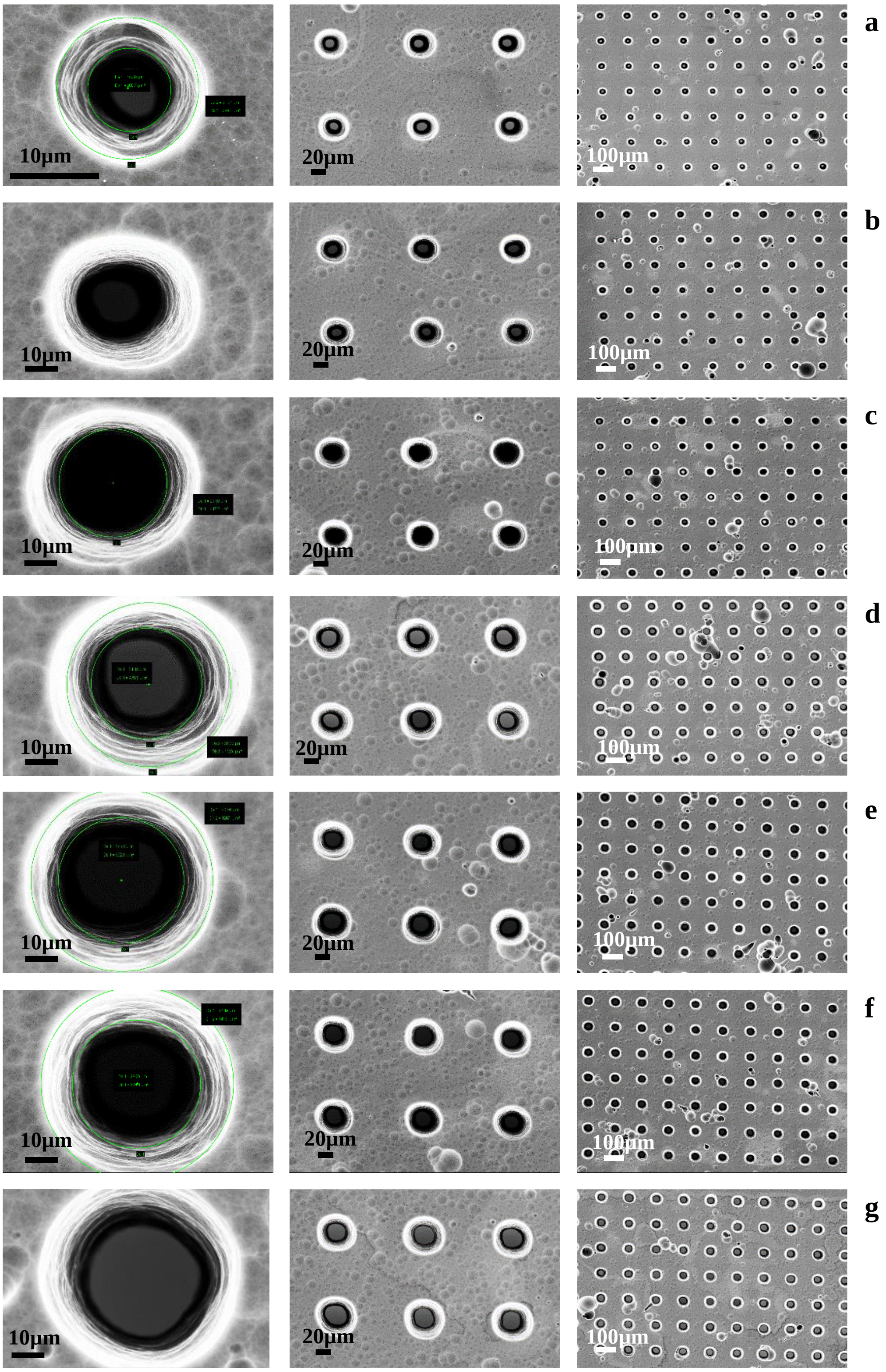

Figure 4.11 Top view SEM images of laser-processed drilled holes in c-Si wafer at different pulse energy: 2 µJ (a), 2.5 µJ (b), 3 µJ (c), 3.5 µJ (d), 4 µJ (e),4.5 µJ (f) and 5 µJ (g), after 90 minutes etching.

As can be seen in Figure 4.11 (a-g) shows top-view SEM images of micro-holes with high aspect ratio produced at various laser pulse energies. Micro holes with a different diameter were successfully developed and fabricated for 90 minutes etching with a depth of 250 µm.

Table 4.1 Various hole diameter values relative to laser pulse energy

Pulse energy (µJ)	2	2.5	3	3.5	4	4.5	5
Avg hole diameter (µm)	10.5	20	23.9	24.4	27.7	28.3	34.5

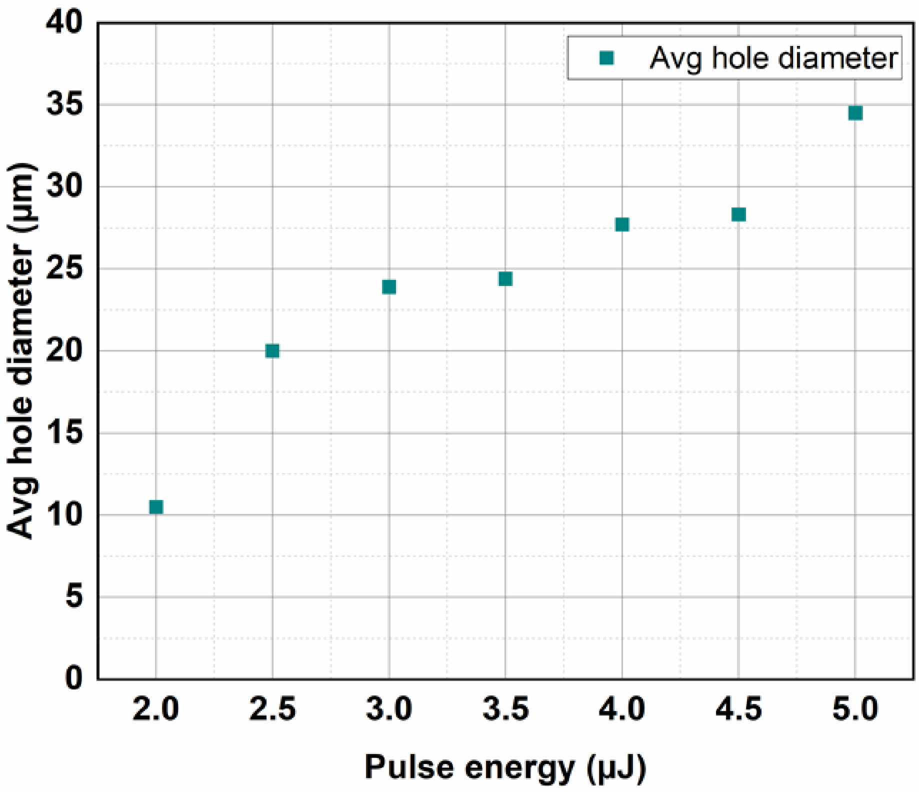

Figure 4.12 Average various holes diameter size as a function of the pulse energy.

As it is shown, by increasing laser pulse energy (see Table 4.1 and Figure 4.12), hole diameter varies with increasing tendency as 10.5 µm, 20 µm, 23.9 µm, 24.4 µm, 27.7

µm, 28.3 µm, and 34.5 µm. Well-controlled various depth and sizes of holes are feasible by using different pulse energies and selective chemical processes.

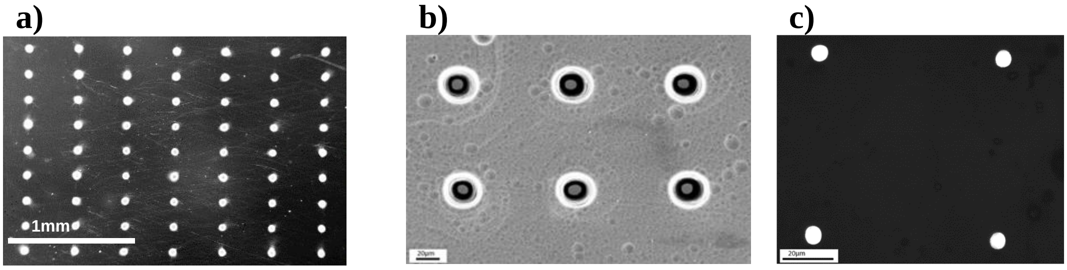

Figure 4.13 Top-view SEM images of laser-processed drilled holes at 5 µJ pulse energy and chemically treated c-Si with selective etchant recipes: hole laser processing before etching (a), enhanced composition after 90 minutes etching (b), optical microscope image of the produced drilled holes (c).

Figure 4.13 (a-c) shows the drilled holes with close-to-perfect circular geometry. Figure 4.13 (b) shows the top-view SEM of micro-holes with aspect ratio (defined as depth/width) as high as 14 with 250 µm depth and ~10.5 µm diameter within minutes of etching. The transmission mode optical microscope image of the same holes, shown in Figure 4.13 (c), indicates that laser drilled holes are correctly processed all the way through the wafer and are fully opened by the selective chemical etching. Theses holes indicate that laser drilled holes are completely opened during the chemical etching. The demonstrated laser drilling technique has the potential to be utilized in the fabrication and development of microfluidic devices, photonic devices, pressure sensors, gyroscopes, flowmeters, and biomedical devices on Si wafers.

CHAPTER 5

CONCLUSION

The optimization of a $Cu(NO_3)_2$-based etching solution on the novel application of surface and subsurface laser modified regions (CALP and SALP) is presented. The laser modifications are done by utilizing a nanosecond IR fiber laser on the p-type c-Si wafers. The laser modified samples are treated with a number of MEMC-like etchants in which the chemical component concentrations are varied in order to survey for an especially optimal etchant for laser modified Si. For investigating the effect of each component, different sets of solutions are prepared by changing the concentrations. To obtain the etch rates, the mass difference of laser modified and unprocessed samples are measured up to 60 minutes. By applying correction factors of initial mass, etch opening, and attack area, the mass reduction of the laser modified region and unprocessed c-Si samples are calculated. The selectivity of each set calculated as ratio of laser modified region and unprocessed c-Si samples. The c-Si smoothness is represented by calculating etch pit radius size distribution which obtained from SEM images after 60 minutes. The etch rate, selectivity, and surface morphology of subsurface laser modified regions are well controlled during the experiments by varying the etching concentration of the etching solution components. The selection of the component concentrations depends on the desired applications since different combination of etch rate, selectivity, and surface morphology can be achieved. For instance, decreasing $Cu(NO_3)_2$ to 0.75 g in 100 ml solution leads to fast and selective etching at the cost of c-Si surface smoothness. In addition, decreasing HNO_3 leads to low etch rate and selectivity while providing smooth c-Si surface morphology. Some applications which may use small samples require high selectivity but low etch rate which can be achieved by increasing the $Cu(NO_3)_2$ to 2 g in 100 ml solution. After an extensive survey of component concentrations, we achieved an optimum composition of $HF:HNO_3:CH_3COOH:H_2O$

– 56:65:72:207 with 0.01 g/ml $Cu(NO_3)_2.3H_2O$ as *the champion etchant* for surface and subsurface laser modified Si which shows more than 1600 selectivity which was not demonstrated in the literature before for laser processed region as well as etch pit sizes in the range of 1 – 10 µm indicating relatively smooth and low defective surface. In addition, by comparing SALP and CALP results, it is concluded that surface etching has higher etch rate which is expectable due to heat transfer and diffusion restrictions in the subsurface samples.

In order to demonstrate the capacity of this especially optimized etchant in an application, we demonstrate the LASIS technique as a first application that enables the multi-thin slicing of Si wafers. This technique allows for a significant reduction in the amount of Si material used in photovoltaic (PV) cells. Due to the fact that Si is one of the main cost-determining factors in PV cell manufacturing, the produced Si slice based on LASIS method has the potential to significantly reduce the cost of photovoltaic cell fabrication. The first solar cell fabricated attained efficiency is ~9% with a V_{oc} of 495 mV, J_{sc} of 29.31 mA/cm^2 and FF of 62.61%.

As a second application, micro-pillar with an area of less than ~9 µm and 118 µm depth were successfully demonstrated and produced. The purpose of fabricating micro pillar arrays on the surface of Si wafers is to trap light through multiple reflections in the area between the pillars. This technique enables the manufacture of a pillar with a controlled size/depth combination in a variety of ranges in a two-step process in Si. The 2mm×2mm total areas are covered with various pillars, including 9 µm × 9 µm, 31 µm × 31 µm and 57 µm × 57 µm corresponding the surface coverage of ~5%, ~25% and ~56.25%, respectively, can be revealed in 20 minutes etching duration. Surface coverage of ~25% is found to the optimum for square micro-pillars with minimum reflection response. This sophisticated technology was used to fabricate periodic arrays of pillars with controlled aspect ratio to reach minimum multiple reflections to improve light trapping for photonic structure and solar cell applications.

As a third application, we have fabricated micro-holes with laser power-controlled diameters with aspect ratio of 14 all the way through 250-micron thick c-Si wafers.

This technique enables two-step fabrication in Si to achieve a controlled hole diameter in the range of less than 10 µm and produced for 90 minutes at a depth of 250 µm. By increasing laser pulse energy, hole diameter varies with increasing tendency as 10.5 µm, 20 µm, 23.9 µm, 24.4 µm, 27.7 µm, 28.3 µm, and 34.5 µm. As a result using a variety of pulse energies and selective chemical processes, it is possible to create holes of varying depths and diameters with high precision.The demonstrated laser drilling technique has the potential to be utilized in the fabrication and development of microfluidic devices, photonic devices, pressure sensors, gyroscopes, flowmeters, and biomedical devices on Si wafers.

REFERENCES

[1] D. Liang, G. Roelkens, R. Baets, J.E. Bowers, Hybrid integrated platforms for silicon photonics, Materials (Basel). 3 (2010) 1782–1802. https://doi.org/10.3390/ma3031782.

[2] F. Paquin, J. Rivnay, A. Salleo, N. Stingelin, C. Silva, Multi-phase semicrystalline microstructures drive exciton dissociation in neat plastic semiconductors, J. Mater. Chem. C. 3 (2015) 10715–10722. https://doi.org/10.1039/b000000x.

[3] B. Jalali, S. Fathpour, Silicon photonics, J. Light. Technol. 24 (2006) 4600–4615. https://doi.org/10.1109/JLT.2006.885782.

[4] A.J. Pedraza, J.D. Fowlkes, D.H. Lowndes, Silicon microcolumn arrays grown by nanosecond pulsed-excimer laser irradiation, Appl. Phys. Lett. 74 (1999) 2322–2324. https://doi.org/10.1063/1.123838.

[5] G.D. Tsibidis, M. Barberoglou, P.A. Loukakos, E. Stratakis, C. Fotakis, Dynamics of ripple formation on silicon surfaces by ultrashort laser pulses in subablation conditions, Phys. Rev. B - Condens. Matter Mater. Phys. 86 (2012) 1–14. https://doi.org/10.1103/PhysRevB.86.115316.

[6] A. Serpenguzel, Luminescence of black silicon, J. Nanophotonics. 2 (2008) 021770. https://doi.org/10.1117/1.2896069.

[7] M. Shen, J.E. Carey, C.H. Crouch, M. Kandyla, H.A. Stone, E. Mazur, High-density regular arrays of nanometer-scale rods formed on silicon surfaces via femtosecond laser irradiation in water, Nano Lett. 8 (2008) 2087–2091. https://doi.org/10.1021/nl080291q.

[8] A.Y. Vorobyev, C. Guo, 2010_Vorobyev_A.Y. Vorobyev and C. Guo, Opt. Express 18, 6455–6460, 18 (2010) 6455–6460.

[9] H. Misawa, 3D Laser Microfabrication, 2006.

[10] R.R. Gattass, E. Mazur, Femtosecond laser micromachining in transparent materials, Nat. Photonics. 2 (2008) 219–225. https://doi.org/10.1038/nphoton.2008.47.

[11] C.W. Carr, H.B. Radousky, A.M. Rubenchik, M.D. Feit, S.G. Demos, Localized Dynamics during Laser-Induced Damage in Optical Materials, Phys. Rev. Lett. 92 (2004) 1–4. https://doi.org/10.1103/PhysRevLett.92.087401.

[12] B. Stuart, M. Feit, S. Herman, A. Rubenchik, B. Shore, M. Perry, Nanosecond-to-femtosecond laser-induced breakdown in dielectrics, Phys. Rev. B - Condens. Matter Mater. Phys. 53 (1996) 1749–1761. https://doi.org/10.1103/PhysRevB.53.1749.

[13] K.M. Davis, K. Miura, N. Sugimoto, K. Hirao, Writing waveguides in glass

with a femtosecond laser, Opt. Lett. 21 (1996) 1729. https://doi.org/10.1364/ol.21.001729.

[14] G.D. Marshall, J.C.F. Matthews, A. Politi, P. Dekker, M. Ams, M.J. Withford, J.L. O'Brien, Quantum optics in laser-written waveguide circuits, Opt. InfoBase Conf. Pap. 17 (2009) 646–649. https://doi.org/10.1364/iqec.2009.imi7.

[15] A.M. Kowalevicz, V. Sharma, E.P. Ippen, J.G. Fujimoto, K. Minoshima, Three-dimensional photonic devices fabricated in glass by use of a femtosecond laser oscillator, Opt. Lett. 30 (2005) 1060. https://doi.org/10.1364/ol.30.001060.

[16] Y. Nasu, M. Kohtoku, Y. Hibino, Low-loss waveguides written with a femtosecond laser for flexible interconnection in a planar light-wave circuit, Opt. Lett. 30 (2005) 723. https://doi.org/10.1364/ol.30.000723.

[17] S. Nolte, M. Will, J. Burghoff, A. Tuennermann, Femtosecond waveguide writing: A new avenue to three-dimensional integrated optics, Appl. Phys. A Mater. Sci. Process. 77 (2003) 109–111. https://doi.org/10.1007/s00339-003-2088-6.

[18] G. Corrielli, A. Crespi, R. Geremia, R. Ramponi, L. Sansoni, A. Santinelli, P. Mataloni, F. Sciarrino, R. Osellame, Rotated waveplates in integrated waveguide optics, Nat. Commun. 5 (2014) 1–6. https://doi.org/10.1038/ncomms5249.

[19] O. Tokel, A. Turnall, G. Makey, P. Elahi, T. Çolakoğlu, E. Ergeçen, Ö. Yavuz, R. Hübner, M. Zolfaghari Borra, I. Pavlov, A. Bek, R. Turan, D.K. Kesim, S. Tozburun, S. Ilday, F.Ö. Ilday, In-chip microstructures and photonic devices fabricated by nonlinear laser lithography deep inside silicon, Nat. Photonics. 11 (2017) 639–645. https://doi.org/10.1038/s41566-017-0004-4.

[20] I. Pavlov, E. Dülgergil, E. Ilbey, F.Ö. Ilday, Diffraction-limited, 10-W, 5-ns, 100-kHz, all-fiber laser at 155 μm, Opt. Lett. 39 (2014) 2695. https://doi.org/10.1364/ol.39.002695.

[21] and F.Ö.I. A. Turnali, O.Toke, I. Pavlov, Direct Laser Writing of Volume Fresnel Zone Plates in Silicon, in: European Conference on Lasers and Electro-Optics - European Quantum Electronics Conference, 2015.

[22] A.H. Nejadmalayeri, P.R. Herman, J. Burghoff, M. Will, S. Nolte, A. Tünnermann, Inscription of optical waveguides in crystalline silicon by mid-infrared femtosecond laser pulses, Opt. Lett. 30 (2005) 964. https://doi.org/10.1364/ol.30.000964.

[23] A. Mouskeftaras, A. V. Rode, R. Clady, M. Sentis, O. Utéza, D. Grojo, Self-limited underdense microplasmas in bulk silicon induced by ultrashort laser pulses, Appl. Phys. Lett. 105 (2014). https://doi.org/10.1063/1.4901528.

[24] S. Leyder, D. Grojo, P. Delaporte, W. Marine, M. Sentis, O. Utéza,

Multiphoton absorption of 1.3 μm wavelength femtosecond laser pulses focused inside Si and SiO 2 , 17th Int. Sch. Quantum Electron. Laser Phys. Appl. 8770 (2013) 877004. https://doi.org/10.1117/12.2016857.

[25] V. V. Kononenko, V. V. Konov, E.M. Dianov, Delocalization of femtosecond radiation in silicon, Opt. Lett. 37 (2012) 3369. https://doi.org/10.1364/ol.37.003369.

[26] D. Grojo, A. Mouskeftaras, P. Delaporte, S. Lei, Limitations to laser machining of silicon using femtosecond micro-Bessel beams in the infrared, J. Appl. Phys. 117 (2015). https://doi.org/10.1063/1.4918669.

[27] Y. Ito, H. Sakashita, R. Suzuki, M. Uewada, K.P. Luong, R. Tanabe, Modification and machining on back surface of a silicon substrate by femtosecond laser pulses at 1552 nm, J. Laser Micro Nanoeng. 9 (2014) 98–102. https://doi.org/10.2961/jlmn.2014.02.0004.

[28] and F.O.I. O. Tokel, A. Turnali, I. Pavlov, S. Tozburun, I. Akca, Laser-writing in silicon for 3D information processing, (2014).

[29] S. Jesse, A.J. Pedraza, J.D. Fowlkes, J.D. Budai, Etching-enhanced ablation and the formation of a microstructure in silicon by laser irradiation in an SF6 atmosphere, J. Mater. Res. 17 (2002) 1002–1013. https://doi.org/10.1557/JMR.2002.0148.

[30] T.H. Her, R.J. Finlay, C. Wu, S. Deliwala, E. Mazur, Microstructuring of silicon with femtosecond laser pulses, Appl. Phys. Lett. 73 (1998) 1673–1675. https://doi.org/10.1063/1.122241.

[31] D. Riedel, J.L. Hernandez-Pozos, R.E. Palmer, K.W. Kolasinski, Fabrication of ordered arrays of silicon cones by optical diffraction in ultrafast laser etching with SF6, Appl. Phys. A Mater. Sci. Process. 78 (2004) 381–385. https://doi.org/10.1007/s00339-002-1938-y.

[32] D. Mills, K.W. Kolasinski, Laser-etched silicon pillars and their porosification, J. Vac. Sci. Technol. A Vacuum, Surfaces, Film. 22 (2004) 1647–1651. https://doi.org/10.1116/1.1690253.

[33] D. Mills, K.W. Kolasinski, Non-lithographic method of forming ordered arrays of silicon pillars and macropores, J. Phys. D. Appl. Phys. 38 (2005) 632–636. https://doi.org/10.1088/0022-3727/38/4/017.

[34] O. Tokel, A. Turnall, G. Makey, P. Elahi, T. Çolakoğlu, E. Ergeçen, Ö. Yavuz, R. Hübner, M. Zolfaghari Borra, I. Pavlov, A. Bek, R. Turan, D.K. Kesim, S. Tozburun, S. Ilday, F.Ö. Ilday, In-chip microstructures and photonic devices fabricated by nonlinear laser lithography deep inside silicon, Nat. Photonics. 11 (2017) 639–645. https://doi.org/10.1038/s41566-017-0004-4.

[35] B. Miao, J. Zhang, X. Ding, D. Wu, Y. Wu, W. Lu, J. Li, Improved metal assisted chemical etching method for uniform, vertical and deep silicon structure, J. Micromechanics Microengineering. 27 (2017).

https://doi.org/10.1088/1361-6439/aa6872.

[36] L. Romano, M. Kagias, J. Vila-Comamala, K. Jefimovs, L.-T. Tseng, V.A. Guzenko, M. Stampanoni, Metal assisted chemical etching of silicon in the gas phase: a nanofabrication platform for X-ray optics, Nanoscale Horizons. 5 (2020) 869–879. https://doi.org/10.1039/c9nh00709a.

[37] N. Van Toan, M. Toda, T. Hokama, T. Ono, Cantilever with High Aspect Ratio Nanopillars on Its Top Surface for Moisture Detection in Electronic Products, Adv. Eng. Mater. 19 (2017) 1–5. https://doi.org/10.1002/adem.201700203.

[38] M.Z. Mohd Zin, E.H. Felix, Y. Wahab, M.N. Bakar, Process development and characterization towards microstructural realization using laser micromachining for MEMS, SN Appl. Sci. 2 (2020) 1–5. https://doi.org/10.1007/s42452-020-2715-2.

[39] R. Soref, Mid-infrared photonics in silicon and germanium, Nat. Photonics. 4 (2010) 495–497. https://doi.org/10.1038/nphoton.2010.171.

[40] Z. Fang, Q.Y. Chen, C.Z. Zhao, A review of recent progress in lasers on silicon, Opt. Laser Technol. 46 (2013) 103–110. https://doi.org/10.1016/j.optlastec.2012.05.041.

[41] X. Li, K. Tao, H. Ge, D. Zhang, Z. Gao, R. Jia, S. Chen, Z. Ji, Z. Jin, X. Liu, Improvement of saw damage removal to fabricate uniform black silicon nanostructure on large-area multi-crystalline silicon wafers, Sol. Energy. 204 (2020) 577–584. https://doi.org/10.1016/j.solener.2020.03.072.

[42] X. Wei, Z. Xiao, Z. Yue, H. Huang, L. Zhou, Texturization of diamond wire sawn multi-crystalline silicon wafers by micro-droplet etching, Mater. Sci. Semicond. Process. 115 (2020) 105075. https://doi.org/10.1016/j.mssp.2020.105075.

[43] R. Venkatesan, J. Mayandi, R. Søndenå, T.G. Finstad, V. Venkatachalapathy, Investigating antireflection properties of hybrid silicon nanostructures comprising rod-like nanopores and nano-textured surface, Mater. Lett. 275 (2020) 128087. https://doi.org/10.1016/j.matlet.2020.128087.

[44] T.E. Scheul, E. Khorani, T. Rahman, M.D.B. Charlton, S.A. Boden, Wavelength and angle resolved reflectance measurements of pyramidal textures for crystalline silicon photovoltaics, Prog. Photovoltaics Res. Appl. (2020) 1–10. https://doi.org/10.1002/pip.3319.

[45] J. Ding, S. Zou, J. Choi, J. Cui, D. Yuan, H. Sun, C. Wu, J. Zhu, X. Ye, X. Su, A laser texturing study on multi-crystalline silicon solar cells, Sol. Energy Mater. Sol. Cells. 214 (2020) 110587. https://doi.org/10.1016/j.solmat.2020.110587.

[46] T.H. Fung, T.P. Pasanen, Y. Zhang, A. Soeriyadi, V. Vähänissi, G. Scardera, D. Payne, H. Savin, M. Abbott, Improved emitter performance of RIE black

silicon through the application of in-situ oxidation during POCl3 diffusion, Sol. Energy Mater. Sol. Cells. 210 (2020). https://doi.org/10.1016/j.solmat.2020.110480.

[47] F. Es, G. Baytemir, M. Kulakci, R. Turan, Metal-assisted nano-textured solar cells with SiO2/Si3N4 passivation, Sol. Energy Mater. Sol. Cells. 160 (2017) 269–274. https://doi.org/10.1016/j.solmat.2016.10.032.

[48] L. Jiang, A.D. Wang, B. Li, T.H. Cui, Y.F. Lu, Electrons dynamics control by shaping femtosecond laser pulses in micro/nanofabrication: Modeling, method, measurement and application, Light Sci. Appl. 7 (2018) 1–27. https://doi.org/10.1038/lsa.2017.134.

[49] H. Tang, C. Di Franco, Z.Y. Shi, T.S. He, Z. Feng, J. Gao, K. Sun, Z.M. Li, Z.Q. Jiao, T.Y. Wang, M.S. Kim, X.M. Jin, Experimental quantum fast hitting on hexagonal graphs, Nat. Photonics. 12 (2018) 754–758. https://doi.org/10.1038/s41566-018-0282-5.

[50] H. Tang, X.F. Lin, Z. Feng, J.Y. Chen, J. Gao, K. Sun, C.Y. Wang, P.C. Lai, X.Y. Xu, Y. Wang, L.F. Qiao, A.L. Yang, X.M. Jin, Experimental two-dimensional quantum walk on a photonic chip, Sci. Adv. 4 (2018) 1–6. https://doi.org/10.1126/sciadv.aat3174.

[51] K. Kumar, K.K. Lee, J. Li, J. Nogami, N.P. Kherani, P.R. Herman, Quantized structuring of transparent films with femtosecond laser interference, Light Sci. Appl. 3 (2014) 1–7. https://doi.org/10.1038/lsa.2014.38.

[52] R. Osellame, H.J.W.M. Hoekstra, G. Cerullo, M. Pollnau, Femtosecond laser microstructuring: An enabling tool for optofluidic lab-on-chips, Laser Photonics Rev. 5 (2011) 442–463. https://doi.org/10.1002/lpor.201000031.

[53] R.G.H. Van Uden, R.A. Correa, E.A. Lopez, F.M. Huijskens, C. Xia, G. Li, A. Schülzgen, H. De Waardt, A.M.J. Koonen, C.M. Okonkwo, Ultra-high-density spatial division multiplexing with a few-mode multicore fibre, Nat. Photonics. 8 (2014) 865–870. https://doi.org/10.1038/nphoton.2014.243.

[54] K. Sugioka, J. Xu, D. Wu, Y. Hanada, Z. Wang, Y. Cheng, K. Midorikawa, Femtosecond laser 3D micromachining: A powerful tool for the fabrication of microfluidic, optofluidic, and electrofluidic devices based on glass, Lab Chip. 14 (2014) 3447–3458. https://doi.org/10.1039/c4lc00548a.

[55] M.S. Giridhar, K. Seong, A. Schülzgen, P. Khulbe, N. Peyghambarian, M. Mansuripur, Femtosecond pulsed laser micromachining of glass substrates with application to microfluidic devices, Appl. Opt. 43 (2004) 4584–4589. https://doi.org/10.1364/AO.43.004584.

[56] C. Hnatovsky, R.S. Taylor, E. Simova, V.R. Bhardwaj, D.M. Rayner, P.B. Corkum, Polarization-selective etching in femtosecond laser-assisted microfluidic channel fabrication in fused silica, Opt. Lett. 30 (2005) 1867. https://doi.org/10.1364/ol.30.001867.

[57] S.W. Bedell, D.K. Sadana, K. Fogel, H. Chen, A. Domenicucci, Quick turnaround technique for highlighting defects in thin Si/SiGe bilayers, Electrochem. Solid-State Lett. 7 (2004) 105–107. https://doi.org/10.1149/1.1676116.

[58] B. Öktem, I. Pavlov, S. Ilday, H. Kalaycioğlu, A. Rybak, S. Yavaş, M. Erdoğan, F.Ö. Ilday, Nonlinear laser lithography for indefinitely large-area nanostructuring with femtosecond pulses, Nat. Photonics. 7 (2013) 897–901. https://doi.org/10.1038/nphoton.2013.272.

[59] A. Turnali, in-Chip Devices Fabricated With Nonlinear Laser Lithography Deep Inside Silicon, (2019).

[60] M.S. Tyagi, R. Van Overstraeten, Minority carrier recombination in heavily-doped silicon, Solid State Electron. 26 (1983) 577–597. https://doi.org/10.1016/0038-1101(83)90174-0.

[61] N.G. Nilsson, Band-to-band auger recombination in silicon and germanium, Phys. Scr. 8 (1973) 165–176. https://doi.org/10.1088/0031-8949/8/4/007.

[62] N.D. Arora, J.R. Hauser, D.J. Roulston, Electron and Hole Mobilities in Silicon as a Function of Concentration and Temperature, IEEE Trans. Electron Devices. 29 (1982) 292–295. https://doi.org/10.1109/T-ED.1982.20698.

[63] C. Chen, T. Zhang, P. Contu, J. Klamkin, A.K. Coskun, A. Joshi, Sharing and Placement of On-chip Laser Sources in Silicon-Photonic NoCs, (2014). https://doi.org/10.1109/NOCS.2014.7008766.

[64] R.F. Wood, J.C. Wang, G.E. Giles, Note : This is a draft of a paper being submitted for publication . Contents of this paper should not be quoted nor referred to without permission of the authors . MACROSCOPIC THEORY OF PULSED LASER ANNEALING Operated by UNION CARBIDE CORPORATION for the , (n.d.).

[65] H.R. Shanks, P.D. Maycock, P.H. Sidles, G.C. Danielson, Thermal conductivity of silicon from 300 to 1400°K, Phys. Rev. 130 (1963) 1743–1748. https://doi.org/10.1103/PhysRev.130.1743.

[66] H.M. Van Driel, Kinetics of high-density plasmas generated in Si by 1.06- and 0.53-pm picosecond laser pulses, 35 (1987) 8166–8176.

[67] F. Optical, Ultrafast Heating of Silicon on Sapphire by Femtosecond Optical Pnlses, 56 (1986).

[68] R.A. Soref, B.R. Bennett, Electrooptical Effects in Silicon, (1987) 123–129.

[69] P.J. Timans, Emissivity of silicon at elevated temperatures Emksivity of silicon at elevated temperatures, 6353 (2012). https://doi.org/10.1063/1.355159.

[70] R. Bekenstein, R. Schley, M. Mutzafi, C. Rotschild, M. Segev, Optical

simulations of gravitational effects in the Newton-Schrödinger system, Nat. Phys. 11 (2015) 872–878. https://doi.org/10.1038/nphys3451.

[71] A.D. Bristow, N. Rotenberg, H.M. Van Driel, Two-photon absorption and Kerr coefficients of silicon for 850-2200 nm, Appl. Phys. Lett. 90 (2007). https://doi.org/10.1063/1.2737359.

[72] M.R. Watts, J. Sun, C. DeRose, D.C. Trotter, R.W. Young, G.N. Nielson, Adiabatic thermo-optic Mach–Zehnder switch, Opt. Lett. 38 (2013) 733. https://doi.org/10.1364/ol.38.000733.

[73] E.G. Turitsyna, S. Webb, Simple design of FBG-based VSB filters for ultra-dense WDM transmission ELECTRONICS LETTERS 20th January 2005, Electron. Lett. 41 (2005) 40–41. https://doi.org/10.1049/el.

[74] A. Brodeur, C.Y. Chien, F.A. Ilkov, S.L. Chin, O.G. Kosareva, V.P. Kandidov, Moving focus in the propagation of ultrashort laser pulses in air, Opt. Lett. 22 (1997) 304. https://doi.org/10.1364/ol.22.000304.

[75] G.P. Agrawal, Nonlinear fiber optics : its history and recent progress [Invited], 28 (2011) 0–1.

[76] A. Couairon, A. Mysyrowicz, Femtosecond filamentation in transparent media, Phys. Rep. 441 (2007) 47–189. https://doi.org/10.1016/j.physrep.2006.12.005.

[77] J. Leuthold, C. Koos, W. Freude, Nonlinear silicon photonics, Nat. Publ. Gr. 4 (2010) 535–544. https://doi.org/10.1038/nphoton.2010.185.

[78] J.T. Verdeyen, J. Thomas, I.J.T. Verdeyen, Laser Electronics THIRD EDITION, 1995.

[79] B.E.A. Saleh, M.C. Teich, <Fundamentals of Photonics-ICOLE2013.pdf>, n.d.

[80] F. Es, O. Demircioglu, M. Gunoven, M. Kulakci, H.E. Unalan, R. Turan, Performance of nanowire decorated mono- and multi-crystalline Si solar cells, Phys. E Low-Dimensional Syst. Nanostructures. 51 (2013) 71–74. https://doi.org/10.1016/j.physe.2013.01.002.

[81] H.J. Choi, S. Baek, H.S. Jang, S.B. Kim, B.Y. Oh, J.H. Kim, Optimization of metal-assisted chemical etching process in fabrication of p-type silicon wire arrays, Curr. Appl. Phys. 11 (2011) S25–S29. https://doi.org/10.1016/j.cap.2010.11.047.

[82] Z.P. Huang, N. Geyer, L.F. Liu, M.Y. Li, P. Zhong, Metal-assisted electrochemical etching of silicon, Nanotechnology. 21 (2010). https://doi.org/10.1088/0957-4484/21/46/465301.

[83] X. Li, P.W. Bohn, Metal-assisted chemical etching in HF / H2O2 produces porous silicon, 2572 (2012) 1–4. https://doi.org/10.1063/1.1319191.

[84] C. Lee, K. Tsujino, Y. Kanda, S. Ikeda, M. Matsumura, Pore formation in silicon by wet etching using micrometre-sized metal particles as catalysts, (2008) 1015–1020. https://doi.org/10.1039/b715639a.

[85] P.K. Mohseni, L. Pan, X. Zhao, S.H. Kim, K. Balasundaram, J.D. Kim, J.J. Coleman, X. Li, III-As pillar arrays by metal-assisted chemical etching for photonic applications, 2013 Conf. Lasers Electro-Optics, CLEO 2013. 1 (2013). https://doi.org/10.1364/cleo_si.2013.cth1j.3.

[86] A. Huczko, Invited paper Template-based synthesis of nanomaterials, 376 (2000) 365–376.

[87] A. Boltasseva, V.M. Shalaev, Fabrication of optical negative-index metamaterials : Recent advances and outlook, 2 (2008) 1–17. https://doi.org/10.1016/j.metmat.2008.03.004.

[88] D. Mills, M. Nahidi, K.W. Kolasinski, Stain etching of silicon pillars and macropores, Phys. Status Solidi Appl. Mater. Sci. 202 (2005) 1422–1426. https://doi.org/10.1002/pssa.200461119.

[89] J.P. Gambino, S.A. Adderly, J.U. Knickerbocker, Microelectronic Engineering An overview of through-silicon-via technology and manufacturing, Microelectron. Eng. (2015). https://doi.org/10.1016/j.mee.2014.10.019.

[90] B.M. Motoyoshi, Through-Silicon Via (TSV), 97 (2009) 43–48.

[91] B. Dang, M.S. Bakir, D.C. Sekar, C.R. King, J.D. Meindl, L. Fellow, Integrated Microfluidic Cooling and Interconnects for 2D and 3D Chips, 33 (2018) 79–87.

[92] K. Liu, S. Qu, X. Zhang, Z. Wang, Anisotropic characteristics and morphological control of silicon nanowires fabricated by metal-assisted chemical etching, J. Mater. Sci. 48 (2013) 1755–1762. https://doi.org/10.1007/s10853-012-6936-7.

[93] X. Li, Metal assisted chemical etching for high aspect ratio nanostructures: A review of characteristics and applications in photovoltaics, Curr. Opin. Solid State Mater. Sci. 16 (2012) 71–81. https://doi.org/10.1016/j.cossms.2011.11.002.

[94] C. Chartier, S. Bastide, C. Lévy-Clément, Metal-assisted chemical etching of silicon in HF-H2O2, Electrochim. Acta. 53 (2008) 5509–5516. https://doi.org/10.1016/j.electacta.2008.03.009.

[95] U.P. Formation, Uniform Pyramid Formation on A lkaline-et ched Polished Monocrystalline (1 00) Silicon Wafers, 4 (1996) 435–438.

[96] K. Kim, S.K. Dhungel, S. Jung, D. Mangalaraj, J. Yi, Texturing of large area multi-crystalline silicon wafers through different chemical approaches for solar cell fabrication, Sol. Energy Mater. Sol. Cells. 92 (2008) 960–968.

https://doi.org/10.1016/j.solmat.2008.02.036.

[97] Infrared absorption by sulfur-doped silicon formed by femtosecond laser irradiation, 1641 (2004) 1635–1641. https://doi.org/10.1007/s00339-004-2676-0.

[98] J. Shiu, C. Kuo, P. Chen, Fabrication of Tunable Superhydrophobic, 16 (2004).

[99] C. Wu, C.H. Crouch, L. Zhao, J.E. Carey, R. Younkin, J.A. Levinson, E. Mazur, R.M. Farrell, P. Gothoskar, A. Karger, C. Wu, Near-unity below-band-gap absorption by microstructured silicon Near-unity below-band-gap absorption by microstructured silicon, 1850 (2013) 23–26. https://doi.org/10.1063/1.1358846.

[100] L.L. Ma, Y.C. Zhou, N. Jiang, X. Lu, J. Shao, L.L. Ma, Y.C. Zhou, N. Jiang, Wide-band " black silicon " based on porous silicon, 171907 (2006). https://doi.org/10.1063/1.2199593.

[101] H. Savin, P. Repo, G. Von Gastrow, P. Ortega, E. Calle, M. Garín, R. Alcubilla, Black silicon solar cells with interdigitated back-contacts achieve 22.1% efficiency, (2015) 1–6. https://doi.org/10.1038/nnano.2015.89.

[102] R.M. Wagterveld, C.W.J. Berendsen, S. Bouaidat, J. Jonsmann, V. Scandina, M. Biode, V. Aps, V. Gammelgårds, D.- Farum, Ultralow Hysteresis Superhydrophobic Surfaces by Excimer Laser Modification of SU-8, (2006) 10904–10908.

[103] S. Zhong, Z. Huang, X. Lin, Y. Zeng, Y. Ma, High-Efficiency Nanostructured Silicon Solar Cells on a Large Scale Realized Through the Suppression of Recombination Channels, (2014) 1–7. https://doi.org/10.1002/adma.201401553.

[104] S. Koynov, M.S. Brandt, M. Stutzmann, Black nonreflecting silicon surfaces for solar cells, Appl. Phys. Lett. 88 (2006) 88–91. https://doi.org/10.1063/1.2204573.

[105] K. Peng, H. Fang, J. Hu, Y. Wu, J. Zhu, Y. Yan, S.T. Lee, Metal-particle-induced, highly localized site-specific etching of Si and formation of single-crystalline Si nanowires in aqueous fluoride solution, Chem. - A Eur. J. 12 (2006) 7942–7947. https://doi.org/10.1002/chem.200600032.

[106] M.C. Putnam, D.B. Turner-Evans, M.D. Kelzenberg, S.W. Boettcher, N.S. Lewis, H.A. Atwater, 10 μm minority-carrier diffusion lengths in Si wires synthesized by Cu-catalyzed vapor-liquid-solid growth, Appl. Phys. Lett. 95 (2009). https://doi.org/10.1063/1.3247969.

[107] K.V.N. and J.P. Izabela Kuzma-Filipek*, Frederic Dross, Kris Baert, Jose Luis Hernandez, Sukhvinder Singh, >16% thin-film epitaxial silicon solar cells on 70-cm2 area with 30-μm active layer, porous silicon back reflector, and Cu-based top-contact metallization, Ieee Trans Fuzzy Syst. 20 (2012)

1114–1129. https://doi.org/10.1002/pip.

[108] J.O. and H.M.B. Fatima Toor*, Efficient nanostructured ‘black’ silicon solar cell by copper-catalyzed metal-assisted etching, Ieee Trans Fuzzy Syst. 20 (2012) 1114–1129. https://doi.org/10.1002/pip.

[109] Y. Wang, L. Yang, Y. Liu, Z. Mei, W. Chen, J. Li, Maskless inverted pyramid texturization of silicon, Nat. Publ. Gr. (2015) 1–6. https://doi.org/10.1038/srep10843.

[110] M.K. Basher, R. Mishan, S. Biswas, M. Khalid Hossain, M.A.R. Akand, M.A. Matin, Study and analysis the Cu nanoparticle assisted texturization forming low reflective silicon surface for solar cell application, AIP Adv. 9 (2019). https://doi.org/10.1063/1.5109003.

[111] Y. Cao, Y. Zhou, F. Liu, Y. Zhou, Y. Zhang, Y. Liu, Y. Guo, Progress and Mechanism of Cu Assisted Chemical Etching of Silicon in a Low Cu 2+ Concentration Region , ECS J. Solid State Sci. Technol. 4 (2015) P331–P336. https://doi.org/10.1149/2.0191508jss.

[112] J.P. Lee, S. Choi, S. Park, Extremely superhydrophobic surfaces with micro- and nanostructures fabricated by copper catalytic etching, Langmuir. 27 (2011) 809–814. https://doi.org/10.1021/la1045354.

[113] H. Zheng, M. Han, P. Zheng, L. Zheng, H. Qin, L. Deng, Porous silicon templates prepared by Cu-assisted chemical etching, Mater. Lett. 118 (2014) 146–149. https://doi.org/10.1016/j.matlet.2013.12.093.

[114] X. Tan, Z. Tao, M. Yu, H. Wu, H. Li, Anti-reflectance optimization of secondary nanostructured black silicon grown on micro-structured arrays, Micromachines. 9 (2018). https://doi.org/10.3390/mi9080385.

[115] S. Dottermusch, R. Schmager, E. Klampaftis, S. Paetel, O. Kiowski, K. Ding, B.S. Richards, U.W. Paetzold, Micro-cone textures for improved light in-coupling and retroreflection-inspired light trapping at the front surface of solar modules, Prog. Photovoltaics Res. Appl. 27 (2019) 593–602. https://doi.org/10.1002/pip.3133.

[116] B. Radfar, F. Es, R. Turan, Effects of different laser modified surface morphologies and post-texturing cleanings on c-Si solar cell performance, Renew. Energy. 145 (2020) 2707–2714. https://doi.org/10.1016/j.renene.2019.08.031.

[117] K.W. Kolasinski, D. Mills, M. Nahidi, Laser assisted and wet chemical etching of silicon nanostructures, J. Vac. Sci. Technol. A Vacuum, Surfaces, Film. 24 (2006) 1474–1479. https://doi.org/10.1116/1.2188414.

[118] C.Q. Lai, H. Cheng, W.K. Choi, C. V. Thompson, Mechanics of catalyst motion during metal assisted chemical etching of silicon, J. Phys. Chem. C. 117 (2013) 20802–20809. https://doi.org/10.1021/jp407561k.

[119] Z. Huang, N. Geyer, P. Werner, J. De Boor, U. Gösele, Metal-assisted chemical etching of silicon: A review, Adv. Mater. 23 (2011) 285–308. https://doi.org/10.1002/adma.201001784.

[120] Y.T. Lu, A.R. Barron, Anti-reflection layers fabricated by a one-step copper-assisted chemical etching with inverted pyramidal structures intermediate between texturing and nanopore-type black silicon, J. Mater. Chem. A. 2 (2014) 12043–12052. https://doi.org/10.1039/c4ta02006e.

[121] Y. Wang, Y. Liu, L. Yang, W. Chen, X. Du, A. Kuznetsov, Micro-structured inverted pyramid texturization of Si inspired by self-assembled Cu nanoparticles, Nanoscale. 9 (2017) 907–914. https://doi.org/10.1039/c6nr08126f.

[122] W. Kern, Evolution of silicon wafer cleaning technology, Proc. - Electrochem. Soc. 90 (1990) 3–19. https://doi.org/10.1149/1.2086825.

[123] E. Granados, M. Martinez-Calderon, M. Gomez, A. Rodriguez, S.M. Olaizola, Photonic structures in diamond based on femtosecond UV laser induced periodic surface structuring (LIPSS), Opt. Express. 25 (2017) 15330. https://doi.org/10.1364/oe.25.015330.

[124] J. Bonse, S. V. Kirner, S. Höhm, N. Epperlein, D. Spaltmann, A. Rosenfeld, J. Krüger, Applications of laser-induced periodic surface structures (LIPSS), Laser-Based Micro- Nanoprocessing XI. 10092 (2017) 100920N. https://doi.org/10.1117/12.2250919.

[125] S. Kontermann, T. Gimpel, A.L. Baumann, K.M. Guenther, W. Schade, Laser processed black silicon for photovoltaic applications, Energy Procedia. 27 (2012) 390–395. https://doi.org/10.1016/j.egypro.2012.07.082.

[126] M. Otto, M. Algasinger, H. Branz, B. Gesemann, T. Gimpel, K. Füchsel, T. Käsebier, S. Kontermann, S. Koynov, X. Li, V. Naumann, J. Oh, A.N. Sprafke, J. Ziegler, M. Zilk, R.B. Wehrspohn, Black silicon photovoltaics, Adv. Opt. Mater. 3 (2015) 147–164. https://doi.org/10.1002/adom.201400395.

[127] V.Y. Fedorov, M. Chanal, D. Grojo, S. Tzortzakis, Accessing Extreme Spatiotemporal Localization of High-Power Laser Radiation through Transformation Optics and Scalar Wave Equations, Phys. Rev. Lett. 117 (2016) 1–5. https://doi.org/10.1103/PhysRevLett.117.043902.

[128] M. Chambonneau, Q. Li, M. Chanal, N. Sanner, D. Grojo, Writing waveguides inside monolithic crystalline silicon with nanosecond laser pulses, Opt. Lett. 41 (2016) 4875. https://doi.org/10.1364/OL.41.004875.

[129] M. Chanal, V.Y. Fedorov, M. Chambonneau, R. Clady, S. Tzortzakis, D. Grojo, Crossing the threshold of ultrafast laser writing in bulk silicon, Nat. Commun. 8 (2017) 1–6. https://doi.org/10.1038/s41467-017-00907-8.

[130] G.C. Giakos, A. Molhokar, A. Orozco, V. Kumar, S. Sumrain, D. Mehta, A.

Maniyedath, N. Ojha, A. Medithe, Laser imaging through scattering media, Conf. Rec. - IEEE Instrum. Meas. Technol. Conf. 1 (2004) 433–437. https://doi.org/10.1109/IMTC.2004.1351081.

[131] I. Pavlov, E. Dülgergil, E. Ilbey, F.Ö. Ilday, 10 W, 10 ns, 50 kHz all-fiber laser at 1.55 µm, in: Conf. Lasers Electro-Optics 2012, OSA, Washington, D.C., 2012: p. CTu2M.5. https://doi.org/10.1364/CLEO_SI.2012.CTu2M.5.

[132] W.C. Dash, Copper precipitation on dislocations in silicon, J. Appl. Phys. 27 (1956) 1193–1195. https://doi.org/10.1063/1.1722229.

[133] V.E. Sirtl, A. Adler, n, Zeitschrift Für Met. 52 (1961) 529.

[134] H. Seiter, INTEGRATIONAL ETCHING METHODS, in: Semicond. Silicon/1977, Electrochemical Society Proceedings, 1977: p. 187. https://books.google.com.tr/books?id=A8RQAAAAYAAJ&pg=187.

[135] M.W. Jenkins, A New Preferential Etch for Defects in Silicon Crystals, J. Electrochem. Soc. 124 (1977) 757. https://doi.org/10.1149/1.2133401.

[136] H. Younan, Studies of a new chemical etching method - 152 Secco Etch in failure analysis of wafer fabrication, IEEE Int. Conf. Semicond. Electron. Proceedings, ICSE. (1998) 20–26. https://doi.org/10.1109/smelec.1998.781143.

[137] A. Abbadie, S.W. Bedell, J.M. Hartmann, D.K. Sadana, F. Brunier, C. Figuet, I. Cayrefourcq, Study of HCl and Secco Defect Etching for Characterization of Thick sSOI, J. Electrochem. Soc. 154 (2007) H713. https://doi.org/10.1149/1.2740032.

[138] T.C. Chandler, MEMC Etch—A Chromium Trioxide-Free Etchant for Delineating Dislocations and Slip in Silicon, J. Electrochem. Soc. 137 (1990) 944–948. https://doi.org/10.1149/1.2086584.

[139] National Institute for Occupational Safety and Health (NIOSH), NIOSH chemical carcinogen policy, Curr. Intell. Bull. 68, DHHS Publ. Number 2017-100. (2017) 1–28. https://www.cdc.gov/niosh/docs/2017-100/pdf/2017-100.pdf?id=10.26616/NIOSHPUB2017100revised.

[140] K. Peng, J. Hu, Y. Yan, Y. Wu, H. Fang, Y. Xu, S. Lee, J. Zhu, Fabrication of single-crystalline silicon nanowires by scratching a silicon surface with catalytic metal particles, Adv. Funct. Mater. 16 (2006) 387–394. https://doi.org/10.1002/adfm.200500392.

[141] D. Nečas, P. Klapetek, Gwyddion: An open-source software for SPM data analysis, Cent. Eur. J. Phys. 10 (2012) 181–188. https://doi.org/10.2478/s11534-011-0096-2.

[142] Natick, MATLAB, (2021).

[143] W. Hadibrata, F. Es, S. Yerci, R. Turan, Ultrathin Si solar cell with nanostructured light trapping by metal assisted etching, Sol. Energy Mater.

Sol. Cells. 180 (2018) 247–252. https://doi.org/10.1016/j.solmat.2017.06.029.

[144] F. Dross, J. Robbelein, B. Vandevelde, E. Van Kerschaver, I. Gordon, G. Beaucarne, J. Poortmans, Stress-induced large-area lift-off of crystalline Si films, Appl. Phys. A Mater. Sci. Process. 89 (2007) 149–152. https://doi.org/10.1007/s00339-007-4195-2.

[145] S.W. Bedell, D. Shahrjerdi, B. Hekmatshoar, K. Fogel, P.A. Lauro, J.A. Ott, N. Sosa, D. Sadana, Kerf-less removal of Si, Ge, and III-V layers by controlled spalling to enable low-cost PV technologies, IEEE J. Photovoltaics. 2 (2012) 141–147. https://doi.org/10.1109/JPHOTOV.2012.2184267.

[146] S.W. Bedell, K. Fogel, P. Lauro, D. Shahrjerdi, J.A. Ott, D. Sadana, Layer transfer by controlled spalling, J. Phys. D. Appl. Phys. 46 (2013). https://doi.org/10.1088/0022-3727/46/15/152002.

[147] S. Kajari-Schröder, J. Käsewieter, J. Hensen, R. Brendel, Lift-off of free-standing layers in the kerfless porous silicon process, Energy Procedia. 38 (2013) 919–925. https://doi.org/10.1016/j.egypro.2013.07.365.

[148] R.A. Rao, L. Mathew, S. Saha, S. Smith, D. Sarkar, R. Garcia, R. Stout, A. Gurmu, E. Onyegam, D. Ahn, D. Xu, D. Jawarani, J. Fossum, S. Banerjee, A novel low cost 25µm thin exfoliated monocrystalline Si solar cell technology, Conf. Rec. IEEE Photovolt. Spec. Conf. (2011) 001504–001507. https://doi.org/10.1109/PVSC.2011.6186244.

[149] P.C. Verburg, G.R.B.E. Römer, A.J. Huis in ’t Veld, Two-photon–induced internal modification of silicon by erbium-doped fiber laser, Opt. Express. 22 (2014) 21958. https://doi.org/10.1364/oe.22.021958.

[150] E. Garnett, P. Yang, Light trapping in silicon nanowire solar cells, Nano Lett. 10 (2010) 1082–1087. https://doi.org/10.1021/nl100161z.

[151] M. Zolfaghari Borra, S. Kayra Güllü, F. Es, O. Demircioɨlu, M. Günöven, R. Turan, A. Bek, A feasibility study for controlling self-organized production of plasmonic enhancement interfaces for solar cells, in: Appl. Surf. Sci., 2014: pp. 43–50. https://doi.org/10.1016/j.apsusc.2013.12.088.

[152] D.Y. Jung, K.J. Moon, B.L. Park, G. Choi, H.K. Kang, C. Chung, Y. Rho, Properties of isolation liner and electrical characteristics of high aspect ratio TSV in 3D stacking technology, ASMC (Advanced Semicond. Manuf. Conf. Proc. (2012) 198–200. https://doi.org/10.1109/ASMC.2012.6212888.

APPENDICES

A. Dicing of CALP Samples

Related to Section 4.2. In the CALP samples, the laser processing modifies the Si below the surface. The total area of processed region was 10mm×10mm. In order to increase the number of samples for more investigations, the samples were diced to the size of 7.3mm×2.34mm which is shown in Fig 1.

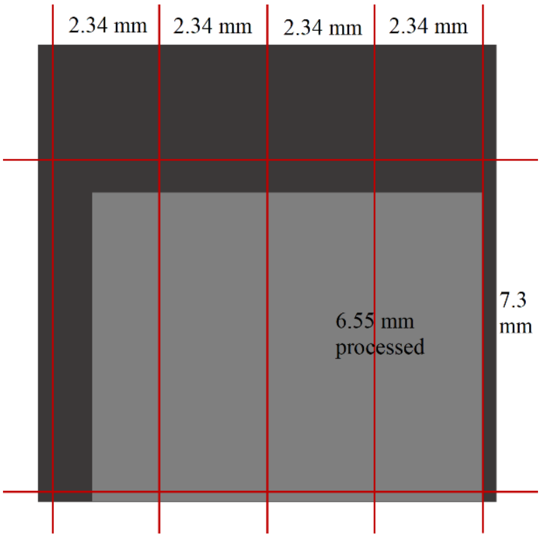

Fig 1 Schematic of diced laser processed samples with the size of 7.3mm×2.34mm.

B. Mass weights

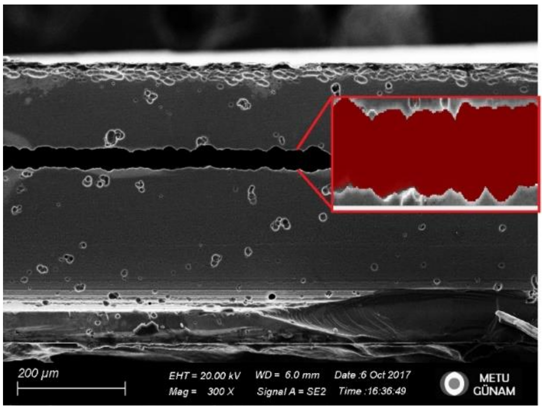

Fig 2 SEM image of the *Champion Etchant* indicating the surface smoothness and final opening after 60min etching treatment.

Table. 1 Measured masses of laser processed and unprocessed samples from *the Champion Etchant* over time including the calculated laser modified mass.

Time min	Laser Processed			Unprocessed				Laser Modified	
	Mass mg	M_t-M_{t-1} mg	M_t-M_{t0} mg	Mass mg	M_t-M_{t-1} mg	M_t-M_{t0} mg	$\frac{\% M_t - M_{t0}}{M_{t0}}$	Corrected Mass mg	$\frac{\% M_t}{M_{processed}}$
0	20.40			20.60					
10	20.05	0.35	0.35	20.40	0.20	0.20	0.97087	0.01795	1.70848
20	19.85	0.20	0.55	20.30	0.10	0.30	1.45631	0.05193	4.94216
30	19.60	0.25	0.80	20.20	0.10	0.40	1.94175	0.13590	12.93474
40	19.40	0.20	1.00	20.20	0.00	0.40	1.94175	0.33590	31.97028
50	19.25	0.15	1.15	20.15	0.05	0.45	2.18447	0.40289	38.34601
60	19.10	0.15	1.30	20.10	0.05	0.50	2.42718	0.46988	44.72174

Table. 2 Measured masses and corresponding geometrical parameters of *the Champion Etchant* for both laser processed and unprocessed samples.

		Laser Processed	Unprocessed
Initial Mass	mg	20.4	20.6
Final Mass	mg	19.1	20.1
Corresponding Initial Volume	mm^3	8.75912	8.84500
Corresponding Final Volume	mm^3	8.20095	8.63031
Corresponding Initial Thickness	µm	512.76924	517.79639
Corresponding Final Thickness	µm	502.99950	508.02665
Δ Thickness	µm	9.76974	9.76974
Total Area	µm	44.14711	44.08096

Table. 3 Calculated correction factors and intermediate parameters of *the Champion Etchant*.

		Laser Modified		
Corresponding Total Mass from Laser Modification	mg	1.07090		
Corresponding Total Volume from Laser Modification	mm^3	0.45981	CFIM	1.00980
Corresponding Total Opening Area from Laser Modification	mm^2	0.4632	CFEO	0.66996
Real Opening Area from SEM at 500x	mm^2	0.02178	CFAA	95.609
Corresponding Opening Thickness from SEM	µm	36.54530		
Corresponding Opening Thickness of Unprocessed Region from Inside from SEM	µm	6.54530		

C. Infrared images of laser modified region

IR Camera Images of various sets that shows the laser modified and etched regions.

Set 1

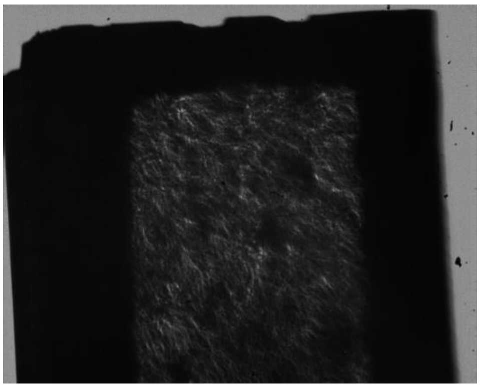

Set 2

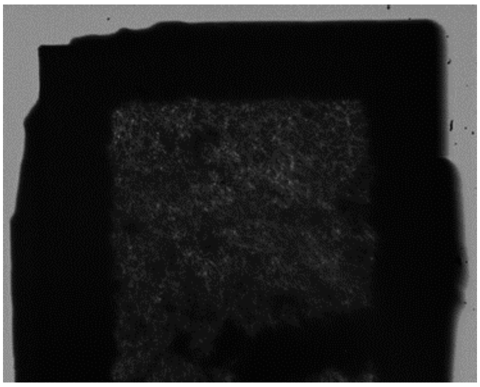

Set 3

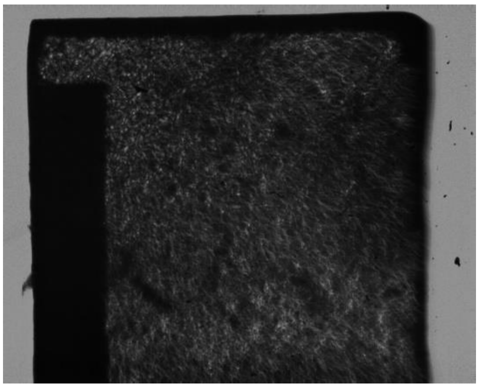

Set 4

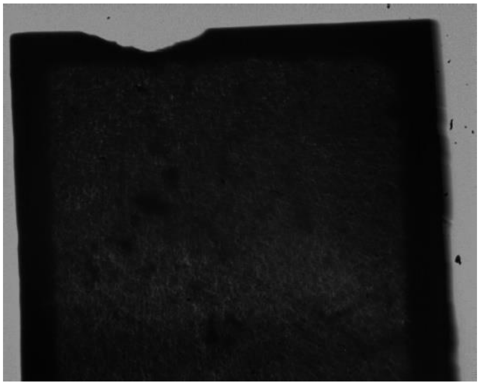

Set 5

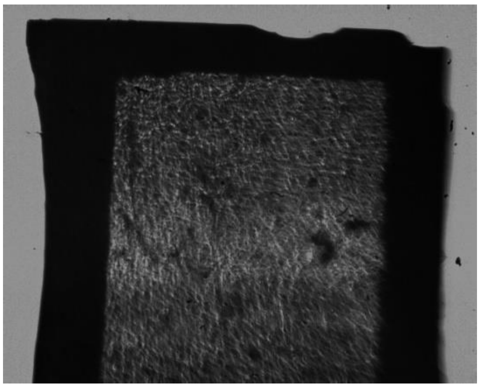

Set 6

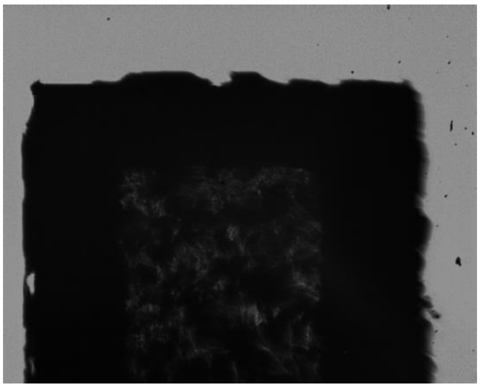

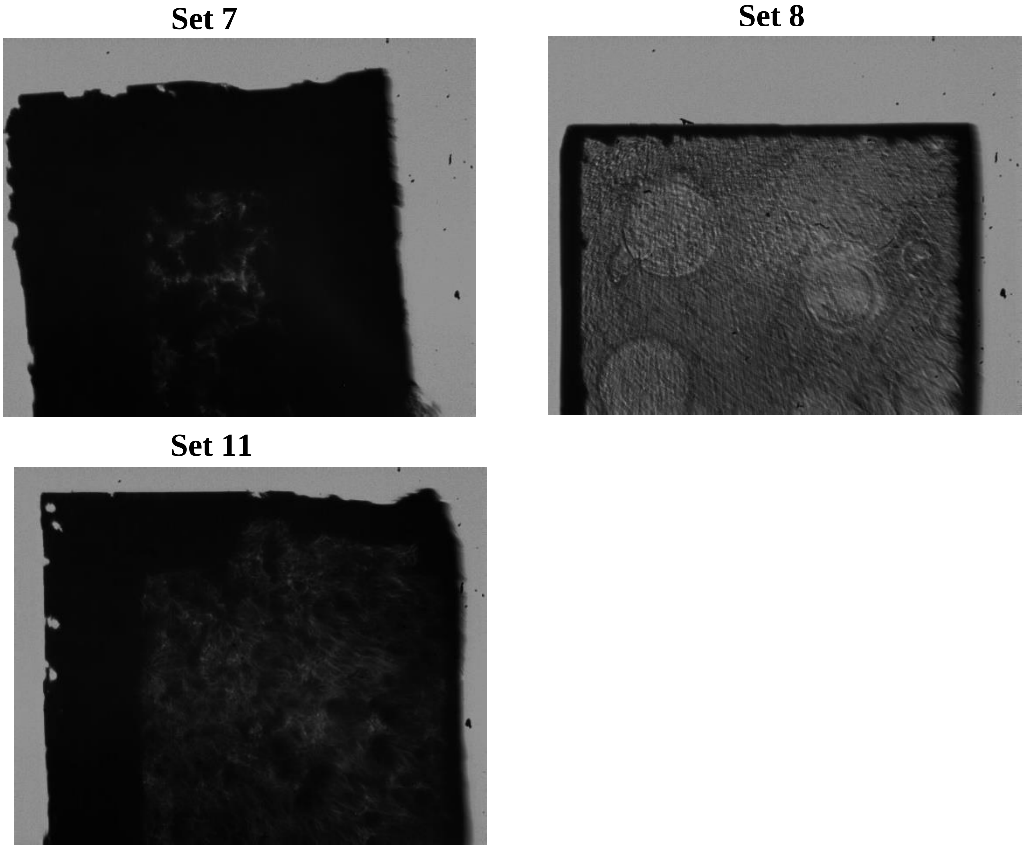

Fig 3 Images of the infrared camera of the etched laser modified region for various sets.

D. Derivative of laser modified of etched mass

The derivative of laser modified mass changes are presented in Fig 4, Fig 5, and Fig 6 for the variations in $Cu(NO_3)_2$, HF, and HNO_3 respectively. These figures are derivative of normalized etched mass shown in the Figure 3.14 (d), Figure 3.15 (d) and Figure 3.16 (d).

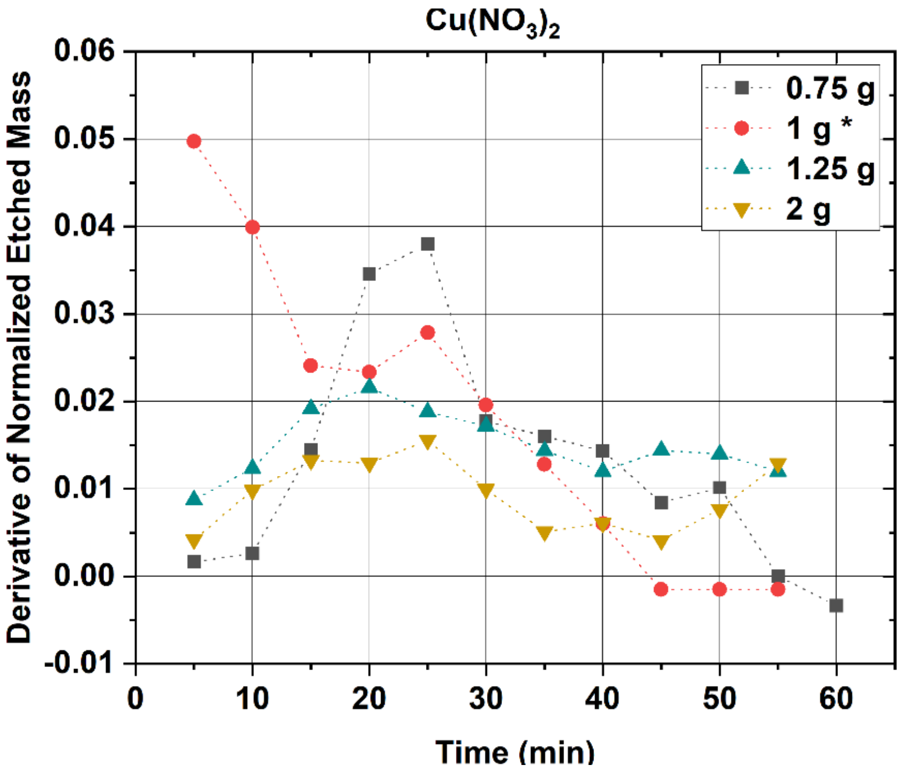

Fig 4 Derivative of Laser modified mass change of $Cu(NO_3)_2$ variations

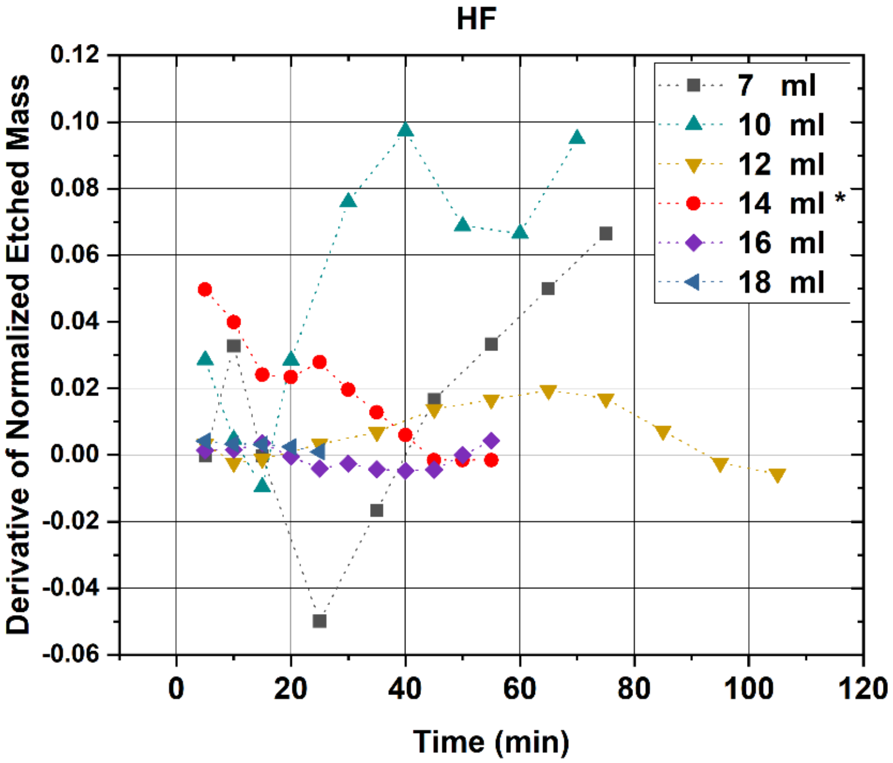

Fig 5 Derivative of Laser modified mass change of HF variations

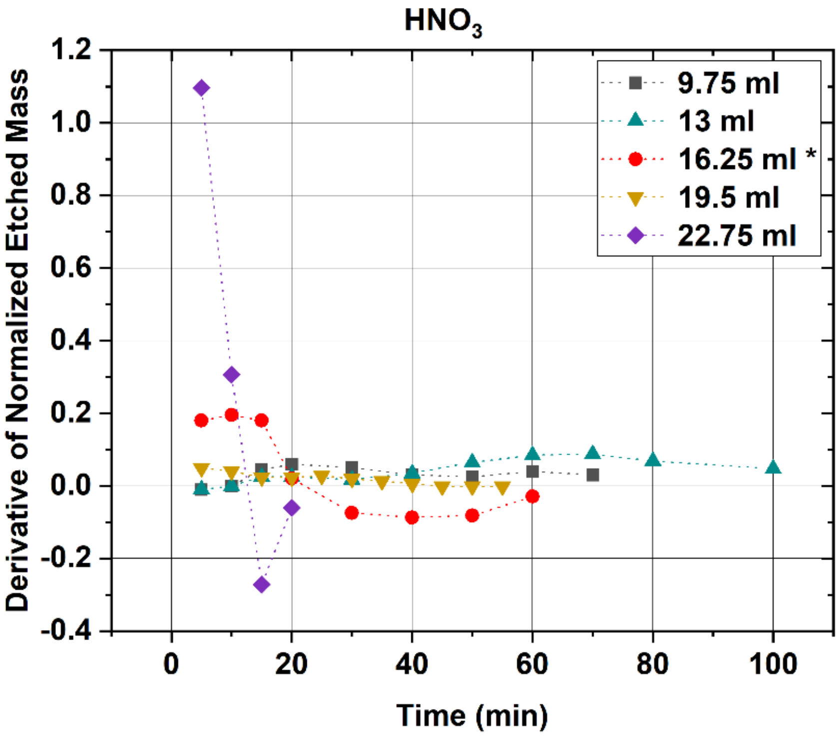

Fig 6 Derivative of Laser modified mass change of HNO_3 variations

CURRICULUM VITAE

PERSONAL INFORMATION

Surname, Name: Zolfaghari Borra, Mona
Nationality: Iranian (IR)
Date and Place of Birth: 23 August 1986, Oroumieh
Marital Status: Single
Phone: +90 312 210 90 95
email: mona.zolfaghariborra@metu.edu.tr

EDUCATION

Degree	**Institution**	**Year of Graduation**
MS	METU Micro and Nanotechnology	2013
BS	Islamic Azad University Tabriz Electrical and Electronics Engineering	2009

WORK EXPERIENCE

Year	**Place**	**Enrollment**
2021-Present	METU GÜNAM	Senior Researcher
2018-2021	METU GÜNAM	Lead Researcher
2013-2018	METU GÜNAM	Researcher

FOREIGN LANGUAGES

Advanced English, Persian

PUBLICATIONS

1. O. Tokel, A. Turnall, G. Makey, P. Elahi, T. Çolakoğlu, E. Ergeçen, Ö. Yavuz, R. Hübner, **Mona Zolfaghari Borra**, I. Pavlov, A. Bek, R. Turan, D.K. Kesim, S. Tozburun, S. Ilday, F.Ö. Ilday, "In-chip microstructures and photonic devices fabricated by nonlinear laser lithography deep inside silicon", (Nat. Photonics. 11 (2017) 639–645 submitted).

2. **Mona Zolfaghari Borra**, Behrad Radfar, Hisham Nasser, Tahir Çolakoğlu, Ahmet Turnalı, Onur Tokel, Hande Toffoli, F. Ömer İlday, Raşit Turan, Ihor Pavlov, Alpan Bek, "Development and Application of a Selective Wet-Chemical Etchant for Surface and Subsurface Laser Modified Silicon", (Manuscript under submission).

3. Hisham Nasser, Fırat Es, **Mona Zolfaghari Borra**, Emel Semiz, Gamze Kökbudak, Efe Orhan, Raşit Turan, "On the application of hole-selective MoO_x as full-area rear contact for industrial scale p-type c-Si solar cells", (Progress in Photovoltaics Research and Applications submitted), November 2020, 1-13.

4. Ozan Akdemir, **Mona Zolfaghari Borra,** Hisham Nasser, Raşit Turan, Alpan Bek, "MoO_x/Ag/MoO_x multilayers as hole transport transparent conductive electrodes for n-type crystalline silicon solar cells", (International Journal of Energy Research submitted), December 2019, 3098-3109.